Assay Development for the Point of Care Detection of Small Molecules for Diagnostic: Two Biomarkers, L-Kynurenine and Ethanolamine, as Examples

Dissertation
der Mathematisch-Naturwissenschaftlichen Fakultät
der Eberhard Karls Universität Tübingen
zur Erlangung des Grades eines
Doktors der Naturwissenschaften
(Dr. rer. nat.)

vorgelegt von
Isabel Quint
aus Donaueschingen

Tübingen
2025

Gedruckt mit Genehmigung der Mathematisch-Naturwissenschaftlichen Fakultät der Eberhard Karls Universität Tübingen.

Tag der mündlichen Qualifikation:	17.10.2025
Dekan:	Prof. Dr. Thilo Stehle
1. Berichterstatter/-in:	Prof. Dr. Stefan Laufer
2. Berichterstatter/-in:	Prof. Dr. Hans-Peter Deigner
3. Berichterstatter/-in:	Prof. Dr. Karine Mougin

List of Abbreviations

3D	three-dimensional
APTES	3-Aminopropyltriethoxysilane
CBD	controlled dielectric breakdown
CKD	chronic kidney disease
Da	Dalton
EA	ethanolamine
ELISA	enzyme-linked immunosorbent assay
FIB-SEM	Focused Ion Beam Scanning Electron Microscope
GC/MS	gas chromatography-mass spectrometry
HPLC	high-performance liquid chromatography
IDO	indoleamine-2,3-dioxygenase
I-V	current-voltage
Kd	dissociation constant
KP	Kynurenine pathway
LC-MS	liquid chromatography-mass spectrometry
MspA	Mycobacterium smegmatis porin A
NNI	Northern Nanopore Instruments
ONT	Oxford Nanopore Technologies
PCR	polymerase chain reaction
PE	Phosphatidylethanolamine
POC	Point of Care
SELEX	Systematic Evolution of Ligands by Exponential Enrichment
SiN	silicon nitride

ss	single-stranded
ssNA	single-stranded nucleic acid
ssNP	solid-state nanopore
nt	nucleotide
TLC	Thin-layer chromatography
FC	Flash column chromatography
KDE	kernel density estimation

Acknowledgements

The experiments described in this thesis were performed during 2021 and 2025 in the group of Prof. Dr. Hans-Peter Deigner at the Institute of Precision Medcine, Furtwangen University.

First and foremost, I would like to express my sincere gratitude to everyone who supported me throughout my PhD and continuously motivated me to persevere.

I would like to thank my supervisor, Prof Dr Hans-Peter Deigner, for giving me the great opportunity to do my doctorate at HFU under his guidance. I am also very grateful for his financial support and for his supervision, encouragement and guidance throughout my doctoral studies.

I would also like to express my appreciation and gratitude to Prof. Dr. Stefan Laufer for allowing me to write my doctoral thesis under his supervision at the University of Tübingen and for his support during this process.

I am especially thankful to all my colleagues from the working group, including Helga Weinschrott, Oliver Riester, Andreas Krames, Levin Riedel, Lars Kaiser, Christoph Ruppert, Max Borgolte, and Simone Rentschler, who warmly welcomed me and helped create a pleasant and friendly working environment. A special thanks to Lars Kaiser, who supervised my Master's thesis and was always available for technical questions and constructive discussions.

I am also extremely grateful for the emotional support of my colleagues Simone Rentschler, Michaela Knöpfle, and Weronika Schary, who not only encouraged me time and again but also became close friends during my time at the university.

Finally, I would like to thank my friends and family outside the university for their unwavering support and belief in me.

Contents

Zusammenfassung

Diagnostische Tests zur Detektion kleiner Moleküle spielen eine Schlüsselrolle in der modernen Medizin, da sie eine präzise Identifikation von Biomarkern, Metaboliten, Arzneimitteln und Umwelttoxinen in biologischen Proben wie Blut, Urin oder Gewebe ermöglichen. Traditionell kommen Techniken wie Massenspektrometrie und Chromatographie zum Einsatz, die durch ihre hohe Sensitivität und Spezifität tiefgehende Einblicke in Krankheitsprozesse, Pharmakokinetik und die Reaktion von Patienten auf therapeutische Interventionen bieten. Diese Methoden sind jedoch oft komplex, teuer und erfordern spezialisierte Geräte und Fachkenntnisse.

Die vorliegende Dissertation konzentriert sich auf die Entwicklung massenspektrometrie-unabhängiger diagnostischer Assays zur Detektion kleiner Moleküle. Ziel war es, die bestehenden Limitationen traditioneller Methoden zu überwinden und das Potenzial markierungsfreier Detektionsverfahren in verschiedenen diagnostischen Anwendungen zu untersuchen. Diese neuen Verfahren könnten die Grundlage für klinische Tests bilden, die eine breitere Verfügbarkeit und Anwendung in der Routine-Diagnostik ermöglichen. Die Dissertation gliedert sich in drei Teile: Der **erste Teil** beschreibt die Entwicklung eines fluoreszenzbasierten, kompetitiven Antikörperbindungsassays für L-Kynurenin, einem potenziellen Biomarker für das Versagen von Nierentransplantaten. Ein fluorescein-markiertes Kynurenin-Derivat wurde synthetisiert und seine Bindung an spezifische Antikörper in einem Bead-Assay nachgewiesen, was einen vielversprechenden Ansatz für einen Kynurenin-Schnelltest im Speichel darstellt. Der **zweite Teil** befasst sich mit der Implementierung einer Nanoporenplattform zur markierungsfreien Quantifizierung kleiner Moleküle, am Beispiel von Ethanolamin. Ein Strangverdrängungstest mit einem Ethanolamin-bindenden Aptamer ermöglichte die indirekte Detektion mittels Protein-Nanoporen im mikromolaren Bereich. Beide Assays beruhen auf der Bindung des Zielmoleküls an magnetische Beads und verwenden innovative Detektionsmethoden, die bisher noch nicht beschrieben wurden. Der **dritte Teil** vergleicht die Stabilität, Sensitivität und Variabilität von Festkörper-Nanoporen mit denen von Protein-Nanoporen, wobei die Herausforderungen und Vorteile des Einsatzes von Festkörper-Nanoporen in der Detektion kleiner Moleküle untersucht werden.

Zusammenfassend trägt diese Dissertation zur Weiterentwicklung diagnostischer Tests bei, indem sie neue, markierungsfreie Detektionsmethoden für kleine Moleküle präsentiert, die großes Potenzial für zukünftige klinische Anwendungen bieten.

Abstract

Diagnostic assays for the detection of small molecules play a key role in modern medicine, as they enable the precise identification of biomarkers, metabolites, drugs, and environmental toxins in biological samples such as blood, urine, or tissue. Traditionally, techniques like mass spectrometry and chromatography are used, providing in-depth insights into disease processes, pharmacokinetics, and patients' responses to therapeutic interventions due to their high sensitivity and specificity. However, these methods are often complex, expensive, and require specialized equipment and expertise.

This dissertation focuses on the development of mass spectrometry-independent diagnostic assays for the detection of small molecules. The aim was to overcome the limitations of traditional methods and explore the potential of label-free detection techniques in various diagnostic applications. These new methods could form the basis for clinical tests that enable broader availability and application in routine diagnostics. The dissertation is divided into three parts: The **first part** describes the development of a fluorescence-based, competitive antibody binding assay for L-Kynurenine, a potential biomarker for kidney transplant failure. A fluorescein-labeled kynurenine derivative was synthesized and its binding to specific antibodies in a bead assay was demonstrated, offering a promising approach for a kynurenine point of care test in saliva. The **second part** focuses on implementing a nanopore platform for the label-free quantification of small molecules, using ethanolamine as a model combound. A strand displacement assay with an ethanolamine-binding aptamer enabled indirect detection via commercially available protein nanopores in the micromolar range. Both assays rely on the binding of the target molecule to magnetic beads and employ innovative detection methods that have not been described yet. The **third part** adresses the fabrication process of solid-state nanopores, comparing their stability, sensitivity, and variability with those of protein nanopores, investigating the challenges and advantages of using solid-state nanopores for the detection of small molecules.

In summary, this dissertation contributes to the advancement of diagnostic tests by presenting novel, label-free detection methods for small molecules, which hold great potential for future clinical applications.

List of Publications

Original Articles, included in this work:

- Borgolte M, Quint I, Kaiser L, Csuk R, Deigner HP. *A Fluorescence-Based Competitive Antibody Binding Assay for Kynurenine, a Potential Biomarker of Kidney Transplant Failure*. Diagnostics (Basel) **2022**, Jun 2;12(6):1380. doi: 10.3390/diagnostics12061380. PMID: 35741190; PMCID: PMC9221851.

- Quint, Isabel; Simantzik, Jonathan; Kaiser, Lars; Laufer, Stefan; Csuk, Rene'; Smith, David et al.: *Ready-to-use nanopore platform for label-free small molecule quantification: Ethanolamine as first example*. In: Nanomedicine: nanotechnology, biology, and medicine **2024**, 55, S. 102724. DOI: 10.1016/j.nano.2023.102724.

Further publications, including reviews, which are not or not directly included in this work:

- Borgolte, M.; Riester, O.; Quint, I.; Blendinger, F.; Bucher, V.; Laufer, S.; Csuk, R.; Scotti, L.; Deigner, H. P. *Synthesis of a Biocompatible Benzophenone-Substituted Chitosan Hy drogel as Novel Coating for PEEK with Extraordinary Strong Antibacterial and Anti-Biofilm Properties*. Materials Today Chemistry **2022**, 26, 101176. https://doi.org/10.1016/j.mtchem.2022.101176.

- Kaiser, Lars; Quint, Isabel; Csuk, René; Jung, Manfred; Deigner, Hans-Peter *Lineage-Selective Disturbance of Early Human Hematopoietic Progenitor Cell Differentiation by the Commonly Used Plasticizer Di-2-ethylhexyl Phthalate via Reactive Oxygen Species: Fatty Acid Oxidation Makes the Difference*. In: Cells **2021**, 10 (10). DOI: 10.3390/cells10102703.

- Kaiser, Lars; Weinschrott, Helga; Quint, Isabel; Blaess, Markus; Csuk, René; Jung, Manfred et al.: *Metabolite Patterns in Human Myeloid Hematopoiesis Result from Lineage-Dependent Active Metabolic Pathways*. In: International journal of molecular sciences **2020**, 21 (17). DOI: 10.3390/ijms21176092.

1 Introduction

Parts of this introduction are based on the author's previous publications [1, 2].

1.1 Small molecule detection

The detection of small molecules is critically important across various fields, including molecular diagnostics, drug development, disease monitoring, and environmental and food analysis. However, it remains a significant challenge due to several factors. Small molecules, typically defined as compounds with a molar mass below 1000 Dalton (Da), include a diverse range of substances such as peptides, drugs, biogenic amines, small-molecule hormones, antibiotics, organic pollutants, food additives, pesticide and veterinary drug residues, and mycotoxins (see Figure 1) [3].These molecules are integral to many biological and chemical processes, making their accurate detection crucial for ensuring health, safety, and regulatory compliance. One of the primary challenges in small molecule detection is their size. Their small size limits the presence of multiple epitopes, often restricting specific antibody binding, reducing the sensitivity and specificity of immunoassays [4]. Additionally, small molecules often share similar chemical structures, further complicating selective detection in complex matrices such as blood, urine, food, and environmental sample [5–9].

To address these issues, current state-of-the-art technologies rely on advanced spectroscopic and chromatographic techniques, including high-performance liquid chromatography (HPLC), liquid chromatography-mass spectrometry (LC/MS), and gas chromatography-mass spectrometry (GC/MS) [10–16]. These techniques offer high sensitivity, accuracy, and the ability to identify and quantify small molecules, even at low concentrations. However, despite their advantages, these techniques present several limitations [16], including:

1. **Complex sample preparation:** Techniques like HPLC, LC/MS, and GC/MS often require extensive sample cleanup, such as solid-phase extraction or immunoaffinity purification, which can be time-consuming and labor-intensive, requiring specialized equipment and trained personnel.

2. **Matrix effects:** Small molecules are often detected in complex biological or environmental matrices, which can interfere with the detection process. Matrix components such as proteins, lipids, or other contaminants can affect the accuracy and sensitivity of the assays, necessitating thorough pretreatment.

3. **Cost and scalability:** The instrumentation for spectroscopic and chromatographic methods is expensive, and routine analysis can be cost-prohibitive for large-scale screening. Additionally, the complexity of the methods limits their accessibility in resource-limited settings or for point-of-care (POC) testing.

4. **Time-consuming workflows:** Despite their precision, these techniques often involve lengthy processes, including multiple steps of sample extraction, purification, and analysis, that extend processing times. In time-sensitive applications, such as disease diagnostics or environmental monitoring, faster detection methods are needed.

Given these limitations, there is increasing interest in developing alternative detection approaches that are faster, more cost-effective, and capable of real-time analysis with high specificity and sensitivity [1, 2, 8, 17–19]. Emerging technologies include:

1. **Competitive immunoassays:** Competitive immunoassays are particularly useful for detecting small molecules, where the target molecule competes with a labeled version for binding to a specific antibody. This method overcomes the challenge of limited epitopes on small molecules, offering high sensitivity and specificity.

2. **Aptamers:** Due to their high specificity, stability, and flexibility, aptamers are emerging as a powerful technology for small molecule detection. These short, single-stranded (ss) DNA or RNA molecules fold into unique three-dimensional structures, allowing them to bind tightly and selectively to small molecules, much like antibodies. Unlike antibodies, aptamers can be chemically synthesized, making them more cost-effective and easier to modify for enhanced stability and detection performance.

3. **Nanotechnology-based approaches:** Nanomaterials, such as nanoparticles, nanotubes, and nanopores, enhance detection sensitivity methods by amplifying signals or increasing the surface area for molecular interactions. **Nanopores**, in particular, are gaining attention for their ability to detect individual molecules by monitoring changes in ionic current as molecules pass through the tiny pores. These nanopores offer real-time, label-free detection and are highly sensitive, making them ideal for applications requiring precise small molecule analysis.

In conclusion, while traditional methods for small molecule detection provide reliable and highly accurate results, their limitations underscore the need for continued innovation. New approaches, particularly those that integrate new immunoassay technologies and nanotechnology, have the potential to address current challenges and improve the efficiency and accessibility of small molecule detection across various applications in molecular science [20–22].

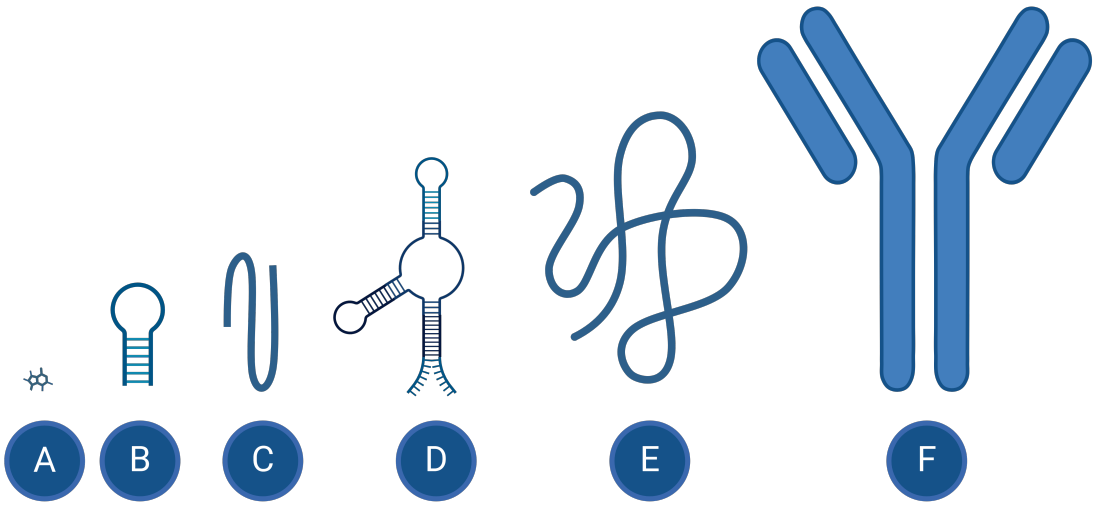

Figure 1: Comparison of different molecules according to size. Note that due to possible conformational differences, the actual size of aptamers may vary greatly. **(A)** caffeine, 0.2 kDa; **(B)** 50mer oligonucleotide, 16 kDa; **(C)** human insulin, 6 kDa; **(D)** 100mer oligonucleotide, 32 kDa; **(E)** human serum albumin, 66 kDa; **(F)** IgG1-antibody, 150 kDa. (Created in BioRender.com, accessed on February 2025.)

1.2 Competitive Immunoassays

Immunoassays are the most common approach for the detection of larger molecules, such as proteins, peptides, or other molecules with a specific antibody. Therefore, they are not typically considered an emerging technology for small molecule detection. Small molecule detection using immunoassays presents unique challenges due to the limited number of epitopes (binding sites) on small molecules, making it harder to generate strong immune responses and highly specific antibodies [4]. Despite this, they remain highly relevant and continue to evolve as attractive alternatives to spectroscopic and chromatographic techniques, with innovations improving their sensitivity, specificity, and ease of use. Consequently, immunoassay technologies are still extensively used in areas such as drug testing, food safety, environmental monitoring, and clinical diagnostics [8, 23, 24]. While they can be highly sensitive and specific, they often require further optimization to work effectively for small molecule detection.

As a result, many commercial enzyme-linked immunosorbent assay (ELISA) kits have been developed for detecting various analytes such as hormones, mycotoxins, antibiotics, and pesticide and veterinary drug residues [8, 25]. One significant advancement in immunoassay technology for small molecule detection is the use of competitive immunoassays. In this format, the principle is based on the competition between the target small molecule (analyte) in the sample and a labeled version of the same molecule for binding to a limited number of antibody binding sites. When the target small molecule is present in higher concentrations, less of the labeled molecule binds to the antibody, and this competition results in a measurable signal inversely proportional to the concentration of the analyte (see Figure 2) [26].

Advantages of a competitive immunoassay include higher sensitivity, since the signal is inversely proportional to the analyte concentration, these assays can achieve high sensitivity, even for trace amounts of small molecules. Furthermore, they are versatile in use and can be adapted for a wide range of applications, from food safety testing to medical diagnostics. On the other hand, they are cost effective, compared to spectroscopic and chromatographic methods, especially for high throughput applications. Nevertheless, there are still some challenges that need to be overcome [27]. Due to the limited epitope availability, generating highly specific antibodies is challenging [28]. Especially competitive immunoassays, can be affected by complex sample matrices (e.g., blood, urine, saliva or environmental samples), where interfering substances can cause false positive or negative results [9]. Additional steps such as sample purification or pre-treatment may be required, increasing the complexity of the assay. Moreover, careful optimization is often required, including adjustments of the antibody/analyte-ratio, buffer composition, and detection methods [29]. This optimization process can be labor-intensive and may require fine-tuning to achieve reliable results. Nevertheless, once optimized, these assays are easy to perform and can be conducted by less-trained personnel, representing an important step towards POC testing. This makes competitive immunoassays particularly useful for

label-free detection of small molecules, such as hormones, toxins, drugs, and other medical or environmental biomarkers [17, 30].

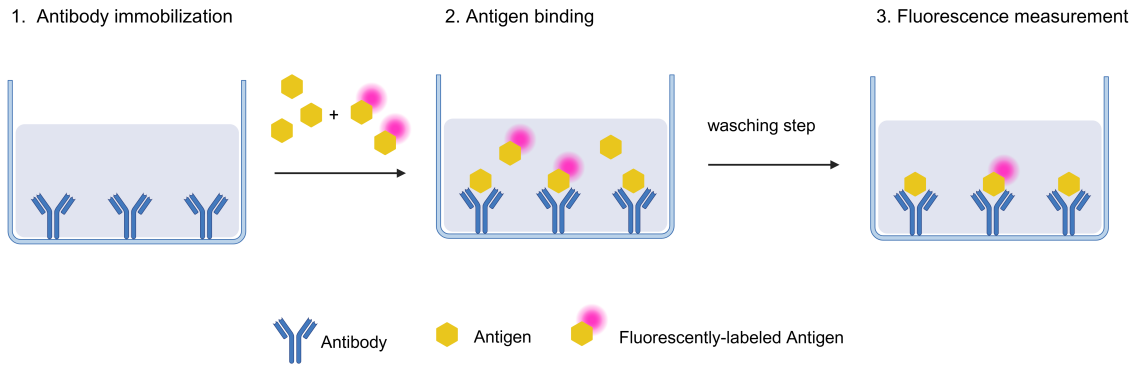

Figure 2: Schematic principle of a competitive immunoassay. First, the antibody is immobilized on a solid surface. Then, the target antigen sample is added along with a known amount of fluorescently labeled analogs. Both the target antigen and labeled analogs compete for the available antibody binding sites. As the concentration of the target antigen increases, the amount of bound fluorescently labeled antigen decreases, and vice versa. After washing away unbound antigen, the fluorescence intensity is measured with a photometer to quantify the target antigen. (Created in BioRender.com, accessed on October 2024.)

1.2.1 Antibodies

Antibodies, also known as immunoglobulins play a crucial role in immunoassays as highly specific molecules that bind to target antigens, enabling the detection and quantification of various analytes, including proteins, small molecules, hormones, and pathogens. This specificity makes them the ideal binding component for competitive immunoassays. Immunoassays rely on the unique ability of antibodies to recognize specific epitopes on target molecules, making them invaluable tools in diagnostics, drug development, and environmental monitoring. Originally, antibodies are specialized proteins produced by the immune system that have the ability to specifically recognize and bind to certain target molecules, called antigens. Their inherent specificity and affinity can be altered during the development of immunoassays to improve performance. In research two different types of antibodies are used: **1. Polyclonal:** These are a mixture of antibodies, recognizing multiple epitopes on the same antigen. **2. Monoclonal:** In contrast monoclonal antibodies, are identical and recognize only one specific epitope on the antigen. As small molecules typically present only one present epitope, monoclonal antibodies are preferred for small molecule detection [31]. Key challenges in developing antibodies for small molecules include cross-reactivity, since many small molecules have similar chemical

structures, antibodies might bind to molecules other than the target, leading to false positives or inaccurate measurements. Also, they require high affinity to ensure sensitive detection, as small molecules are often present in very low concentrations [32]. Despite these challenges, several antibodies against small molecules have been successfully developed for various biological applications [33–36].

1.3 Aptamers

Aptamers are emerging as alternatives to traditional antibodies for various applications, offering greater stability and flexibility, especially for small molecule detection [3, 37]. Aptamers are short, typically 20-60 nucleotides (nt) long, single-stranded DNA or RNA molecules that can fold into specific three-dimensional shapes, allowing them to bind tightly and selectively to target molecules, much like antibodies. The binding affinity of aptamers to target molecules relies on the structural diversity and spatial conformation of single-stranded nucleic acids (ssNA). In the presence of target molecules, aptamers undergo self-adaptive folding to form stable three-dimensional (3D) structures, such as hairpins, pseudoknots, stem-loops, or G-quadruplexes (see Figure 3). This folding is driven by complementary base-pairing, van der Waals forces, electrostatic interactions, and hydrogen bonding. As a result, larger contact area is built between the aptamer and its target, allowing high specific affinity binding [37, 38].

Unlike antibodies, aptamers show no immune response, allowing therapeutic use, and have a modifiable structure, making chemical modification with functional groups and conjugation to other molecules possible. Also, aptamers can target a broader range of molecules from ions and small organic molecules, such as toxins, drugs, and metabolites to large macromolecules, like proteins or other nucleic acids [39].

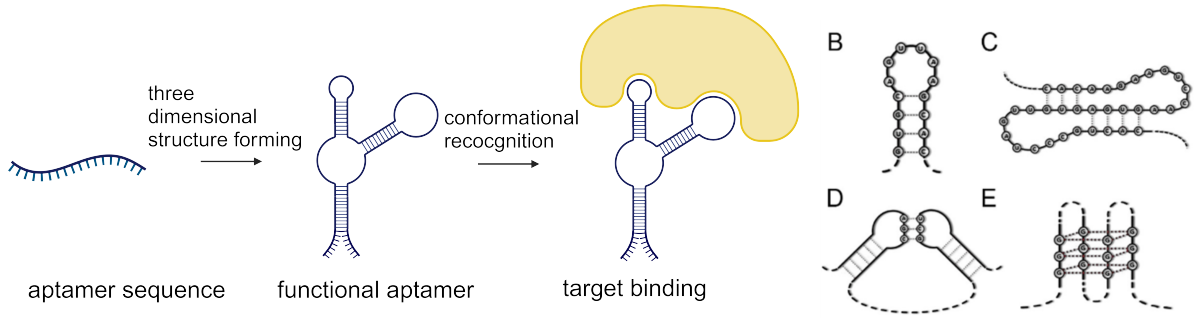

Figure 3: **(A)** Schematic representation of aptamer conformational recognition of targets to form an aptamer-target complex (illustrated as a stem-loop structure). **(B)** hairpin, **(C)** pseudo-knot, **(D)** joined hairpins, and **(E)** G-quadruplex structure. (Created in BioRender.com, accessed on February 2025) adapted from [37]. This article is an open access article distributed under the terms and conditions of the Creative Commons Attribution (CC BY) license (https://creativecommons.org/licenses/by/4.0/).

Aptamers are generated through a molecular evolution process known as SELEX (Systematic Evolution of Ligands by Exponential Enrichment), which can be performed in vitro [40, 41] or even in vivo [42]. In this process, a large random library of nucleic acid sequences is exposed to a desired target molecule e.g., peptides, metabolites, drugs, or other small molecules, which are often immobilized on a surface. Nucleic acids that bind weakly or nonspecifically to the target are washed away, while nucleic acids with stronger, more specific interaction remain bound. The bound nucleic acids are eluted and amplified using PCR (polymerase chain reaction). Through iterative rounds of binding, separation, and amplification, sequences with high specificity for the target are enriched, and the most effective binders are selected (see Figure 4). Using sequencing technologies, they can be further analyzed and then characterized according to their binding affinity, specificity, and other functional properties. Advantages of SELEX include high specificity and affinity aptamers for diverse targets with higher chemical stability compared to antibodies. Furthermore, unlike antibodies, aptamers can be produced synthetically. However, aptamer selection using SELEX is a highly time-consuming process, which can take several weeks or months, as multiple rounds of selection are required to achieve high-affinity aptamers [43]. Aptamers are used in molecular biology and biochemistry as tools for protein detection, purification, and modulation of molecular interactions. They can be used in similar ways as antibodies in techniques like immunoprecipitation and ELISA, while also gaining recognition in many fields, particularly in personalized medicine, and targeted therapeutics. Advances in aptamer modification, nanotechnology, and microfluidics are enhancing their practicality for real-world applications [39]. As new technologies improve aptamer stability and broaden their use, aptamers are expected to play an increasingly important role in diagnostics, therapeutics, and research and offer new possibilities for applications in innovative technologies, such as nanopore technology [44, 45].

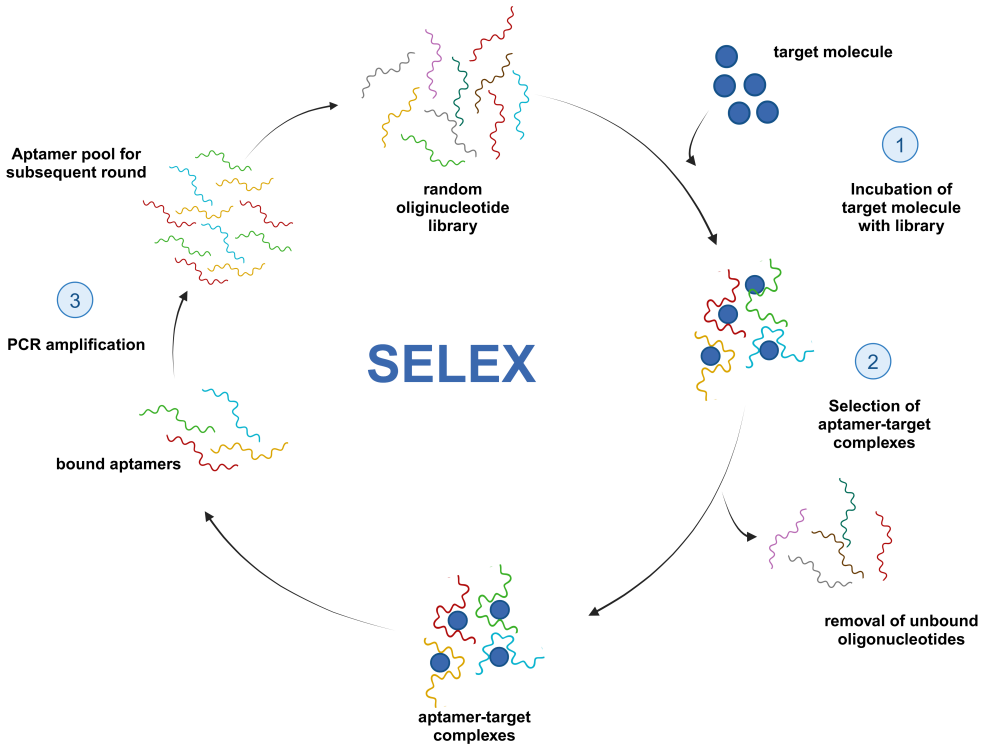

Figure 4: A general scheme of SELEX protocol. **(1)** A random oligonucleotide library is incubated with the desired target molecule. textbf(2) The target-bound aptamers are selected and the unbound oligonucleotides were removed by washing. **(3)** Target-binding aptamers were amplified using PCR (polymerase chain reaction), forming the aptamer pool for the next SELEX cycle. (Created in BioRender.com, accessed on October 2024.)

1.4 Nanopore technology

Nanopore technologies, particularly nanopores, have recently gained attention for small molecule detection [46, 47]. These nanometer-sized pores are utilized in molecular analysis and sensing. By detecting and analyzing molecules based on their size, shape, and charge as they pass through the pore, nanopores offer unique capabilities (see Figure 5). Nanopores can be categorized into three categories **1. biological, 2. solid-state** and **3. hybrid nanopores** [48]. In nature, nanopore-forming proteins, such as ion channels, are embedded in lipid-bilayer membranes, facilitating molecule transport between cells [49]. Solid-state nanopores (ssNPs), in conrast, are artificial holes fabricated in materials like silicon, silicon nitride (SiN) [50], glass [51] or graphene [52]. Originally developed for DNA and RNA sequencing, nanopore technology has recently been adapted for small molecule detection due to its ability to:

1. **Detect individual molecules:** As small molecules pass through or interact with the nanopore, they cause characteristic changes in the ionic current flowing through the pore. These current changes can be detected in real-time, allowing for the identification and quantification of the molecule.

2. **High sensitivity:** Nanopores are sensitive enough to detect even single molecules, making them an excellent platform for applications requiring high sensitivity, such as detecting trace amounts of drugs, hormones, or toxins.

3. **Label-free detection:** Unlike some methods that require molecular labeling (e.g., with fluorescent markers), nanopore-based approaches can detect molecules directly, reducing the complexity and cost of sample preparation.

4. **Versatility:** Nanopores can be used to detect a wide range of molecules, including DNA, RNA, proteins, and small molecules. This versatility makes them suitable for applications in areas like genomics, proteomics, and environmental monitoring.

In summary, nanopores are a highly promising nanotechnology for small molecule detection, offering real-time, sensitive, and label-free analysis. Their applications in biosensing and molecular analytics are rapidly expanding [47, 48].

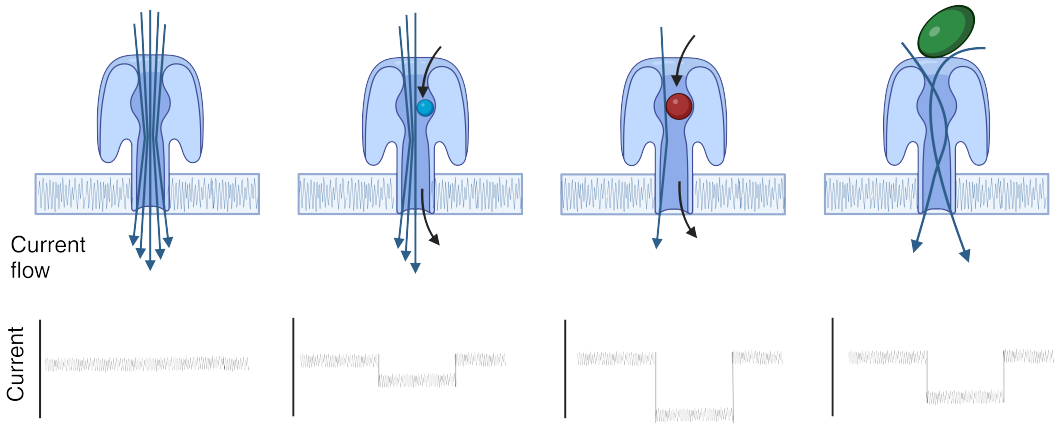

Figure 5: Molecule Sensing via Nanopores. Nanopores are nanometer-sized holes embedded in an electrically resistant membrane through which an electric current is applied. When a molecule passes through the nanopore, it temporarily disrupts the current. The magnitude and duration of this disruption depend on the size, shape, and molecular interactions of the analyte within the pore. Larger molecules cause greater disruptions, while smaller ones result in smaller changes. The shape and translocation time of the molecule also affect the current signal. Based on these current patterns, molecules can be identified and distinguished. (Created in BioRender.com, accessed on February 2025.)

1.4.1 Biological nanopores

Biological pores are typically embedded in planar lipid membranes, liposomes, or polymer membranes within an electrochemical chamber. Large-scale production and purification of various channel proteins can be efficiently achieved using standard molecular biology techniques, resulting in homogenous batches. Additionally, site-directed mutagenesis is possible due to the availability of crystal structures for many channel proteins [48]. The most commonly used pore-forming proteins in molecular biology are α-hemolysin and Mycobacterium smegmatis porin A (MspA). α-hemolysin , an exotoxin secreted by Staphylococcus aureus, is one of the most studied biological nanopores, frequently used in molecular biology, biophysics, and nanopore technology. Its well-characterized structure makes it a model for applications like DNA sequencing, single-molecule sensing, and ion channel research. α-hemolysin forms a mushroom-shaped heptameric transmembrane pore (232.4 kDa), with a cap and a stem domain. The stem forms a transmembrane β-barrel (2.6 nm diameter, 5 nm length), while the cap domain (~3.6 nm diameter, ~5 nm length) extends extracellularly (see Figure 6A). The narrowest point of the pore is at the cap-stem junction (~1.4 nm diameter) [53], limiting its use to the translocation of ssDNA (~1 nm diameter). Genetic or chemical modifications can be applied to the β-barrel to incorporate specific binding elements, making α-hemolysin a stable and

versatile nanopore under laboratory conditions [48]. More recently, MspA has emerged as a promising alternative for α-hemolysin, especially in terms of DNA sequencing. MspA is an octameric, funnel shaped pore forming protein containing a single constriction (~1.2 nm wide, 0.6 nm long) (see Figure 6B) [54]. Similar to α-hemolysin, MspA nanopores can be spontaneously formed in a planar lipid bilayer. However, wildtype MspA needs to be engineered to incorporate all the necessary properties for its use in sequencing applications [55].

Beyond sequencing, biological nanopores have also been extensively studied for the detection of other molecules. Due to its intrinsic nanopore structure, α-hemolysin has shown great potential for stochastic detection of various analytes, including metal ions [56], small organic molecules [57], DNA [58], RNA [59], proteins [60]. Modified protein nanopores hold particular promise for single-molecule sensing. For instance, Wang et al. developed an approach for discrimination of all 20 proteinogenic amino acids and their modifications using an engineered MspA-pore [61]. Likewise, they used the same modified MspA-pores for identification of epigenetic modifications, and nucleotide derivates of natural RNA [62]. Biological nanopores, especially engineered variants, are now powerful tools for single-molecule protein sequencing and small molecule detection.

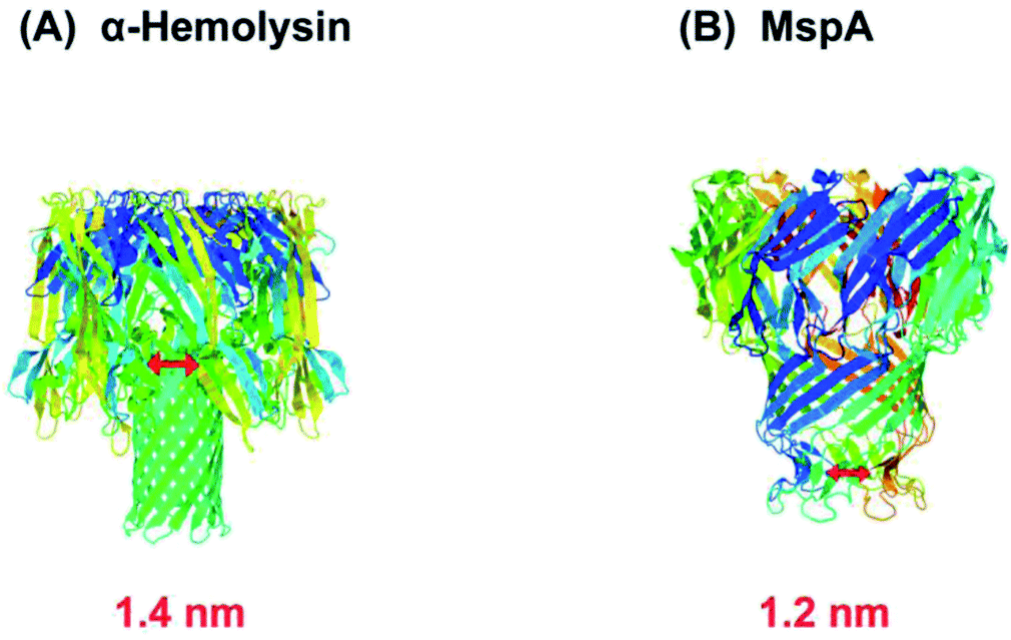

Figure 6: Comparison of the geometries of alpha hemolysin and MspA. A section of Fig. 2A and 2B: alpha-hemolysin (PDB: 3ANZ) and MspA (PDB: 1UUN), from Bhatti et al., Recent advances in biological nanopores for nanopore sequencing, sensing and comparison of functional variations in MspA mutants, RSC Adv., 2021, 11, 28996–29014. Licensed under CC BY-NC 3.0 (https://creativecommons.org/licenses/by-nc/3.0/) [63].

1.4.2 Solid-state nanopores

With advancements in microfabrication technologies, solid-state nanopores (ssNPs) have garnered significant attention due to their tunability, robustness, and potential for a wide range of sensing applications. The first reported fabrication of ssNPs was in 2001 by Li et al., who used a feedback-controlled ion sputtering system to create nanopores [50]. This breakthrough opened the door for a variety of ssNP fabrication methods, each offering different levels of precision, scalability, and control over the nanopore characteristics. Techniques such as ion milling [64], the track-etch method, electron-beam-based decomposition sputtering [65], focused ion beam (FIB) techniques [66], laser ablation [67], electron-beam lithography [68], helium ion microscopy [69], and more recently, dielectric breakdown techniques [70] have all been developed to fabricate ssNPs. An overview of the different fabrication methods is shown in Figure 8. Each of these methods has unique advantages depending on the desired nanopore size, shape, material, and application, allowing researchers to tailor the ssNPs for specific sensing or filtration needs.

A wide range of materials has also been explored for ssNP fabrication, expanding their versatility. Materials such as SiN [71], SiO_2 [65], aluminum oxide (Al_2O_3) [72], boron nitride (BN) [73], graphene [52] and glass [67] have been successfully used to create ssNPs. In recent years, ultrathin membranes, particularly those made from materials like graphene, have also gained attention for their exceptional electrical, mechanical, and chemical properties. Graphene nanopores, fabricated using chemical vapor deposition (CVD) techniques [68, 74], have been extensively studied for biomolecule transport, particularly for DNA sequencing and protein analysis [75, 76].

Among these, SiN and SiO_2 membranes are the most widely used due to their favorable properties, including low mechanical stress and high chemical resistance, making them ideal for nanopore fabrication. The typical process of fabricating ssNPs in SiN or SiO_2 involves low-pressure CVD at high temperatures (around 800°C) to create robust, thin membranes. Photolithography and wet-etching techniques are then employed to define small windows on the silicon side, often measuring 100 × 100 µm or 40 × 40 µm. The nanopore itself is drilled at the center of these windows using a focused electron beam, which precisely sputters atoms from the membrane to achieve the desired pore size. This process allows for exact control over the pore diameter, a critical factor in tailoring ssNPs to the specific requirements of different sensing systems [77]. Standard SiN membranes, typically around 30 nm thick, are particularly popular for applications like DNA translocation studies due to their mechanical robustness and high chemical resistance. However, the negatively charged surfaces of SiN or SiO_2 require the use of high-salt buffers to screen surface charges, ensuring consistent and reliable ionic current measurements. Additionally, SiN nanopores exhibit a linear current-voltage (I-V) relationship even at high voltages, making them ideal for precise molecular sensing under a wide

range of experimental conditions [78].

While SiN and SiO_2 membranes dominate the field, aluminum oxide (Al_2O_3) has emerged as a compelling alternative due to its distinct advantages. Unlike the negatively charged surfaces of SiN and SiO_2, Al_2O_3 surfaces are positively charged, which can enhance signal-to-noise ratios and extend the lifespan of nanopores during sensing experiments. The fabrication of Al_2O_3 membranes with atomic-level precision is made possible through atomic layer deposition (ALD), a technique that enables the creation of ultrathin membranes with precisely controlled thickness. FIB techniques can then be used to fabricate nanopores in these Al_2O_3 membranes, offering tunability in both membrane thickness and pore diameter, which is crucial for optimizing sensitivity and resolution in nanopore-based sensing applications [78].

Moreover, ALD also plays an essential role in surface modification, allowing researchers to coat SiN or SiO_2 nanopores with materials such as Al_2O_3, hafnium oxide (HfO_2), or titanium oxide (TiO_2). These coatings significantly alter the chemical, mechanical, and electrical properties of the nanopores, improving their performance for specific applications [79]. Notably, ALD-coating with HfO_2 has been shown to dramatically increase nanopore stability and longevity, making it a valuable technique for enhancing the durability of ssNPs in long-term experiments [80]. By combining the mechanical strength of SiN or SiO_2 with the improved surface characteristics provided by ALD coatings, researchers can create highly durable and sensitive nanopores that are optimized for a wide range of sensing technologies. In addition to surface coatings using ALD, nanopores can be functionalized with charged functional groups such as amino groups and carboxy groups or whole biomolecules like antibodies or aptamers (see Figure 7). These surface functionalizations can also lead to positively charged surfaces, improving surface characteristicsand enhancing target molecule interaction. For example, antibody-target interactions can prolongtranslocation times, which is crucial for sensitive target detection [81].

Overall, the continued development of advanced fabrication methods and the exploration of novel materials and surface modifications for ssNPs are paving the way for next-generation sensing technologies. From the precision offered by techniques like electron-beam lithography and ALD, to the versatility of materials like SiN, SiO_2, Al_2O_3, and graphene, ssNPs are poised to revolutionize the field of nanopore sensing, enabling applications that were previously unattainable with traditional biological nanopores [82, 83].

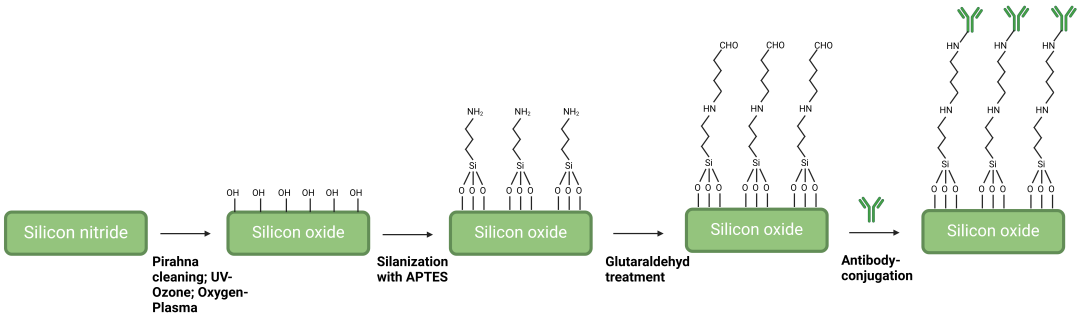

Figure 7: Surface functionalization of ssNPs with antibodies using silanization. The silicon nitride surface is oxidized using piranha acid, oxygen-plasma or UV-Ozone treatment. The resulting oxygen groups can be further conjugated with APTES (3-Aminopropyltriethoxysilane), leading to an amino group on the surface, which can be conjugated to antibodies using glutaraldehyde. (Created in BioRender.com, accessed on October 2024.)

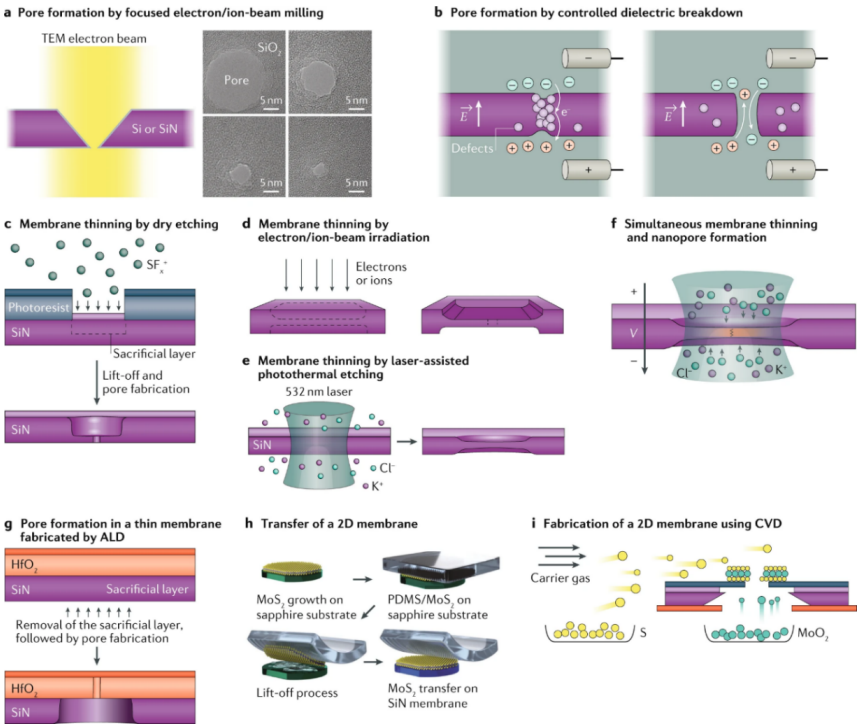

Figure 8: Schematic overview of solid-state nanopore fabrication. a) Focused electron/ion-beam milling of free-standing membranes is a common approach for fabricating sub-10 nm pores (left). The pore size and shape can be monitored in real time during fabrication. A sequence of transmission electron microscope (TEM) images showing nanopore formation in silicon dioxide using an electron beam (right). The electron irradiation leads to a gradual reduction in the size of the nanopore to approximately 3 nm. b) Controlled dielectric breakdown can be used to fabricate pores in membrane materials such as SiN, HfO2 and SiO2. The membrane is immersed in an electrolyte (such as KCl, NaC or LiCl) and exposed to an electric field with intensity comparable to the dielectric strength of the membrane. Structural defects are produced owing to tunnelling leakage current, resulting in the dielectric breakdown of the membrane and in the formation of a nanopore. c–e) Thinning methods for solid-state membranes include dry etching with a patterned protection layer (photoresist) (panel c); electron/ion-beam irradiation (panel d). Helium ion-beam irradiation leads to thinning of both sides of the SiN membrane, which has been attributed to fluidization and ion pressure; laser-assisted photothermal etching (panel e). The process is influenced not only by the laser illumination but also by the composition of the supporting electrolyte. f) The combination of laser-assisted photothermal etching and controlled dielectric breakdown allows for the simultaneous thinning of the membrane and formation of a nanopore. g) Formation of an ultra-thin membrane using atomic layer deposition (ALD). A thin layer of a desired material is deposited on a sacrificial layer using ALD. Etching or removal of the sacrificial layer produces a thin, free-standing membrane; there is a large choice of available deposition chemistries. h,i) Free-standing 2D membranes. 2D materials supported on a sub-micrometre-sized aperture can be prepared via material transfer (panel h) or by directly fabricating the 2D material on the aperture using chemical vapour deposition (CVD) (panel i). Nanopores in single-layer 2D materials have high sensitivity, owing to their near-atomic thickness (graphene: 0.3 nm, BN: 1.1 nm, MoS2: 0.8 nm and WS2: 0.7 nm). PDMS, polydimethylsiloxane. Panel a adapted from ref.37, Springer Nature Limited. Panel b adapted from ref.42, CC BY 4.0. Panel d adapted from ref.74, CC BY 3.0. Panels c, e and f adapted with permission from ref.77, American Chemical Society. Panel h adapted with permission from ref.342, Wiley. Panel i adapted with permission from ref.108, American Chemical Society. Reproduced with permission from Springer Nature [83].

.

1.4.3 Comparison of biological and solid state nanopores for small molecule detection

When comparing ssNPs and bioNPs for small molecule detection, each system offers distinct advantages and faces specific challenges. ssNPs have emerged as a promising and versatile alternative to bioNPs, primarily due to their well-defined geometries, mechanical robustness, and compatibility with various electronic and optical measurement techniques. These features enable ssNPs to be tailored for a wide range of applications, making them highly attractive for researchers working on advanced sensing technologies. ssNPs are typically fabricated using precise techniques such as electron beam lithography, ion milling, and FIB method (see 1.4.2). These fabrication processes allow for the fine-tuning of the nanopore's size, shape, and thickness with remarkable precision, often to within a few nanometers [84]. This high degree of tunability, spanning pore sizes from sub-nanometer dimensions up to hundreds of nanometers, gives ssNPs a distinct advantage in applications where controlling the size and surface properties of the pore is essential for improving sensitivity and resolution. In small molecule detection, where identifying and measuring individual molecules requires fine discrimination, the ability to precisely control these parameters in ssNPs is particularly advantageous. In contrast, bioNPs, such as α-hemolysin or MspA, are naturally occurring protein-based pores with fixed dimensions defined by their biological structure. While bioNPs are effective in many applications, their limited ability to be customized restricts their flexibility in detecting molecules of varying sizes or properties [85].

Another significant advantage of ssNPs lies in their stability under a wide range of chemical and physical conditions. ssNPs made from materials such as silicon nitride (SiN), silicon dioxide (SiO_2), and aluminum oxide (Al_2O_3) are highly resistant to harsh environments. These materials can withstand extreme pH levels, high salt concentrations, and elevated temperatures, conditions that would degrade biological nanopores and their associated lipid bilayer membranes. This chemical and thermal resilience makes ssNPs particularly well-suited for applications in diverse environments, including industrial, environmental, and medical settings where conditions may be less controlled or more demanding [80, 86]. In contrast, bioNPs, rely on delicate lipid bilayers to maintain their structure and are susceptible to degradation in these harsh conditions, limiting their durability and long-term usability [86].

Despite the clear advantages of ssNPs, they also present several significant challenges that must be addressed for them to reach their full potential in small molecule detection. One key limitation of ssNPs is their lower temporal resolution and restricted bandwidth, which arises from ionic current noise generated by the nanopore membrane and its substrate. This noise can interfere with the accuracy and precision of molecule detection, especially when trying to analyze small or subtle molecular events. Achieving high-resolution, real-time sensing remains a technical challenge for ssNPs, requiring advances in both nanopore design and electronic

measurement techniques [87, 88]. In contrast, bioNPs, due to their proteinaceous nature and the uniformity of their lipid bilayer environment, tend to exhibit lower levels of ionic current noise, contributing to better signal-to-noise ratios [89]. This superior noise performance makes bioNPs more effective for high-resolution measurements of single molecules, especially in cases where detecting subtle changes in ionic current is critical. BioNPs' ability to maintain low noise levels allows them to offer improved temporal resolution and bandwidth, enabling more precise detection of molecular interactions over shorter timescales [90]. However, their structural limitations, such as fixed pore size and sensitivity to environmental conditions, still pose challenges in broader applications.

Another challenge ssNPs face is their lack of inherent molecular specificity. BioNPs, being protein-based, have natural molecular recognition capabilities, allowing them to selectively bind or interact with specific target molecules, which is critical in applications like DNA sequencing or the detection of specific proteins. ssNPs, however, lack this built-in specificity. Without surface modifications or functionalization, ssNPs tend to detect a wide array of molecules indiscriminately, making it difficult to identify or quantify specific targets, particularly in complex biological or environmental samples. Functionalizing the surface of ssNPs with chemical groups, antibodies, or other molecular recognition elements can improve their selectivity, but this introduces additional complexity into the fabrication process and may affect nanopore stability or performance. Pore clogging is another issue commonly encountered in ssNP systems. When analyzing biomolecules like DNA, proteins, or other macromolecules, these substances can become lodged in the nanopore, obstructing it and preventing further measurements. Clogging can also lead to signal degradation or inconsistency, reducing the reliability of the data generated from the ssNP [91, 92]. Strategies to mitigate clogging, such as optimizing pore size, modifying surface chemistry, or employing more sophisticated fluidic control, are active areas of research but remain technically challenging.

Mechanical fragility is another concern, particularly for ultrathin ssNP membranes. Nanopores made from materials like SiN or SiO_2, which are often only a few nanometers thick, can be prone to mechanical failure during long-term or continuous sensing applications [80]. This fragility is especially problematic for pores with diameters smaller than 5 nm, which are often necessary for detecting small molecules. These small-diameter nanopores have shorter operational lifespans and are more likely to suffer from surface interactions, such as nonspecific binding or electrostatic effects, further complicating signal interpretation. Although modifying the surface of ssNPs can reduce these issues and improve compatibility with different analytes, it introduces additional fabrication steps and increases the complexity of the overall design.

Another technical hurdle in the development of ssNPs for small molecule detection is the challenge of integrating these nanopores with advanced electronics for real-time, high-throughput sensing. Achieving the necessary precision in both the fabrication of the nanopores and the

design of the accompanying electronic systems is technically demanding. Ensuring device reproducibility across different batches and maintaining high-quality signal processing capabilities are significant obstacles that must be overcome for ssNPs to reach widespread use in practical applications [48, 93].

However, despite these challenges, ssNPs hold immense potential for surpassing bioNPs in small molecule detection. Their flexibility in design, ability to function in harsh environments, and potential for integration into electronic and optical systems make them an attractive platform for developing next-generation sensing technologies. With ongoing advancements in fabrication techniques, surface functionalization, and electronic integration, ssNPs could eventually overcome their current limitations and offer a more versatile, durable, and sensitive alternative to biological nanopores in a wide range of applications, from diagnostics to environmental monitoring to drug discovery.

1.4.4 Hybrid nanopores

In contrast, hybrid nanopores combine the advantageous features of both biological bioNPs and ssNPs, creating a synergistic system that overcomes some of the inherent limitations of each individual type. These hybrid nanopores typically consist of a biological component, usually a pore-forming protein such as α-hemolysin or MspA, embedded within a solid-state material like SiN, graphene, or another thin synthetic membrane [94]. This unique combination aims to merge the highly selective and functional properties of biological pores with the durability, stability, and tunability of solid-state materials. As a result, hybrid nanopores are emerging as a powerful platform for advanced applications, including DNA sequencing, molecular sensing, and single-molecule detection, offering greater flexibility and versatility than either bioNPs or ssNPs alone [89].

One of the major benefits of hybrid nanopores is that they offer the precise molecular specificity of biological pores while also addressing the limitations associated with their fragility. Biological nanopores, although highly functional and capable of distinguishing individual molecules, are prone to degradation under harsh conditions such as extreme pH levels, high temperatures, or varying ionic strengths. For instance, biological pores have very small diameters (1.2 nm for MspA and 1.4 nm for α-hemolysin), making them excellent for detecting small molecules or DNA strands with high precision [53, 55]. However, when exposed to environments outside their optimal conditions, such as high pH or temperature, these proteins can denature or lose functionality, limiting their operational range. Incorporating a synthetic membrane, such as SiN or graphene, into the hybrid nanopore system helps to mitigate these issues by providing a more durable scaffold. The solid-state component enhances the overall stability of the system, allowing the biological nanopore to function in more diverse and potentially harsher

environments without significant loss of performance [89, 94]. Additionally, the synthetic membrane introduces a broader range of customization options, such as precise control over the membrane's thickness, surface chemistry, and electrical properties, which can be fine-tuned for specific applications. This level of control is particularly beneficial for optimizing the interaction between the biological pore and the translocating molecules, ultimately improving the sensitivity and resolution of the system. The solid-state framework also facilitates integration these hybrid systems with various detection technologies, including electronic or optical readouts, further expanding their applicability in complex sensing environments [48, 95].

One of the best-known applications of hybrid nanopores is in DNA sequencing, specifically the MinION® sequencer developed by Oxford Nanopore Technologies (ONT). Introduced in 2014, the MinION® was the first commercially available nanopore-based sequencing device, and it revolutionized the field of genomics by providing a portable, real-time, and affordable sequencing platform. The MinION® utilizes bacterial protein nanopores, either α-hemolysin or MspA, embedded within a synthetic membrane, creating a hybrid nanopore system. The sequencing principle behind the MinION® device is based on the detection of changes in an electrical current as a molecule, typically DNA or RNA, translocates through the biological nanopore. An electrical current is applied across the synthetic membrane, which is highly resistant, and a baseline current is measured based on the size and shape of the nanopore. When a negatively charged molecule, such as a strand of DNA, translocates through the nanopore, it causes a temporary disruption in the current. The magnitude and duration of this disruption depend on the specific nucleotide sequence of the DNA passing through the pore, enabling the device to detect the identity of each base as the molecule is sequenced (see Figure 9). The ability of the MinION® to sequence DNA in real time, without the need for amplification or labeling, is a significant advancement in the field of genomics, providing unprecedented access to large-scale sequencing data in a portable format [45, 48].

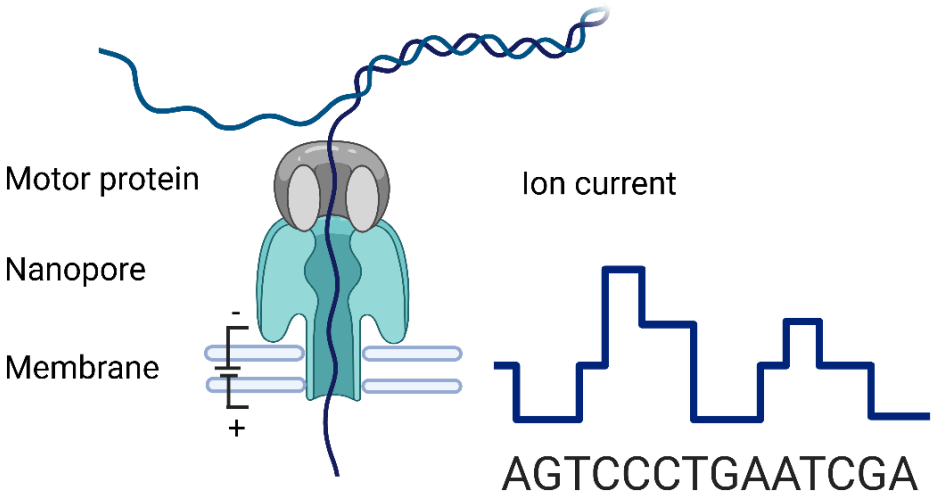

Figure 9: Nanopore sequencing principle. dsDNA is unwound by the motor protein and one strand is translocated through the nanopore to the trans side (positive pol). (Created in BioRender.com, accessed on October 2024.)

Hybrid nanopores offer additional advantages over conventional biological pores or solid-state systems in several areas. In addition to DNA and RNA sequencing, hybrid nanopores are being explored for a wide range of applications in molecular sensing. Their ability to detect single molecules with high precision makes them valuable tools for studying protein folding, enzyme activity, and biomolecular interactions [96, 97]. Furthermore, the integration of solid-state components provides opportunities for hybrid nanopores to be incorporated into lab-on-a-chip devices, enabling high-throughput screening of molecules in real-time. This versatility makes hybrid nanopores a promising technology not only for genomic research but also for diagnostics, drug development, and environmental monitoring [98].

1.4.5 Combination of aptamers and nanopores for the detection of small molecules

To overcome existing challenges in small molecule detection using nanopores, the combination of aptamers and nanopores has become a promising strategy. Given the extensive research on nucleic acid sensing across various types of nanopores, aptamers (that are small ssDNA or ssRNA molecules) serve as ideal carrier molecules for this purpose. As described in section 1.3, aptamers are short, single-stranded DNA or RNA molecules that can fold into unique three-dimensional structures, allowing them to bind selectively to specific target molecules, such as proteins, small molecules, or ions, with high affinity. When integrated with nanopores, aptamers can provide a means of molecular recognition, improving the functional capabilities of both ssNPs and bioNPs [99]. There are several ways how aptamers can be used in small molecule detection using nanopores [100–104]. One opportunity is the chemical surface modification with aptamers of the inner wall or the proximity of the pore entrance. Upon binding with a target molecule the aptamer undergoes conformational changes that either block or alter the ionic current passing through the nanopore, generating a detectable signal [44]. This binding event is highly specific, allowing the nanopore to detect specific molecules based on aptamer-target interactions. Otherwise, the interaction between the target molecule with its aptamer can cause a change in the current signal. These signals can provide real-time data on the presence, concentration, and even the kinetics of the binding event. Using aptamer carriers can significantly enhance the selectivity of nanopore-based sensors, enabling the detection of specific small molecules, that might otherwise pass through the nanopore unrecognized or may only generate subtle current changes [104].

One of the key benefits of aptamer-functionalized nanopores is enhanced molecular specificity. While solid-state nanopores are inherently non-selective, aptamer integration allows for selective detection of particular molecules, such as drugs, toxins, or biomarkers, even in complex mixtures. Furthermore, nanopores equipped with aptamers can provide a label-free approach for small molecule detection in real-time, avoiding the need for fluorescent or other labeling techniques commonly needed for molecular sensing [99]. This makes aptamer-nanopore sensing valuable for diagnostics, environmental analysis, and drug discovery. As aptamers can be designed to detect a wide range of target molecules, including small molecules, proteins, nucleic acids, and even ions, this approach is versatile. The highly specific binding between an aptamer and its target often results in clear, quantifiable changes in ionic current, allowing detection at very low concentrations. This makes aptamer-functionalized nanopores particularly useful in applications requiring high sensitivity, such as detecting trace amounts of biomolecules or environmental toxins. Nevertheless, there are also some challenges to overcome, when combining aptamers with nanopores. One key concern is aptamer stability, as their structure and binding capabilities are sensitive to environmental factors, like pH, temperature and

ionic strength, to maintain their folding and binding capabilities [105]. Also, if attached to the nanopores surface, the aptamer immobilization should not interfere with its target binding ability. While aptamers improve specificity, the signal-to-noise ratio may still be a concern, especially when detecting small molecules with weak or subtle ionic current changes. This challenge is more pronounced in solid-state nanopores, where background noise from the membrane or pore structure may obscure detection signals.

In summary, the combination of aptamers and nanopores leverages the strengths of both technologies, enhancing the selectivity of nanopore sensors while preserving their versatility, sensitivity, and label-free detection capabilities. While challenges remain in terms of stability, functionalization, and signal clarity, aptamer functionalized nanopores hold significant potential for highly selective small molecule detection, especially in complex samples. This makes them a promising tool for a wide range of sensing applications, from diagnostics to environmental monitoring.

1.5 Magnetic beads

Magnetic beads are widely utilized in biological assays for applications such as nucleic acid purification [106], protein isolation [107], immunoassays [108], and cell sorting [109]. These beads, typically composed of superparamagnetic iron oxide particles embedded in a polymer matrix, can be manipulated by external magnetic fields, making them ideal for separating biological molecules or cells [110]. For nucleic acid purification, beads are coated with functional groups (e.g., silica, oligo-dT) that bind nucleic acids. Upon sample lysis, nucleic acids attach to the beads, and a magnetic field is applied to pellet the bead-bound nucleic acids, allowing for the removal of supernatant and washing of contaminants. Purified nucleic acids are then eluted and used for downstream applications such as PCR, sequencing, or cloning [111].

Magnetic beads can also be functionalized with ligands like antibodies or enzymes, facilitating protein isolation or enhance immunoassays. In immunoprecipitation assays, beads coated with specific antibodies capture target proteins from a mixture. After washing, the protein-bead complex is magnetically separated from the sample. This method is commonly used for protein identification, interaction studies, or Western blot analysis. Additionally, beads can be coated with nickel ions (Ni-NTA) to selectively bind histidine-tagged recombinant proteins [108]. The magnetic separation process simplifies purification compared to traditional chromatography methods. Magnetic beads also enhance immunoassays, such as Magnetic bead-based ELISAs, where antibodies or antigens are attached to the bead surface rather than a solid substrate. After binding the target analyte and detection antibodies, the beads are magnetically separated, washed, and analyzed, offering faster processing times and increased sensitivity compared to conventional ELISAs [112].

In small molecule detection, magnetic beads provide improved sensitivity, specificity, and speed. Small molecules, including drugs, hormones, and environmental toxins, are often difficult to detect due to their small size and low abundance (see 1.1). Magnetic beads help overcome these challenges through a variety of assay techniques e.g., competitive immunoassays (see 1.2). Here, beads functionalized with antibodies or antigens bind the small molecule of interest, while a labeled small molecule competes for bead binding. A magnetic field is applied to separate bead-bound complexes, and the unbound molecules are washed away. The signal from the labeled molecule, which decreases in the presence of the target, is measured to quantify the small molecule concentration in the sample (see Figure 10). This method is widely used for drug testing, hormone assays, and toxin detection [8]. Magnetic beads are also integrated into biosensor platforms for small molecule detection. These biosensors use electrochemical, optical, or mass-sensitive methods to quantify small molecule binding events, with magnetic beads enhancing assay sensitivity by preconcentrating small molecules from complex samples like blood or urine. This reduces detection limits and allows for smaller sample volumes, which is especially important in medical diagnostics when sample availability is limited [113].

In conclusion, although magnetic beads are more expensive than traditional methods, they are highly versatile, offering superior sensitivity, automation potential, and compatibility with various biosensing technologies. They are particularly valuable in fields like drug testing, environmental monitoring, and therapeutic drug monitoring, where detecting low-abundance small molecules with precision is critical.

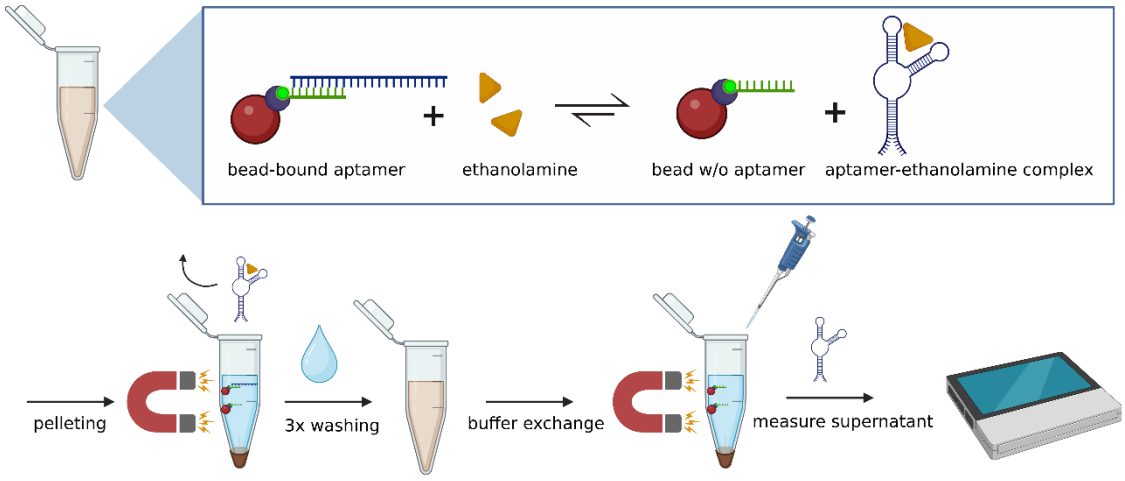

Figure 10: Principle of a magnetic bead based competitive assay. The biotinylated EA aptamer binding complement is covalently attached to streptavidin coupled magnetic beads and the EA aptamer is hybridized to its complementary strand. When ethanolamine is added, the aptamer is displaced from its complementary strand to form the ethanolamine-aptamer complex. Beads can be pelleted with a magnet and the supernatant containing the displaced aptamer can be removed. After washing, the remaining bead-bound aptamer can be removed from the beads with ONT-Flush buffer and the amount of aptamer in the supernatant can be measured using the MinION®-device. (Created in BioRender.com, accessed on October 2024.)

1.6 L-kynurenine as biomarker

L-kynurenine is one of the smallest molecules (208 g/mol) recognized by antibodies in immunoassays, making it a valuable tool for developing POC diagnostic assays. Kynurenine, a key metabolite in the tryptophan degradation pathway, is associated with various inflammatory, metabolic, oncogenic, and psychiatric disorders [114–116]. While some tryptophan is converted into serotonin [117], approximately 95% of dietary tryptophan is processed through the kynurenine pathway (KP) via the enzyme family indoleamine-2,3-dioxygenases (IDOs) [118, 119]. This pathway involves a cascade of degradation enzymes that ultimately produce quinolinic acid as the final product [120]. IDO enzyme activity is regulated by immune factors, including pathogenic microorganisms, lipopolysaccharides (LPS) [121, 122], and inflammatory cytokines like IL-1 and TNF-α [123, 124]. Elevated kynurenine levels have been shown to modulate immune activation and display anti-inflammatory effects through a feedback mechanism [125].

This link between inflammation and increased serum kynurenine levels, driven by IDO upregulation, highlights kynurenine as a promising biomarker for clinically relevant inflammatory conditions. For instance, in patients with chronic kidney disease (CKD). in the pre-dialysis stage, IDO activity and therefore, serum kynurenine levels are elevated to 3.9 ± 2.1 μM, increasing to 5.6 ± 2.3 μM with CKD progression, driven by chronic inflammation [126, 127]. Similarly, elevated kynurenine levels correlate with inflammatory responses following kidney transplantation, inversely relating to kidney function [128]. In a 2007 study, Buczko et al. observed reproducible correlations between saliva and serum kynurenine levels in uremic patients, indicating saliva as a viable alternative for kynurenine measurement [129]. Given the relationship between inflammation, IDO expression, kidney failure, and transplant rejection [130, 131], and supporting literature that highlights kynurenine as a biomarker for renal allograft failure [132], this study explores saliva-derived kynurenine as a potential biomarker for kidney transplant rejection. Notably, patients with transplant rejection exhibit L-kynurenine levels of 17.4 $\pm$ 8.4 μM in serum and 4.6 $\pm$ 1.6 μM in saliva, compared to control groups with levels of 2.7 $\pm$ 0.4 μM in serum and 0.7 $\pm$ 0.4 μM in saliva [128].

Beyond transplant rejection, elevated kynurenine levels are also linked to titanium dental implant failure, impaired bone osseointegration processes [133], and complications with left ventricular assist devices, further connecting kynurenine with implant failure [134].

In clinical trials, kynurenine quantification has primarily relied on LC-MS [135] or GC-MS [136] methods, which are often impractical for rapid diagnosis. Alternative approaches include fluorescent gold nanoclusters that detect physiological levels of kynurenine through a quenching mechanism, as demonstrated by Ungor et al. (2019) [137]. Another method, developed by

Klockow et al. (2013), uses fluorescently labeled kynurenine derivatives with a coumarin aldehyde scaffold to produce fluorescence based on pH changes [138]. Additional rapid testing approaches focus on quantifying IDO activity rather than directly measuring kynurenine [139], offering potential for faster, more accessible diagnostics.

1.7 Ethanolamine as biomarker

Ethanolamine (EA) is a small organic molecule (61.08 g/mol) that has gained attention as an important analyte in both environmental chemistry and life sciences due to its crucial role in the metabolism of humans and plants (see Figure 11) [140–142]. As a key component of phospholipids, particularly phosphatidylethanolamine (PE), EA is vital for maintaining cellular membrane structure and function. It also participates in several metabolic pathways, including lipid metabolism and neurotransmitter synthesis [143]. Given its involvement in these biological processes, EA shows great promise as a biomarker for various diseases and physiological conditions.

In healthy adults, the average concentration of free EA in blood is around 2 μM (ranging from 0 to 12 μM), while significantly higher levels are found in other body fluids, such as breast milk (46.2 ± 18.1 μM), cerebrospinal fluid (14.1 ± 3.0 μM), and saliva (135.99 ± 96.22 μM) [144]. In contrast, newborns also exhibit much higher blood levels, averaging 52.3 μM (range 26.2–91.7 μM). A decrease in PE, and by extension EA, has been linked to the development and progression of several neurodegenerative diseases, including Alzheimer's [145], Parkinson's [146], and Huntington's diseases [147], as well as mitochondrial dysfunction [148].

EA has been studied as a potential marker for liver dysfunction and diseases such as non-alcoholic fatty liver disease (NAFLD) and liver fibrosis. In conditions affecting the liver, altered lipid metabolism can lead to abnormal EA levels in the blood or tissues [149]. Elevated EA levels have been associated with liver injury, reflecting disruptions in the synthesis and turnover of membrane lipids [150]. Additionally, EA is also linked to the central nervous system as a precursor in the synthesis of acetylcholine, an essential neurotransmitter involved in learning and memory. Dysregulation of EA levels have been noted in certain neurodegenerative disorders, such as Alzheimer's disease. Abnormal levels of EA in the cerebrospinal fluid (CSF) or blood may indicate disruptions in phospholipid metabolism or neurotransmitter production, both of which play critical roles in brain function [147]. In cancer biology, altered EA metabolism can be indicative of tumor growth and progression. Tumor cells often exhibit changes in lipid metabolism to support rapid cell division and growth. Studies have shown that EA levels can be elevated in certain types of cancer, such as breast and prostate cancers, making it a potential biomarker for tumor diagnosis or monitoring therapeutic responses [151, 152]. Since EA is involved in lipid metabolism, its levels can be altered in metabolic diseases like obesity, diabetes, and cardiovascular disease. It may serve as a biomarker for metabolic health by reflecting changes in lipid metabolism that occur in these conditions. Elevated serum EA levels have been linked to insulin resistance, making it a potential marker for assessing metabolic syndrome and related disorders [146]. Additionally, abnormal EA levels have been observed in patients with chronic kidney disease (CKD), possibly reflecting disruptions in lipid metabolism due to impaired kidney function. Measuring EA in blood or urine may provide insight into the

progression of CKD and help in evaluating treatment efficacy. Furthermore, EA is also linked to the inflammatory response. In conditions involving inflammation, such as autoimmune diseases or infections, elevated levels of EA can indicate increased membrane turnover due to cell damage or immune activation [141, 153]. Therefore, EA serves as a versatile biomarker, particularly in diseases related to lipid metabolism, liver function, neurological conditions, cancer, and inflammation. Monitoring its levels in blood, urine, or cerebrospinal fluid may provide valuable diagnostic and prognostic information across a wide range of medical conditions.

Despite its potential as a biomarker, detection of small molecules such as ethanolamine remains challenging and labor-intensive with conventional analytical techniques such as HPLC and LC-MS [154]. While various methods have been explored in the literature [155–158] , achieving both high accuracy and sensitivity in ethanolamine quantification is difficult due to its high polarity and low molecular weight, which complicates retention and separation from other matrix components [159]. Therefore, the development of alternative detection methods for ethanolamine is becoming increasingly critical.

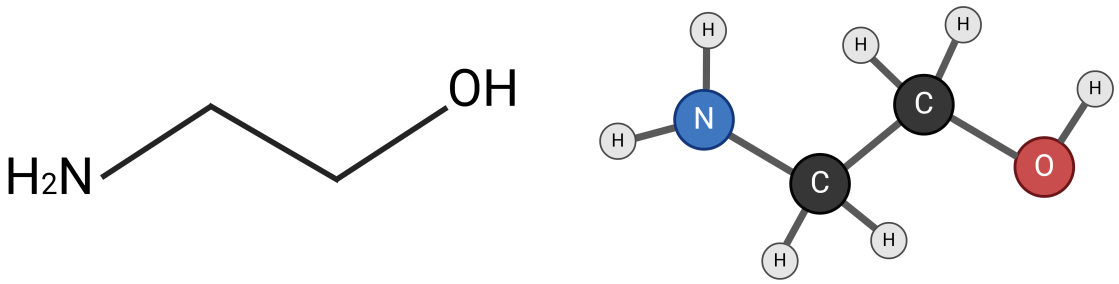

Figure 11: Chemical structure of ethanolamine. Ethanolamine is a small organic molecule (MW 61.08 g/mol), containing two functional groups, a hydroxyl group and an amino group. (Created in BioRender.com, accessed on October 2024.)

1.7.1 Ethanolamine aptamer

As shown in 1.3 aptamers are short, synthetic produced ssNA (DNA or RNA) that specifically bind to small target molecules with high affinity, by folding into three-dimensional structures, enabling them to selectively recognize target molecules, much like antibodies. Various aptamers against small molecules have been reported in the literature [160]. Ethanolamine, as small organic molecule (MW = 61.08 g/ mol) is one of the smallest aptamer targets so far [161]. As shown in the previous section ethanolamine holds biological, medical and environmental relevance. A few DNA aptamers were previously reported for binding ethanolamine with a dissociation constant (Kd) as low as 6 nM. Mann et al. (2005), were the first who identified two different aptamer structures (#14.3 and #9.4) which showed high binding affinity and selectivity of ethanolamine over chemically similar target molecules (e.g., propylamine, ethanol, glycine). Both structures consist of a ssDNA aptamer with 96 nucleotides folding into a stem-loop secondary structure [162]. The target binding region of the aptamer could be determined using truncated aptamer sequences for binding studies [161]. It is a guanine-rich sequence segment with a length of 16 nucleotides. Secondary structure predictions show that this target-binding aptamer region is located in a loop region of the aptamer (see Figure 12). The three-dimensional folding of this aptamer region forms a G-quadruplex structure. G-quadruplexes are formed by the stacking of coplanar guanine tetrads via Hoogsteen hydrogen bonds [163]. The coplanar architecture of G-quadruplexes has noticeable van der Waals attraction and many aromatic planar ligands can interact with this guanine chamber [164]. The target ethanolamine is presumably bound by loop structures within the G-quadruplex [165]. Additionally, some truncated EA-aptamer variants were reported to show sufficient binding affinity and selectivity against EA. In particular, the 42-nucleotide long variant from the EA-aptamer #14.3 (EA-aptamer #14.3K42) showed good performance in EA binding assays, especially in competitive binding assays [166, 167].

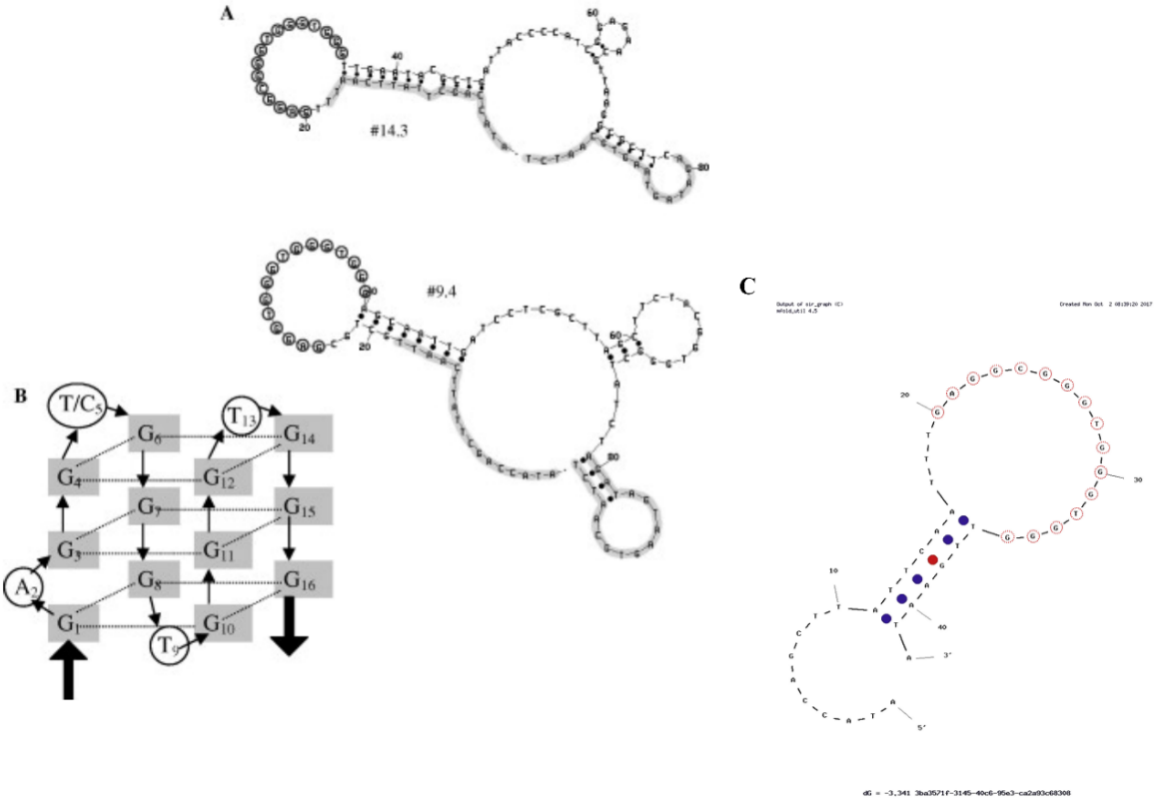

Figure 12: Ethanolamine aptamer structure. Combined figure of: (A) Secondary structure of aptamers #14.3 and #9.4. The primer regions (nucleotides 1–18 and 79–96) are highlighted in grey, and the consensus sequence (nucleotides 20–35 for version 14.3 and 24–39 for version 9.4) is marked by circles. The primer regions were always arranged in stem-loop structures, whereas the consensus sequences were found in a single-stranded loop. Modified from Mann et al., 2005, In vitro selection of DNA aptamers binding ethanolamine, Biochemical and Biophysical Research Communications, Vol. 338, Issue 4, Pages 1928-1934, Copyright (2005), with permission from Elsevier [162]. **(B)** G-quadruplex structure. The consensus sequence of 16 nucleotides was characterized by several G-triplets. Thus, the three-dimensional shape of this consensus sequence could be a threefold stacked G-quadruplex structure. The image shows one possible conformation of the nucleotides. Modified from Mann et al., 2005, In vitro selection of DNA aptamers binding ethanolamine, Biochemical and Biophysical Research Communications, Vol. 338, Issue 4, Pages 1928-1934, Copyright (2005), with permission from Elsevier [162]. **(C)** Predicted secondary structure of the ethanolamine aptamer with 42 nucleotides (EA#14.3K42), a truncated version of the original 96nt (EA#14.3) aptamer. Modified from Mahmoud, M., Laufer, S., & Deigner, H.-P., Data for homogeneous thermofluorimetric assays for ethanolamine using aptamers and a PCR instrument, Data in Brief, 2019. https://doi.org/10.1016/j.dib.2019.103946. Licensed under CC BY 4.0 (https://creativecommons.org/licenses/by/4.0/).

2 Objectives

Detecting small molecules is essential in fields such as molecular diagnostics, drug development, disease monitoring, as well as environmental and food analysis. Current technologies rely on advanced spectroscopic and chromatographic methods like HPLC, LC-MS, and GC-MS, which, while effective, are costly, time-intensive, and limited to laboratory settings.

The aim of this dissertation is to develop novel, label-free detection methods that enable rapid and accessible quantification of small molecules, offering a faster and more cost-effective alternative to traditional chromatographic techniques. Given the challenges in detecting small molecules due to their lack of binding sites, this research explores three innovative approaches.

The first approach focuses on the development of a **competitive magnetic bead assay** for **L-kynurenine quantification**. Using a fluorescently labeled competitor and one of the few existing antibodies specific to L-kynurenine, this assay enables direct measurement through fluorescence signals. Additionally, its application in complex biological matrices, such as saliva, was evaluated to assess both the sensitivity and practicality of the method for point-of-care applications.

In the second approach, a **ready-to-use protein nanopore platform** for small molecule **quantification of ethanolamine** was implemented using a magnetic bead-based strand-displacement assay. This introduces an alternative approach that bypasses the need for specific antibodies by employing ssDNA aptamers. The assay utilizes hybrid protein nanopores within a synthetic membrane, tested on the commercial MinION® nanopore sequencer, where current disruptions are measured as aptamers translocate through the pores. This section critically evaluates the adaptability of commercially available nanopores for small molecule detection via aptamers, highlighting both their potential and current limitations.

The third approach explores the potential of **solid-state nanopores for small molecule detection**, leveraging insights from hybrid nanopore experimentation. This section addresses fabrication and stability challenges, surface modification techniques, and sensor optimization to refine nanopore-based molecular detection. Together, these methods aim to advance small-molecule analysis techniques, contributing to faster, more accessible, and cost-efficient biochemical assays.

3 Materials and Methods

3.1 Part 1: L-kynurenine fluorescence-based competitive immunoassay

The first part, aimed to develop a rapid test for L-kynurenine a potential biomarker for kidney transplant failure. Therefore, a fluorescence-labelled L-kynurenine derivate was synthesised, characterized and its binding ability to a bead-bound L-kynurenine antibody was investigated. Further a competitive bead-based immunoassay for native kynurenine was designed using the fluorescence derivate as competitor.

3.1.1 General experimental

Thin-layer chromatography (TLC) was performed using Silica Gel 60 F254 plates (Merck) with a layer thickness of 0.2 mm. Visualization was achieved either by UV light irradiation at 254 nm or by charring with a 1 % potassium permanganate ($KMnO_4$) solution in 1 N sodium hydroxide (NaOH). Flash column chromatography (FC) was carried out using M&N Silica Gel 60 (particle size 0.063–0.200 mm). ^{1}H and ^{13}C NMR spectra were recorded on Bruker Avance I 200 (200 MHz) and Avance II 400 (400 MHz) spectrometers (both Bruker, Billerica, MA, USA), or on a Varian Unity 500 (500 MHz) spectrometer (Varian Inc., Palo Alto, CA, USA). Chemical shifts are reported in parts per million (ppm) relative to the residual solvent signals ($CDCl_3$: $\delta_H = 7.26$ ppm, $\delta_C = 77.0$ ppm; DMSO-d_6: $\delta_H = 2.49$ ppm, $\delta_C = 39.7$ ppm). Signal assignments were made based on first-order analysis and, where applicable, supported by 2D ^{1}H,^{1}H and ^{1}H,^{13}C correlation spectroscopy. Coupling constants are given in Hertz (Hz). UV/Vis spectra were recorded on a PerkinElmer Lambda XLS+ UV/Vis spectrophotometer (PerkinElmer, Waltham, MA, USA) using a 10.00 mm quartz cuvette. Fluorescence measurements were conducted with a Tecan Infinite M200 plate reader in commercially available 96-well multiwell plates. All chemicals and reagents were obtained from Acros Organics, Alfa Aesar, Sigma-Aldrich, Carl Roth, Carbolution, or ABCR and used without further purification.

3.1.2 Synthesis of kynurenine–rhodamine B conjugates

The synthesis of the kynurenine–rhodamine B conjugates used in this study was carried out by a colleague and has previously been described in detail in [2]. The following text is reproduced with minor editorial adjustments from that publication, which is licensed under Creative Commons CC BY 4.0:

***(1)* [6-Diethylamino-9-(2-prop-2-ynyloxycarbonyl-phenyl)-xanthen-3-ylidene] diethylammonium; Chloride:**

Rhodamine B (10 g, 20.9 mmol, 1 eq) was dissolved in dry CH_2Cl_2 (250 ml) under a nitrogen atmosphere. EDC (4.4 g, 22.99 mmol, 1.1 eq) and DMAP (0.51 g, 4.18 mmol, 0.2 eq) were added, and the reaction mixture was stirred at room temperature for 15 minutes. Propargyl alcohol (1.33 ml, 22.99 mmol, 1.1 eq) was then introduced, and stirring was continued overnight at ambient temperature. The reaction mixture was washed twice with 1 M HCl (2 × 250 ml) followed by a wash with brine (250 ml). The organic phase was dried over Na_2SO_4 and concentrated under reduced pressure to yield the crude product. Purification by flash column chromatography (CH_2Cl_2:MeOH 9:1) afforded the desired compound as a violet solid (6.08 g, 56 % yield).

Spectroscopic data: ^{1}**H-NMR** ($CDCl_3$, 400 MHz): 8.66 (d, J = 7.9 Hz, 1H, aromatic H), 7.88 (t, J = 7.6 Hz, 1H, aromatic H), 7.78 (t, J = 7.7 Hz, 1H, aromatic H), 7.38 (d, J = 7.6 Hz, 1H, aromatic H), 7.09 (d, J = 9.4 Hz, 1H, aromatic H), 6.95 (d, J = 9.6 Hz, 1H, aromatic H), 6.88 (s, 1H, aromatic H), 4.65 (d, J = 1.3 Hz, 2H, CH_2), 3.68 (q, J = 7.1 Hz, 8H, CH_2), 2.46 (s, 1H, CH), 1.36 (t, J = 7.1 Hz, 12H, CH_3).

^{13}**C-NMR** (DMSO-d_6, 50 MHz): 164.4 (C(=O)O), 157.6, 155.6, 134.0, 133.8, 131.3, 131.3, 131.0, 129.3, 115.1, 113.4, 107.4, 96.4 (aromatic C), 78.5 (C), 77.8 (CH), 53.3, 45.8 (CH_2), 12.9 (CH_3).

***(2)* 4-(2-Amino-phenyl)-2-tert-butoxycarbonylamino-4-oxo-butyric Acid:**

The amino group of kynurenine was protected using Boc chemistry under Schotten–Baumann conditions: Kynurenine (500 mg, 2.4 mmol, 1 equiv) was dissolved in a 1:1 mixture of water and THF containing NaOH (288 mg, 7.2 mmol, 3 equiv). Once the solution became clear, Boc_2O (1.55 ml, 7.2 mmol, 3 equiv) was added dropwise at 0 °C. The reaction was monitored by TLC, and full conversion was achieved after 90 minutes. Acidification with 10% HCl followed by three extractions with ethyl acetate, drying of the organic phase, and removal of solvent yielded the crude product as a yellow oil. Purification by column chromatography (ethyl acetate) afforded the pure compound as a yellowish powder (327.7 mg, 44% yield).

Spectroscopic data: ^{1}**H-NMR** (400 MHz, $CDCl_3$): 7.73 (d, J = 8.0 Hz, 1H, aromatic H), 7.34 (t, J = 7.6 Hz, 1H, aromatic H), 6.83–6.72 (m, 2H, aromatic H), 5.64 (d, J = 8.7 Hz, 1H, CH), 4.67 (ddd, J = 12.8, 8.5, 4.3 Hz, 1H, CH), 3.80–3.69 (m, 2H, CH_2), 3.53 (dd, J = 18.0, 3.8 Hz, 1H, CH), 1.45 (s, 9H, 3×CH_3).

^{13}**C-NMR** (100 MHz, $CDCl_3$): 199.54 (aromatic C=O), 172.43 (carboxylic acid C=O), 155.68 (Boc carbonyl), 149.45, 134.96, 131.08, 125.83, 118.10, 116.73 (aromatic C), 69.98 (Boc tert-butyl C), 52.60 (CH), 41.47 (CH_2), 28.34 (CH_3).

(3) **[3-(2-Amino-phenyl)-1-(2-2-[2-(2-azido-ethoxy)-ethoxy]-ethoxy-ethylcarbamoyl)-3-oxo-propyl]-carbamic Acid Tert-Butyl Ester:**

Boc-protected kynurenine **(1)** (318.9 mg, 1.03 mmol, 1 equiv) and the corresponding azido linker (248.68 mg, 1.14 mmol, 1.1 equiv) were dissolved in dichloromethane (50 ml). EDC (197.45 mg, 1.03 mmol, 1 equiv) and DMAP (25.17 mg, 0.206 mmol, 0.2 equiv) were added, and the reaction mixture was stirred at room temperature for 48 hours. The mixture was washed three times with 2 M NaOH (80 ml), followed by a brine wash (80 ml). After drying over sodium sulfate and solvent removal, the crude product was obtained. Purification by column chromatography using ethyl acetate yielded the pure compound as an orange solid (175.11 mg, 33% yield), which was used directly in the subsequent step without further characterization.

(4) **(9-2-[1-(2-2-[4-(2-Amino-phenyl)-2-tert-butoxycarbonylamino-4-oxobutyrylamino]-ethoxy-ethyl)-1H-[1,2,3]triazol-4-ylmethoxycarbonyl]-phenyl-6-diethylamino-xanthen-3-ylidene)-diethyl-ammonium Salt:**

Azido-functionalized Boc-L-Kynurenine **(3)** (166 mg, 326.6 µmol, 1 equiv) and propargyl rhodamine B **(1)** (169 mg, 326.6 µmol, 1 equiv) were dissolved in 30 ml of a solvent mixture of CH_2Cl_2/MeOH/H_2O (10:10:3). To this solution, aqueous $CuSO_4$ (262 µL, 0.5 M, 130.64 µmol, 0.4 equiv), TBTA (18 mg, 32.66 µmol, 0.1 equiv), and sodium ascorbate (142 mg, 718.52 µmol, 2.2 equiv) were added. The reaction mixture was then heated at 60 °C for 16 hours. After cooling, 20 ml of deionized water was added, and the mixture was extracted three times with 50 ml portions of CH_2Cl_2. The combined organic layers were dried over Na_2SO_4 and concentrated under reduced pressure. Purification by column chromatography (CH_2Cl_2/MeOH 3:1) afforded the pure product as a pink solid (302.5 mg, 90% yield).

Spectroscopic data: ^{1}**H-NMR** (DMSO, 500 MHz): 8.20 (dd, $J = 7.9, 1.0$ Hz, 1H, Ar–H), 7.91–7.85 (m, 3H, Ar–H), 7.83–7.79 (m, 2H, Ar–H), 7.47 (dd, $J = 7.6, 0.8$ Hz, 1H, Ar–H), 7.08–7.00 (m, 2H, Ar–H), 6.97–6.90 (m, 5H, Ar–H), 5.04 (s, 2H, Ar–CH_2), 4.65 (d, $J = 2.4$ Hz, 1H, CH_2), 4.44 (t, $J = 5.2$ Hz, 2H, Triazol–CH_2), 3.74 (t, $J = 5.2$ Hz, 2H, O–CH_2), 3.63 (dd, $J = 13.9, 6.7$ Hz, 8H, 4× RhB–CH_2), 3.48–3.45 (m, 2H, O–CH_2), 3.44–3.40 (m, 6H, 3× O–CH_2), 3.30 (t, $J = 6.4$ Hz, 2H, O–CH_2), 3.00 (dd, $J = 12.0, 6.0$ Hz, 2H, CH_2), 1.33 (s, 9H, 3× Boc–CH_3), 1.20 (t, $J = 6.7$ Hz, 12H, 4× RhB–CH_3).

^{13}**C-NMR** (DMSO, 125 MHz): 198.9 (Ar–C=O), 172.1 (C(=O)–NH), 164.9 (C(=O)–O), 157.8 (Ar–H), 157.5 (Boc–C=O), 156.0, 155.6, 155.5 (Ar–C), 141.04 (Triazol–Ar–C), 134.6, 133.9, 133.8, 133.7, 131.3, 131.2, 131.0, 130.9, 129.6, 129.2 (Ar–C), 125.3 (Triazol–Ar–C), 115.0, 114.9, 114.8, 113.3, 96.3 (Ar–C), 78.4 (tert–C), 78.0 (NH(Boc)–CH), 77.8, 70.1, 70.0, 69.9, 69.6, 69.3, 68.0 (O–CH_2), 58.6 (Ar–CH_2), 53.2 (RhB–CH_2), 49.8 (Ar–CH_2), 45.8 (N–CH_2), 28.7 (Boc–CH_3), 12.9 (RhB–CH_3).

(5) **(9-2-[1-(2-2-[2-Amino-4-(2-amino-phenyl)-4-oxo-butyrylamino]-ethoxy-ethyl)-1H-[1,2,3]triazol-4-ylmethoxycarbonyl]-phenyl-6-diethylamino-xanthen-3-ylidene)-diethyl-ammonium Salt:**
Boc-deprotection of the rhodamine B–kynurenine conjugate **(4)** was performed by dissolving conjugate **(4)** in 6 ml of CH_2Cl_2 containing 25% trifluoroacetic acid. After stirring at room temperature for 1 hour, the solution was precipitated into 50 ml of ice-cold Et_2O and centrifuged at maximum speed for 5 minutes at 4 °C. The precipitate was then dissolved in deionized water and lyophilized. Purification by HPLC afforded the pure product as a pink solid (60.5 mg, 26% yield).

Spectroscopic data: ^{1}**H-NMR** (DMSO, 500 MHz): 8.20 (dd, J = 8.0, 1.4 Hz, 1H, Ar–H), 8.11 (s, 1H, C(=O)NH), 7.93–7.84 (m, 3H, Ar–H), 7.85–7.78 (m, 2H, Ar–H), 7.47 (dd, J = 7.7, 1.4 Hz, 1H, Ar–H), 7.05–6.99 (m, 3H, Ar–H), 6.97–6.89 (m, 5H, Ar–H), 5.05 (d, J = 4.4 Hz, 3H, Ar–CH_2 + CH), 4.47–4.41 (m, 2H, Ar–CH_2), 3.75 (t, J = 5.2 Hz, 2H, O–CH_2), 3.63 (q, J = 6.9 Hz, 8H, RhB–CH_2), 3.54 (d, J = 5.6 Hz, 2H, O–CH_2), 3.50–3.42 (m, 8H, O–CH_2), 2.92 (q, J = 5.6 Hz, 2H, O–CH_2), 1.20 (t, J = 7.0 Hz, 12H, RhB–CH_3).

^{13}**C-NMR** (DMSO, 125 MHz): 197.3 (Ar–C(=O)), 168.8 (C(=O)–NH), 164.9 (C(=O)–O), 158.2 (Ar–C), 157.9 (Ar–C), 157.5 (Ar–C), 155.5 (Ar–C), 141.1 (Triazol–Ar–C), 133.2 (Ar–C), 133.7 (Ar–C), 131.2 (Ar–C), 130.9 (Ar–C), 129.6 (Ar–C), 125.3 (Triazol–Ar–C), 117.5 (Ar–C), 114.9 (Ar–C), 113.3 (Ar–C), 96.3 (Ar–C), 70.1 (O–CH_2), 70.0 (O–CH_2), 69.9 (O–CH_2), 69.0 (O–CH_2), 67.1 (O–CH_2), 58.6 (Ar–CH_2), 49.8 (Ar–CH_2), 45.7 (N–CH_2), 12.87 (CH_3).

(6) **(6-Diethylamino-9-2-[1-(2-2-[2-(2-hydroxy-ethoxy)-ethoxy]-ethoxy-ethyl)-1H-[1,2,3]triazol-4-ylmethoxycarbonyl]-phenyl-xanthen-3-ylidene)-diethyl-ammonium Salt:**
Propargyl rhodamine B **(1)** (100 mg, 193.4 µmol, 1 eq) and azidotetraethylene glycol (42.4 mg, 193.4 µmol, 1 eq, synthesized according to literature [168]) were dissolved in 25 ml of a mixture of CH_2Cl_2/MeOH/H_2O (10:10:3). An aqueous solution of $CuSO_4$ (0.5 M, 15.5 µL, 7.74 µmol, 0.04 eq) was added, followed by TBTA (1 mg, 1.93 µmol, 0.01 eq) and sodium ascorbate (8.4 mg, 42.6 µmol, 0.22 eq), and the mixture was heated to 60 °C. The reaction progress was monitored by TLC. After 16 h, the mixture was cooled down and 25 ml of ddH_2O was added. The mixture was extracted three times with 50 ml CH_2Cl_2, then dried over Na_2SO_4 to yield the crude product. Purification by column chromatography (CH_2Cl_2/MeOH 3:1) afforded the pure product as a pink oil (135.8 mg, 95% yield).

Spectroscopic data: ^{1}**H-NMR** (DMSO, 500 MHz): 8.22 (d, J = 8.0 Hz, 1H, Ar–H), 7.89 (t, J = 5.2 Hz, 2H, Ar–H), 7.82 (t, J = 7.9 Hz, 1H, Ar–H), 7.48 (d, J = 7.5 Hz, 1H, Ar–H), 7.04 (dd, J = 9.5, 2.2 Hz, 2H, Ar–H), 6.96 (s, 1H, Ar–H), 6.95–6.92 (m, 3H, Ar–H), 5.06 (s, 2H, Ar–CH_2), 4.56 (s, 1H, OH), 4.45 (t, J = 5.2 Hz, 2H, O–CH_2), 3.76 (t, J = 5.2 Hz, 2H, O–CH_2), 3.65 (q, J =

6.8 Hz, 8H, CH_2), 3.49 (dd, J = 5.6, 3.1 Hz, 2H, O–CH_2), 3.46–3.41 (m, 6H, O–CH_2), 3.37–3.34 (m, 2H, O–CH_2), 1.22 (t, J = 6.8 Hz, 12H, CH_3).

^{13}**C-NMR** (DMSO, 125 MHz): 164.88 (C(=O)), 157.88 (Ar–C), 157.53 (Ar–C), 155.53 (Ar–C), 141.05 (Ar–C), 133.71 (Ar–C), 131.24 (Ar–C), 130.93 (Ar–C), 129.67 (Ar–C), 125.36 (Ar–C), 114.94 (Ar–C), 113.32 (Ar–C), 96.29 (Ar–C), 72.75 (CH_2), 70.21 (CH_2), 70.17 (CH_2), 70.05 (CH_2), 69.97 (CH_2), 69.01 (CH_2), 66.81 (CH_2), 60.63 (CH_2), 58.63 (CH_2), 49.77 (CH_2), 45.76 (CH_2), 12.89 (CH_3).

3.1.3 Magnetic bead immunoassay (MIA)

The following methods were developed and applied by the author and were previously published in [2].

Antibody biotinylation

A total of 1 µl of a 6 mg/ml Biotin-NHS solution (NHS-dPEG®12-biotin, Sigma Aldrich, Taufkirchen, Germany) was added to 100 µl of an anti-kynurenine antibody (monoclonal Mouse IgG1a κ chain anti-kynurenine antibody, clone 3D4-F2, ImmuSmol SAS, 0.5 mg/ml). The mixture was incubated for 50 min at room temperature with gentle shaking. Excess Biotin-NHS was removed using a VivaSpin 500 centrifugal concentrator with 10 kDa MWCO (Sigma Aldrich).

Bead preparation

For bead activation, 50 µl of magnetic beads (Dynabeads™ MyOne™ Streptavidin C1 magnetic beads, 10 mg/ml, Thermo Fisher Scientific, Schwerte, Germany) was diluted to 1 mg/ml with 450 µl of PBS and pelleted on a magnetic rack for 2 min. The supernatant was discarded, and the beads were washed three times with 500 µl PBS. After the last washing step, 20 µl of the supernatant was replaced with 20 µl biotinylated antibody (0.5 mg/ml). The mixture was incubated for 30 min at RT under gentle shaking. The reaction was blocked by washing the beads three times with PBS containing 1.5% BSA and 0.5% Tween-20. The final concentration was 20 µg of antibody per 1 mg of beads.

Immunoassay conjugate binding

For 3 h at RT, 0–100 µM rhodamine B–kynurenine conjugate **(5)** or rhodamine B-PEGLinker **(6)** was incubated with 50 µl of antibody-conjugated magnetic beads and 50 µl of PBS (1:3 dilution). The beads were pelleted on a magnetic rack, and the unbound rhodamine B in the supernatant was quantified in a 96-well plate with a fluorescence measurement of 100 µl of supernatant at 561 nm excitation and 592 nm emission, using a Tecan Infinite M200 multiplate reader. A standard curve of rhodamine B fluorescence intensity between 0 and 100 µM diluted 1:3 in PBS was used for the calculation of bead-bound conjugate **(5)** or **(6)**.

Competition between rhodamine B–kynurenine conjugate and native kynurenine

Fifty microliters of antibody coupled beads was incubated with 50 µl of 12 µM rhodamine B-kynurenine conjugate **(5)** and 50 µl of spiked PBS or artificial saliva (Sigma Aldrich, SAE0149), containing 0–250 µM native L-kynurenine, for 3 h at RT on a hula shaker (1:3 dilution). Beads were pelleted on a magnet and fluorescence intensity of unbound rhodamine B–kynurenine conjugate **(5)** in 100 µl supernatant was measured in a Tecan Infinite M200 multiplate reader at 561 nm excitation and 592 nm emission (see Figure 13). Bead-bound L-kynurenine was indirectly calculated by calculating the amount of displaced rhodamine B–kynurenine conjugate **(5)**. Therefore, the fluorescence intensity of bound rhodamine B–kynurenine conjugate **(5)** without L-kynurenine was subtracted from the fluorescence intensity of samples with different L-kynurenine concentrations.

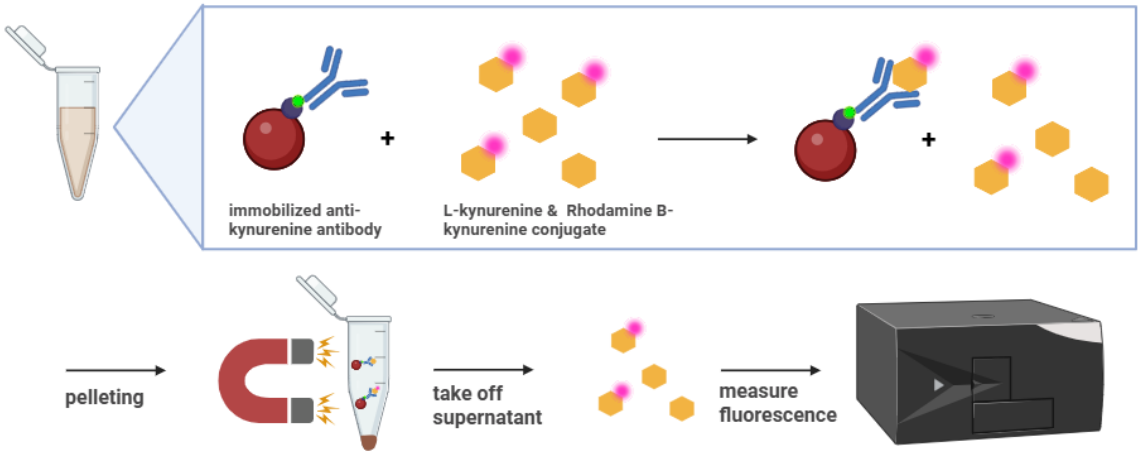

Figure 13: Schematic principle of the bead-based competitive immunoassay for L-kynurenine. A biotinylated anti-kynurenine antibody was immobilized on the surface of the magnetic beads and incubated with a constant amount of fluorescent kynurenine conjugate and different concentrations of native kynurenine. The beads were then pelleted on a magnetic rack and the fluorescence in the supernatant was measured photometrically to calculate the amount of native kynurenine. (Image Created in BioRender.com, accessed on May 2025.)

3.2 Part 2: Ethanolamine quantification using protein nanopores

In the second part of this dissertation, a ready-to-use nanopore platform for ethanolamine quantification was developed using the commercially available protein-nanopores from the MinION® sequencer of Oxford Nanopore Technologies. Therefore, a strand-displacement assay on the surface of magnetic beads using the ethanolamine binding aptamer was designed. Further, a data evaluation software was developed for easy visualization of nanopore experiment results. LC/MS was used to verify nanopore results.

3.2.1 Materials

Ethanolamine binding aptamer with and without 3′biotin (5′ ATACCAGCTTATTCAATTTGAGGCGGGTGGGTGGGTTGAATA 3′), 3′- biotinylated aptamer complement (5′ CCACCCACCC 3′/biotin), 3′-biotinylated random sequence (non-binding) (5′ CAC GGC ATG GTT CAA TAC TTA AGG GCG TCG TG 3′/biotin) and 3′-biotinylated non-binding complement 5′ CCC ACC CAA 3′/biotin) were purchased from Integrated DNA Technologies (Coralville, IA). Ethanolamine, ethanol and propylamine were purchased from Sigma-Aldrich (Darmstadt, Germany). Magnetic particles 1 µM (Dynabeads™ MyOne™ Streptavidin C1 product number: 65002) were purchased from Thermo Fischer Scientific (Sankt Leon-Roth, Germany). Flongle® flow cells (FLO-FLG114) and ONT-flush buffer (EXP-FLP004) were purchased from Oxford Nanopore Technologies (Oxford, UK).

The following methods described in Chapters 3.2.2, 3.2.3, and 3.2.4 were developed and carried out by the author. The corresponding data were previously published in [1], in which the author is listed as co–first author. The LC/MS method described in Chapter 3.2.5 was performed by a co-author of the publication. The bioinformatic analyses in Chapters 3.2.6 and 3.2.7 were conducted by the other co–first author of [1].

3.2.2 Strand displacement assay

Streptavidin-coupled Dynabeads® with 1 µm diameter, were diluted to a final concentration of 1 mg/ml in 1x washing and binding buffer (W&B-buffer: 5 mM Tris-HCl, 0.5 mM EDTA, 1 M NaCl, pH 7.5). This concentration was used throughout all experiments. Oligonucleotide coupling was performed by diluting 50 µl (10 mg/ml) magnetic beads in 450 µl W&B-buffer in a 0.5 ml Eppendorf reaction tube. After 3-fold washing with W&B 5 µl buffer were replaced by 5 µl 100 µM 3′-biotinylated aptamer complement or non-binding complement (negative control). Oligonucleotide binding took place on a HulaMixer for 90 minutes at room temperature (Thermo

Fisher Scientific). To remove unbound aptamer complement, the particles were washed again 3-times with W&B-buffer. 10 µl buffer were again replaced by 10 µl 100 µM EA aptamer solution and the hybridization was allowed to proceed for another 90 minutes on a shaker at room temperature. After hybridization, particles were pelleted on a magnetic rack and the supernatant was collected for measuring the binding efficiency. Particles with hybridized aptamer were washed again with W&B-buffer 3-time. Strand-displacement with ethanolamine took place by adding 100 µl ethanolamine solution (0.5-25 µM] in W&B-buffer to the beads. 20 µM ethanol or 20 µM propylamine were used as negative controls. After 15 minutes on a shaker at room temperature, the beads were pelleted, and the first supernatant was used for calculation of aptamer hybridization efficiency. The particles were washed again 3 times with W&B-buffer, were directly resuspended in 100 µl ONT-flush buffer and incubated for 15 minutes on a shaker at room temperature. Beads were pelleted on a magnetic rack and aptamer concentration of 30 µl supernatant was measured in the MinION® (see Figure 14).

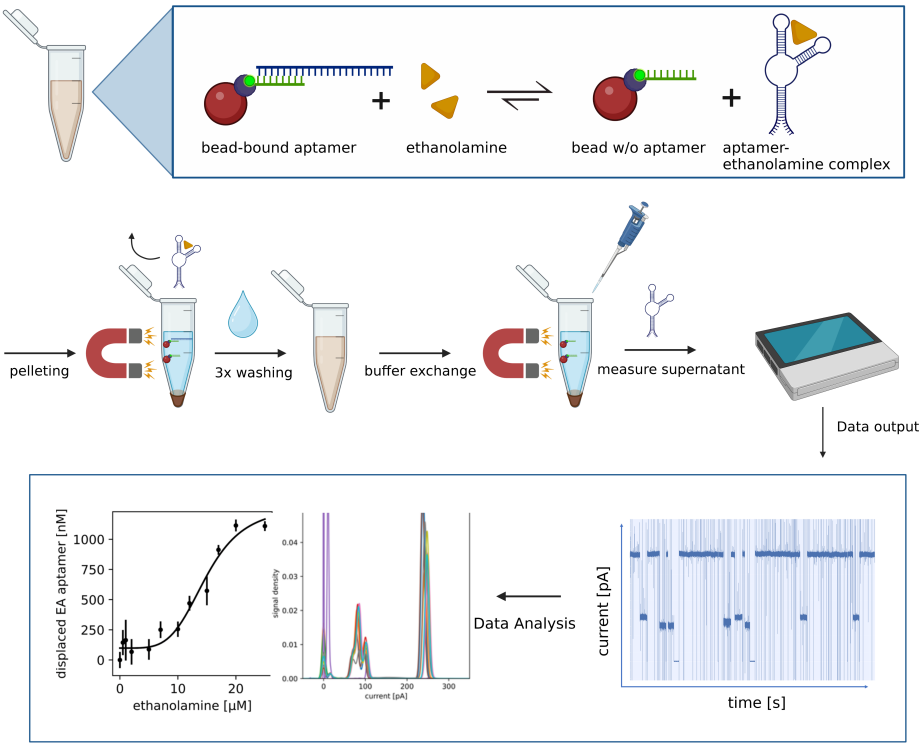

Figure 14: Schematic principle of the strand displacement assay. A new approach for small molecule detection using a ready-to-use protein nanopore platform was designed. Using ethanolamine as an example, a strand displacement assay with magnetic beads and a target-binding aptamer was developed and optimized. The nanopore signals can be analysed with the in-house developed software. Ethanolamine was successfully detected quantitatively in the micromolar range [1].

3.2.3 Quantification of oligonucleotides immobilization and hybridization efficiency

For quantification of oligonucleotide immobilization and hybridization efficiency, the absorption of 1 µl of the collected supernatant after aptamer complement immobilization and EA aptamer hybridization to its complement strand, were photometrically measured in triplicates at 260 nm using a nanophotometer (Nanophotometer® P-class, P-360, Implen GmbH). The same measurements were done with non-reacted oligonucleotides as control measurement, giving insights on the aptamer's ability to hybridize to its complementary strand and the effect of steric hindrance.

3.2.4 Aptamer quantification using MinION®-nanopores

Flongle flow cell (R 10.4.1) were adjusted to room temperature for 30 minutes before use. After reaching room temperature, the flow cell was inserted into the MinION® sequencer using the Flongle adapter. To check the number of active pores for analysis, a flow cell check on the device was performed. Flow cells were discarded if the active pore level was below warranty of 30 pores. Otherwise, the flow cell was flushed with 120 µl of ONT-flush buffer and the 30 µl aptamer sample were added in a dropwise fashion. Nanopore analysis started using the LSQK-109 sequencing kit settings without barcoding, a runtime of 30 minutes and activation of bulkfile output including the raw current data. Flow cells can be re-used several times after analysis (approximately 5-times), if washed with 120 µl ONT-flush buffer between each experiment. Using the new developed evaluation software (Nanotrace), an aptamer calibration line was developed by measuring the event-density of pure 5 nM-10 µM EA-aptamer in ONT-flush buffer. The linear range was used for aptamer quantification in the strand-displacement assay.

3.2.5 Quantification of ethanolamine via LC/MS

Magnetic beads were functionalized with 10 µl of a 100 µM solution of either a $3'$-biotinylated EA aptamer or a random, non-binding sequence, as previously described. The beads were then incubated with 100 µl of ethanolamine solution (0.5–20 µM) in W&B buffer. Following incubation, the beads were separated using a magnetic rack, and the supernatant was collected for further analysis. Ethanolamine concentrations in the supernatant, after exposure to either aptamer- or random sequence-modified beads, were quantified using a previously established method [169]. Briefly, 100 µl of the respective supernatant was mixed with 900 µl of acetonitrile and subjected to ultrasonication for 10 minutes. The samples were then centrifuged at 20,000 rcf for 20 minutes at 4 °C, resulting in phase separation into an organic (upper) and an aqueous (lower) layer. A volume of 800 µl from the upper phase was transferred into a glass vial for direct

analysis. Quantification was performed using a 4000 QTRAP mass spectrometer (ABI Sciex) coupled to a NexeraXR HPLC system (Shimadzu). LC and MRM parameters were consistent with those described in the referenced method [169]. The mass spectrometer operated in positive ion mode, using an electrospray voltage of 5500 V at 400 °C, with curtain gas set to 20 psi, collision gas at 6 psi, nebulizing gas at 40 psi, and auxiliary gas at 50 psi. All quadrupoles were set to unit resolution.

3.2.6 Determination of event density

The procedure for calculating event densities was developed through extensive data mining, using data from 52 runs with known concentrations to establish the method and generate a calibration curve. The high redundancy of the flow cell data enabled robust filtering prior to signal density calculation, which was optimized during the same process. Various pre-processing strategies were explored, including moving average filters (mean or median with varying parameters) and an outlier filter based on a Huber-type skipped mean rule, as well as different choices for the event band. These combinations were evaluated for their suitability as indicators of analyte concentration. Assuming a monotonic relationship between event density and concentration, the combination yielding the highest Spearman correlation was selected. In the first step, data from each channel were segmented into multiple signal bands corresponding to the three functional states of the nanopore (baseline, event, closed; see Figure 22a, closed state not shown). Due to inherent baseline fluctuations between channels, even within the same run, baseline levels were individually determined. Channels were classified as active or inactive based on these values: on average, 55 out of 126 channels per flow cell were active, with approximately 45 remaining after filtering. For each signal band, the number of data points was determined, indicating the proportion of the run spent in that state. The "event density" refers specifically to the proportion of data points within the event band. Channels with baseline values or baseline shares identified as outliers, defined as deviations exceeding three times the median absolute deviation from the median, based on a Huber-type rule, were excluded from further analysis. The final event density was computed as the mean event density across all non-rejected channels. Ultimately, the pre-processing steps did not enhance performance, and due to the computational burden of moving-window calculations, the finalized method operates directly on the raw data.

3.2.7 Visualizing experiments with Nanotrace

A python-based GUI-application, called nanotrace, was developed to visualize the results of the MinION®-measurements, allowing easier calculation of the associated aptamer event densities. This is an open-source application which is available for download at http://github.com/simanjo/nanotrace. It contains three main components: First, an overview page for the currently loaded experiment (see Figure 15. At **(1)**, a bulk file can be selected for analysis or display. NanoTrace maintains a database of previously loaded experiments, identified by file content hashes, accessible via the Settings tab. If an experiment is not yet registered, active channels must be calculated first (not shown). After determining the active channels, a specific channel can be selected **(2)**, and a summary is displayed **(3)**. For this summary, the file name is analysed to determine concentration information. If the name contains “buffer”, the concentration is assumed to be zero; otherwise, a case-insensitive search is performed for ‘micro’, ‘nano’ or “nm”, with all preceding numbers interpreted as micromolar or nanomolar concentrations. Second, users can view a squiggle plot for the selected channel (Figure 15 bottom left), or third a kernel density estimation (KDE) plot for the individual channel, or an overlay of the KDEs of 10 randomly selected active channels (Figure 15 bottom right). If values for the zero density, baseline density or baseline value are identified as outliers, they are highlighted in red. To provide efficient data structures Numpy [170] is used for all statistical computations, except the kernel density estimations which are performed using the statsmodel [171] package. Dealing with the output bulkfiles is done using h5py [172], a python interface to the HDF5 data format. For detailed information see supplementary information of Quint et. al (2024) [1].

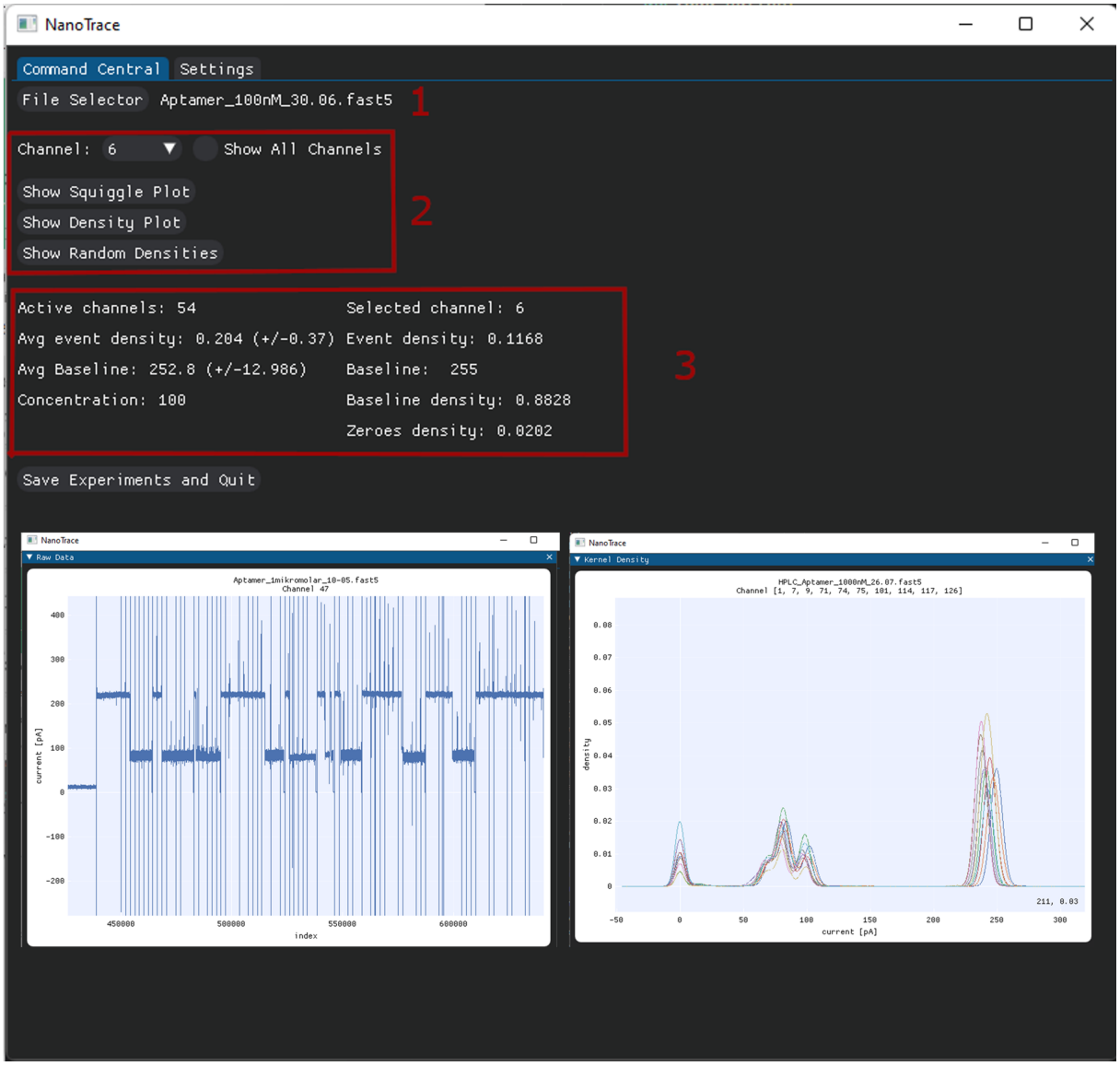

Figure 15: Main view of NanoTrace with exemplary information for the currently loaded experiment. Top: (1) selected experiment file, (2) channel selection and (3) channel output. **Bottom**: (left) squiggle plot of selected channel and (right) event density plot for 10 random selected channels.[1].

3.3 Part 3: Solid-state nanopores for small molecule detection

This third part aimed to apply insights from hybrid nanopores to solid-state nanopores (ssNPs), assessing their potential, benefits, and limitations for small molecule detection. Therefore, different fabrication methods were evaluated for their potential in small diameter nanopore (< 10 nm) fabrication. Furthermore, the fabricated nanopores were compared in terms of quality, current noise and applicability for molecule sensing, especially small molecule sensing. Surface modification techniques were investigated for improving nanopore functionality.

3.3.1 Materials

Silicon Nitride chips (SiNx membrane: 40μm $\times$ 40μm, 12$\pm$2 nm thick; frame: 5 mm $\times$ 5 mm, 200μm thick Si; noise reduction: standard) were purchased from Norcada Inc. (Edmonton, Canada). The controlled dielectric breakdown device (SparkE2), piranha cleaning jig, and the flow cells were provided by Northern Nanopore Instruments (NNI) (Ottawa, Canada). The eOne Light Amplifier and the 100 kHz nanopore reader were purchased from Elements (Rome, Italy). Ethanolamine binding aptamer (5'-ATACCAGCTTATTCAATTTGAGGCGGGTGGGTGGGTTGAATA-3') and Ochratoxin binding aptamer (5'-GAT CGGGTGTGGGTGGCGTAAAGGGAGCATCGGACA-3') were synthesized and purified by Integrated DNA Technologies (Coralville, IA).

3.3.2 Solid-state nanopore fabrication

SiN chip preparation:
Before nanopore fabrication, the SiN chips were cleaned using piranha acid (3:1). Therefore, 30 ml of sulfuric acid (H_2SO_4) was mixed with 10 ml hydrogen peroxide (H_2O_2) in a 100 ml beaker and heated to 90°C on a magnetic stirrer. The SiN chips were inserted into the chip cleaning jig (see Figure 16A) provided by NNI and carefully placed into the beaker containing the piranha acid. The chips were cleaned in piranha solution for at least 1 hour. After cleaning, the piranha acid was carefully diluted with DI-water before disposal. The SiN chips were washed with DI-water six times and remained in the water until fabrication. To ensure best performance during nanopore fabrication, the chips were mounted in the provided flow cell (see Figure 16B) as soon as possible. The chips were placed, membrane side up, on a gasket into the female half-cell (bigger half) of the flow cell using a clean pair of tweezers. A second gasket was placed on top of the chip. The full flow cell was assembled by mating the two half-cells using screws. For fabrication via dielectric breakdown, the membrane needs to be wetted in a conductive liquid. To achieve this, 40 μl of isopropanol was flushed into the central well of each side of the fluidic

cell, to remove air bubbles. Subsequently, the flow cell was flushed with 600 μl of 1 M KCl-solution pH 8 on each side of the chip, while any overflow is aspirated using a weak vacuum. Once both sides have been flushed the electrode is inserted into the central well on either side of the chip, Ag/AgCl side down.

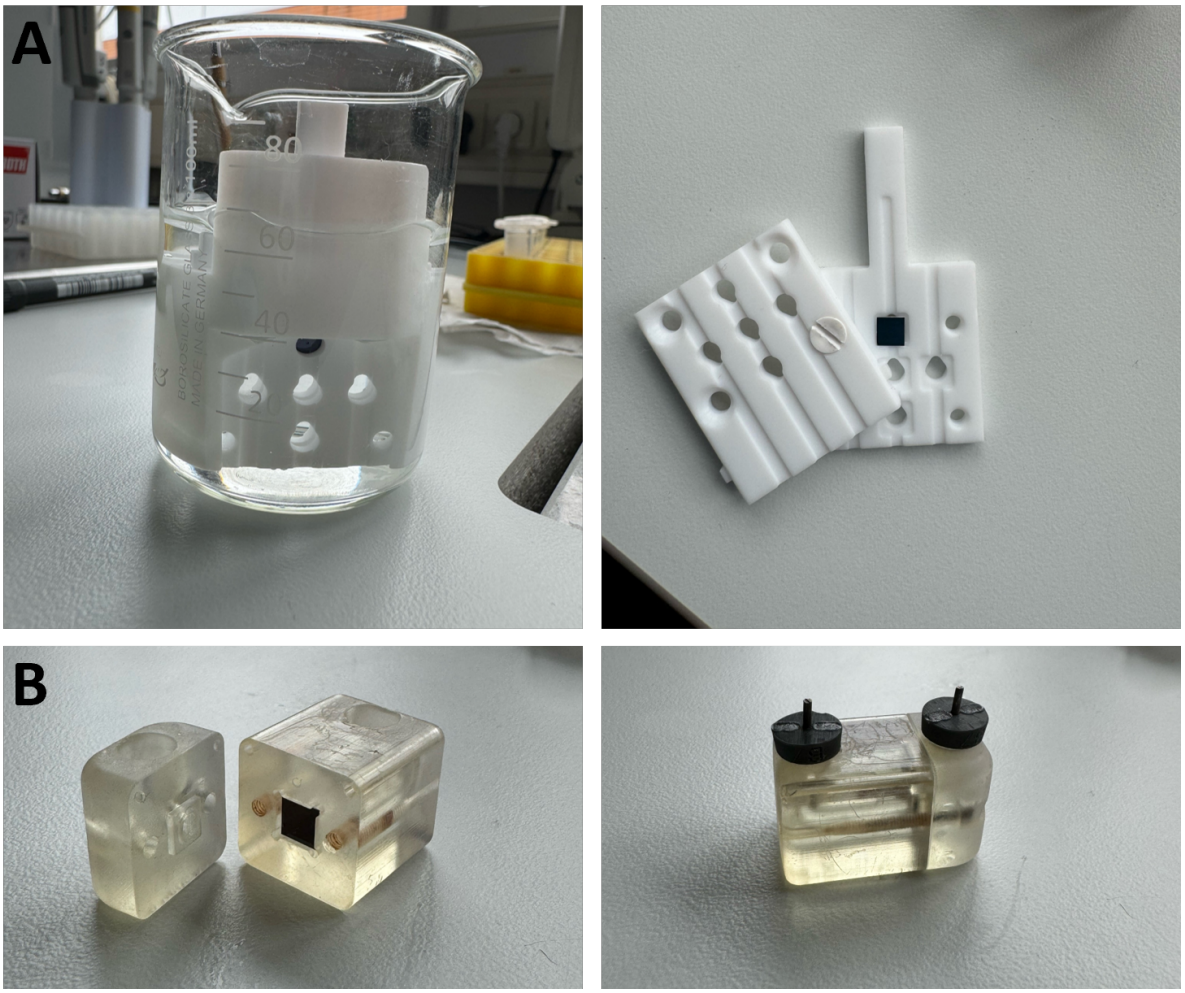

Figure 16: Nanopore chip cleaning and mounting. (A) Piranha cleaning jig from NNI for cleaning of silicon nitride chips. **(B)** NNI flow cell. The nanopore chips are mounted in the female half (bigger half) of the flow cell embedded in two gaskets and screwed with the smaller half of the flow cell. Electrodes were added to the provided holes.

Controlled dielectric breakdown (CBD):
For CBD, the SparkE2-device from NNI was used according to the manufacturer's protocol [173]. The flow cell containing the mounted chips was inserted to the device. The target pore size in nm was chosen (between 3 and 6 nm). Fabrication was done using the provided standard protocol for 5 nm fabrication within the software. At the beginning of each fabrication, a I/V-measurement was done to ensure that the membrane remained intact. During nanopore fabrication a piecewise linearly increasing voltage was applied to the membrane until the software recognized a breakdown event, meaning a spike in current. Membranes with around 10nm thickness, normally undergo CBD at a voltage of approx.10 V. After CBD the size of the fabricated nanopore was determined using I/V-measurements. For adjusting the final nanopore size, nanopore conditioning with 3.6 M LiCl pH 8 was done, to controllably enlarge the pore. Therefore, a waveform of +/- 3 V intermediate voltage was applied for several cycles until the nanopore reaches the desired target size. Conditioning also can help to reduce the signal-to-noise ratio. Final nanopore diameter is calculated using a I/V-measurements (see 3.3.3).

Focused Ion Beam Scanning Electron Microscope (FIB-SEM):
Nanopores were fabricated in SiN chips using a Crossbeam FIB-SEM system from Zeiss (Oberkochen, Germany). For this process, SiN chips were mounted on a sTEM holder with copper tape (see Figure 17). Care was taken to ensure that the chip was not fully adhered to the sTEM holder surface, as full contact could cause the chip to break upon vacuum application. The sTEM holder was then placed in the FIB-SEM vacuum chamber, where it was positioned at an angle of approximately 45°for nanopore fabrication. Nanopores with a diameter of 50 nm were created by applying a 1 pA, 30 kV ion beam for 90 ms. Following fabrication, nanopore size was verified using TEM imaging and I/V curve measurements. Before insertion into the flow cell for I/V measurements or molecular sensing experiments, the nanopores were cleaned with piranha solution to ensure surface cleanliness.

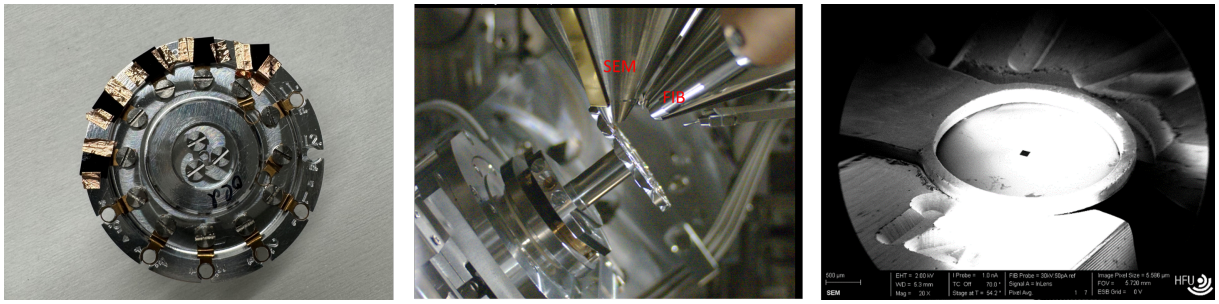

Figure 17: SiN chips on the sTEM holder inserted to the FIB-SEM. The left picture shows the fixation of the SiN-chips on the sTEM-holder using copper tape. In the middle, a picture of the sTEM-holder inserted to the FIB-SEM vacuum chamber. The right picture shows, the SEM-image of the SiN-Chip inserted into the FIB-SEM.

3.3.3 Pore diameter calculation

Pore size (diameter in nm) is calculated by drawing of an I/V-curve using the specific program in the eONE amplifier, estimating the pore diameter using following equation:

$$d = \frac{G}{2\sigma}\left(1+\sqrt{1+\frac{16\sigma t}{\pi G}}\right)$$

G = pore conductance
σ = ionic solution conductivity
t = nanopore thickness

The value of the nanopore diameter d is calculated from the pore conductance G in a solution of conductivity σ in a membrane of thickness t.

3.3.4 Surface functionalization

For surface functionalization, SiN chips were initially immersed in acetone and ethanol for 2 minutes each, rinsed with Milli-Q water, and dried under a nitrogen stream. Afterwards the chips were subjected to piranha cleaning for 1h. Silanization was carried out using a 2% (v/v) APTES (3-aminopropyltriethoxysilane) solution in toluene, with the chips incubated overnight in the APTES solution at room temperature. The next day, the chips were rinsed with toluene and Milli-Q water, each preheated to 96°C, for 2 minutes. The chips were then dried under a nitrogen stream and heated to 100°C on a thermoshaker for 1 hour; the reaction tube lid was kept open for the first 2 minutes to allow for the evaporation of residual toluene.

Successful silanization with APTES was verified using an FTIR microscope from PerkinElmer (Massachusetts, USA), to confirm the presence of functional amino groups on the surface, thus allowing further modification. For aptamer or antibody functionalization, the chips were incubated in a 2% glutaraldehyde solution in 1× PBS for 2 hours at room temperature. After rinsing with 1× PBS, the chips were transferred to a reaction tube containing either the aptamer or antibody solution. For aptamer functionalization, the chips were incubated overnight at room temperature in a 100 nM amino-modified aptamer solution in 1× PBS. For antibody functionalization, the chips were incubated for 3 hours in a 5 μg/ml antibody solution in 1× PBS. After incubation, the chips were washed with 1× PBS and dried under a nitrogen stream. Successful surface modification was confirmed using a FTIR-microscope. Additional proof of successful aptamer or antibody binding was done using fluorescently labeled antibodies or aptamers by detecting the surface fluorescence of the nanopore chips using a fluorescence reader from Scienion (Berlin, Germany).

3.3.5 Molecule sensing

Molecule sensing was performed using two different amplifiers based on pore size: (1) the **eOne Light amplifier**, suited for smaller pores (<10 nm), and (2) the **100 kHz nanopore reader**, suited for larger pores (>10 nm), both manufactured by Elements SRL (Cesena, Italy). The eOne amplifier was compatible with flow cells from NNI, whereas the 100 kHz nanopore reader required SiN chips to be transferred to a different flow cell (see Figure 18). For molecule sensing, each chip mounted in the flow cell was inserted into the appropriate device, and a baseline current (without analyte) was recorded in 1 M KCl at pH 8 as a negative control. An offset correction was applied for several seconds. Only nanopores displaying a stable, low-noise baseline current were selected for further molecule sensing experiments.

Aptamer sensing protocol

For aptamer detection, a dilution series was prepared from 100 μM stock solutions of EA-aptamer or OTA-aptamer to final concentrations of 50 nM, 100 nM, 200 nM, and 400 nM in 1 M KCl with 10 mM HEPES at pH 8. 60 μL of each concentration was introduced to one side of the NNI flow cell. A positive voltage was applied when the analyte was added to the smaller half of the flow cell, and a negative voltage when added to the larger half. Molecule sensing was conducted at a voltage of +/-400 mV, with a sampling frequency of 200 kHz, a current range of 20 nA, and no additional filtering. Between each experiment, the flow cells were flushed three times with 200 μL of fresh KCl solution on each side to remove any residual aptamer. After use, the flow cell and the gaskets were washed in isopropanol and air-dried until the next use.

Aptamer event detection

For each molecular sensing experiment, current traces were recorded for a duration of 5 minutes, provided that the nanopore remained stable throughout the measurement. Event detection was performed using the EDA software tool from Elements. For each analyte concentration, 100 seconds of low-noise measurement data were selected for analysis. Deviations from the baseline exceeding 200 pA (classified as events) were identified and counted.

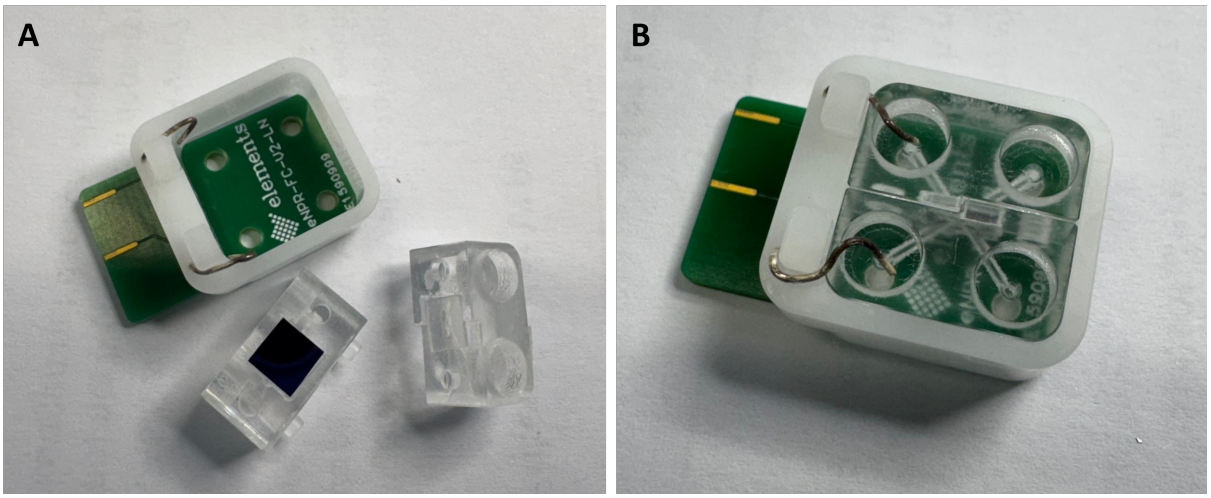

Figure 18: Flow cell for the 100 kHz nanopore reader. (A) The nanopore chip is mounted in one half of the flow cell between two gaskets. The other half is placed on top and clamped into the ring to which the electrodes are attached. **(B)** Shows the fully assembled flow cell into which the electrolyte liquid can be filled via the two chambers.

4 Results and Discussion

4.1 Part 1: A Fluorescence-Based Competitive Antibody Binding Assay for Kynurenine, a Potential Biomarker of Kidney Transplant Failure

This section presents the results of the characterization of a newly synthesized fluorescent L-kynurenine conjugate and a novel detection method for the quantification of kynurenine in PBS and saliva samples as a potential biomarker for renal transplant failure. The experimental results presented in this section have already been published in full in [2], where the author of this thesis was involved in the biological testing and development of the assay as a second author. In this thesis, however, the results are discussed in more detail and in a broader scientific context.

4.1.1 Synthesis of fluorescent kynurenine conjuagtes

The fluorescent L-kynurenine–rhodamine B conjugate was prepared following the synthetic route illustrated in Figure 18. Initially, commercially available rhodamine B was reacted with propargyl alcohol via Steglich esterification employing EDC and DMAP to yield the rhodamine B propargyl ester **(1)**. This intermediate served as the fluorescent building block for the subsequent click conjugation steps producing compounds **(5)** and **(6)**.

For the synthesis of the azido tetraethylene glycol L-kynurenine derivative **(3)**, the primary amine of kynurenine was first protected with a Boc group to yield the intermediate product **(2)**. Subsequently, an amino-azido-tetraethylene glycol linker, prepared according to a previously reported method [174], was attached, affording the azido-4EG-L-kynurenine derivative **(3)**. The click reaction between combound **(3)** and rhodamine B propargyl ester **(1)** yielded conjugate **(4)**, which upon Boc-deprotection produced the final fluorescent kynurenine probe **(5)**. To assess the influence of both the linker and the rhodamine B fluorophore on antibody binding, a rhodamine B clickamer containing only the tetraethylene glycol linker [168] was synthesized under the same conditions as **(4)**. This compound **(6)** served as a negative control in the binding assays.

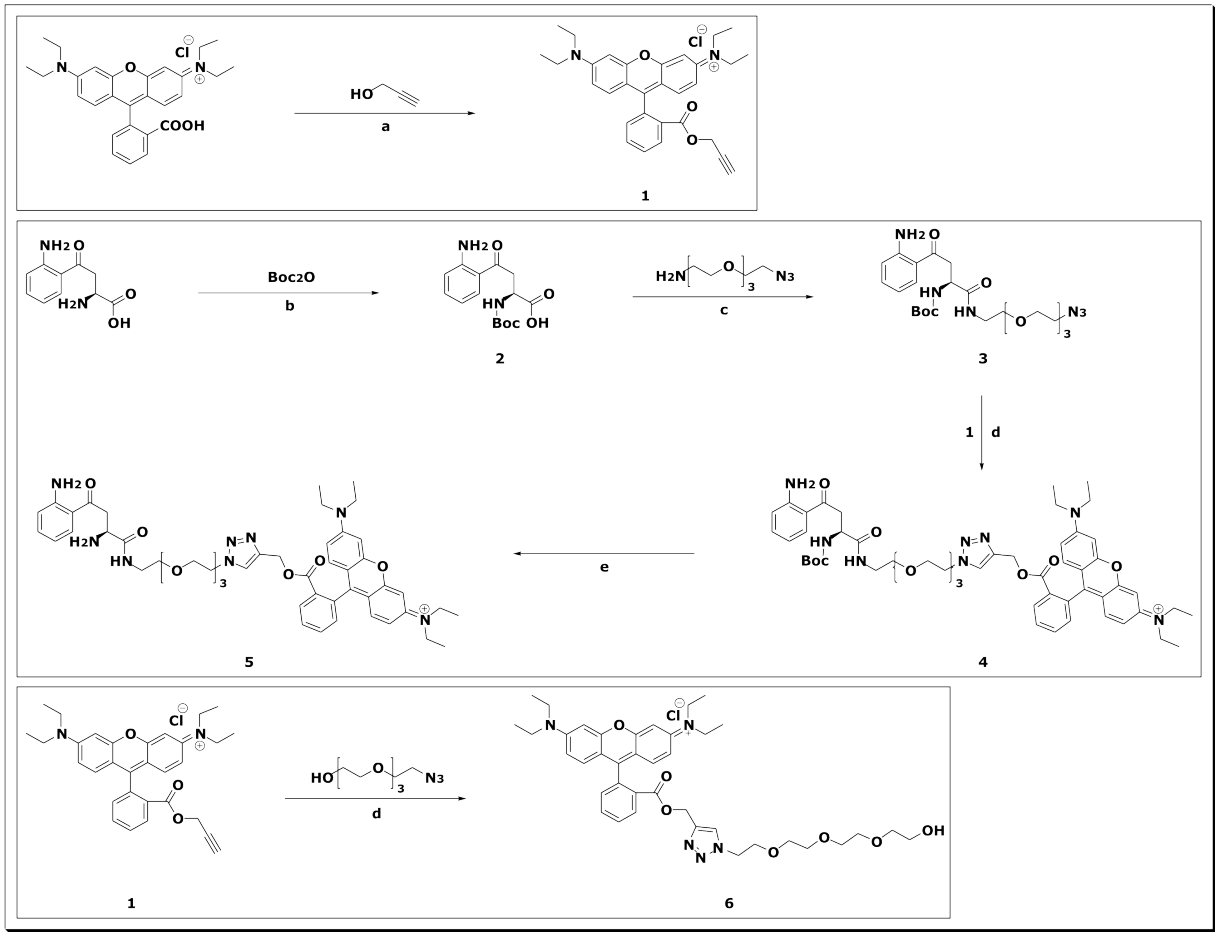

Figure 18: Synthesis route of the fluorescently labeled kynurenine probe. Rhodamine B was initially converted to the corresponding propargyl ester **(1)** via Steglich esterification. This intermediate was then reacted either with an azido tetraethylene glycol linker to produce compound **(6)** or with azido-kynurenine to yield compound **(5)**. Reaction conditions were as follows: (a) EDC, DMAP, CH_2Cl_2, room temperature, overnight; (b) NaOH, H_2O/THF (1:1), room temperature, 90 minutes; (c) EDC, DMAP, CH_2Cl_2, room temperature, 48 hours; (d) $CuSO_4$, TBTA, Na ascorbate, H_2O/MeOH/CH_2Cl_2 (10:10:3), 16 hours; (e) CH_2Cl_2/TFA (4:1), room temperature, 1 hour. Adapted from [2] under CC BY 4.0 (https://creativecommons.org/licenses/by/4.0/).

4.1.2 Spectral properties

UV/vis spectra of the rhodamine B click-conjugates were recorded in ddH_2O to determine their absorption and emission maxima (Figure 19). The absorption maximum of rhodamine B is known to be at 554 nm [175], whereas the final fluorescent kynurenine probe **(5)** and the linker control combound **(6)**, having a benzoic acid ester instead of a free benzoic acid compared to native rhodamine B, show a slight shift in their absorbtion maximum to 560 nm. Emission maxima were measured at 586 nm for the L-Kyn-4EG-RhB probe **(5)** and at 584 nm for the

4EG-RhB clickamer **(6)**, indicating suitable optical properties for following immunoassay applications.

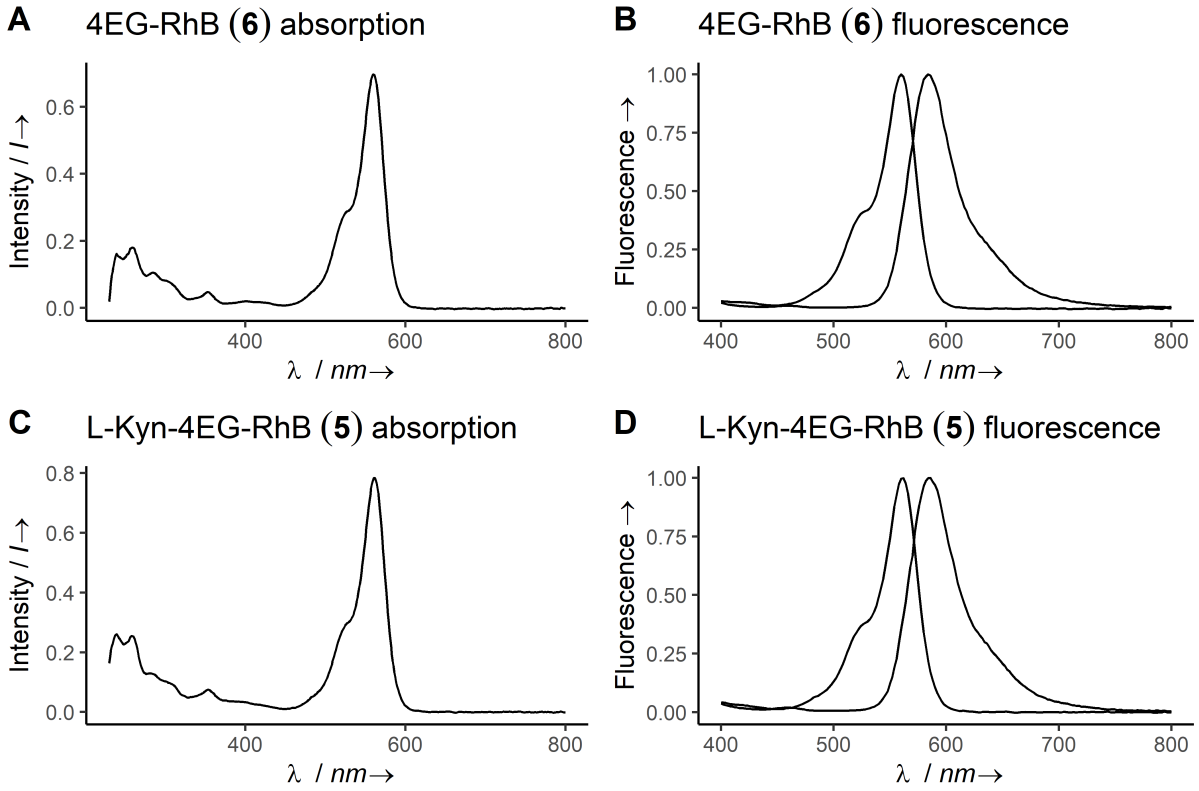

Figure 19: Absorption **(A,C)** and fluorescence **(B,D)** spectra of compounds **(5)** and **(6)** recorded in ddH_2O. Compared to native rhodamine B (absorption maximum at 554 nm [175]), both conjugates exhibit a slight redshift to 560 nm. Fluorescence emission peaks at 586 nm. Reproduced from [2] under the terms of the CC BY 4.0 license (https://creativecommons.org/licenses/by/4.0/).

4.1.3 Magnetic Bead Immunoassay (MIA)

To evaluate the antibody binding properties of the synthesized fluorescent L-kynurenine conjugate, both the direct and competitive binding of the two conjugates **(5)** and **(6)** were examined using anti-kynurenine antibodies immobilized on magnetic beads. Following incubation with the fluorescent probes, unbound conjugate was quantified by measuring fluorescence in the supernatant. Conjugate **(6)**, containing only a tetraethylene glycol-linked rhodamine B moiety, served as a negative control to assess potential nonspecific interactions with the antibody. The results of the binding assays are presented in Figure 20. The use of antibody-coated magnetic beads in suspension allows for an increased effective surface area, thereby improving assay sensitivity and facilitating favorable binding kinetics. This enhances the accuracy of competitive binding measurements between the fluorescent probe **(5)** and native L-kynurenine.

For the assay, anti-kynurenine antibodies were coupled to 1 µm magnetic beads, which were subsequently incubated with the test compounds. After magnetic separation, fluorescence was measured in the supernatant to determine their antibody binding. In the competition experiments, increasing concentrations of L-kynurenine (0–83 µM) were co-incubated with 4 µM of the fluorescent RhB-4EG-L-Kyn conjugate **(5)**. Resulting fluorescence intensities are shown in the binding and competition curves (Figure 20 and Figure 21).

With increasing concentration of the fluorescent L-kynurenine conjugate **(5)**, the measured fluorescence in the supernatant decreases since more fluorescent conjugates bind to the antibody. Figure 20A shows the difference in fluorescence intensity between L-kynurenine conjugate **(5)** and 4EG-RhB clickamer **(6)** with and without incubation with the bead-bound antibodies. In higher concentrations, the 4EG-RhB clickamer **(6)** binding affinity also increases, probably due to unspecific interactions between either the linker or the rhodamine B residue. Apart from this, the difference in measured fluorescence for the L-kynurenine conjugate **(5)** is significantly stronger, showing a KD-value of 5.9 µM, and therefore, unspecific interactions between the 4EG-RhB clickamer **(6)** and the magnetic bead-bound antibody can be neglected. As shown in Figure 21, the competitive binding assay shows a proper increase in fluorescence along with increasing concentrations of native L-kynurenine in both PBS and artificial saliva. Increasing fluorescence levels are caused by the displacement of the fluorescent conjugate through native kynurenine. The IC50 values of this competition were calculated to be 4.0 µM in PBS and 10.2 µM in saliva. As expected, the IC50 value in saliva is higher than in PBS due to interfering components such as enzymes and proteins in saliva samples.

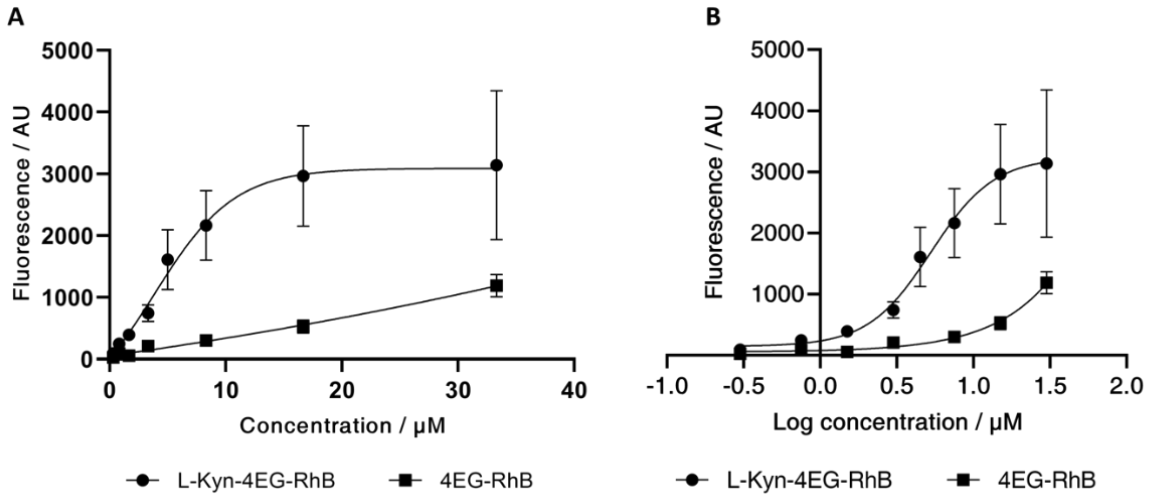

Figure 20: Magnetic bead-based antibody binding of L-Kyn-4EG-RhB conjugate (5) and 4EG-RhB control (6). (A) Binding curves plotted against analyte concentration (µM) and **(B)** logarithmic scale. The fluorescent kynurenine conjugate **(5)** exhibits markedly stronger binding to the antibody-coated beads than the control compound **(6)**, indicating specific antibody recognition. Reproduced from [2] under the terms of the CC BY 4.0 license (https://creativecommons.org/licenses/by/4.0/).

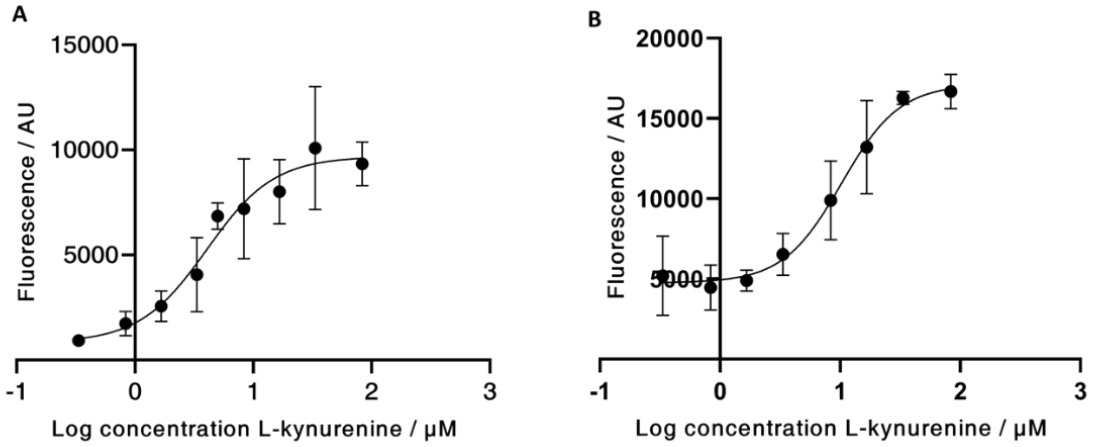

Figure 21: Competitive magnetic bead-based antibody binding assay of fluorescent conjugate (5) versus native L-kynurenine. Competition experiments in **(A)** PBS and **(B)** artificial saliva demonstrate increased fluorescence signal in the supernatant with rising concentrations of native kynurenine, confirming effective displacement of conjugate **(5)** from antibody binding sites. Adapted from [2], licensed under CC BY 4.0 (https://creativecommons.org/licenses/by/4.0/).

4.1.4 Summary of the results for L-kynurenine detection

Kynurenine is a metabolite of tryptophan degradation that is associated with various inflammatory, metabolic, oncogenic [114] and psychiatric disorders [115, 116]. While some tryptophan is metabolized to serotonin, 95% of the dietary tryptophan is metabolized to the KP via the indolamine-2,3-dioxygenases enzyme class [118]. The activity of IDO enzymes is regulated by immunological factors such as pathogenic microorganisms and LPS [121], inflammatory cytokines [124] or IL-1 and TNF-α [123]. Elevated kynurenine levels also regulate immune activation and mediate an anti-inflammatory effect, creating a feedback loop. The link between the inflammatory response and elevated serum kynurenine levels via IDO upregulation by pro-inflammatory factors makes kynurenine an interesting biomarker for clinically relevant inflammatory processes. Increased kynurenine levels have been found in chronic kidney disease (CKD) patients in the pre-dialysis phase, with levels correlating with the severity of CKD [126, 127]. In addition to CKD, elevated kynurenine levels are also associated with inflammatory processes following kidney transplantation and are inversely correlated with kidney function, as higher L-kynurenine levels have been measured in both serum and saliva of transplant rejection patients [127]. However, detecting small molecules like kynurenine is often complex and time-consuming. Most clinical approaches to quantify kynurenine from various tissues rely on LC-MS or GC-MS methods [136], which are clinically impractical and delay diagnosis. Other rapid test approaches using the kynurenine pathway for diagnosis focus on quantifying IDO activity rather than directly measuring kynurenine [139].

To date, due to the small size of the kynurenine molecule, no fluorescently labelled kynurenine derivatives bound to an anti-kynurenine antibody have been described in the literature. Likewise, there is no functional bioassay based on antibody binding of kynurenine. Here, a fluorescent, rhodamine B-labelled kynurenine derivative was successfully synthesized and its binding ability to an anti-kynurenine antibody in a bead-based immunoassay was demonstrated [2]. Spectral properties of the products were elucidated, showing only a slight shift of 6 nm in the fluorescence emission maximum when compared to native rhodamine B. The antibody binding was investigated, and the magnetic bead assay showed a good sensitivity with a KD-value of 5.9 µM for the L-kynurenine conjugate **(5)** and IC50 values of 4.0 µM in PBS and 10.2 µM in saliva for the competitive assay. Since an increase in kynurenine levels in saliva to 4.6 ± 1.6 µM under pathological conditions, compared to 0.7 ± 0.4 µM in the healthy subject, are observed [176], it thus is possible to detect metabolite changes with statistical significance by using repeated measurements. This allows for the detection of transplant rejection in a clinical setting subject to validation in clinical trials. In addition, this approach offers the possibility of using other body fluids such as blood serum, where kynurenine levels are much higher with 17.4 ± 8.4 µM for serum compared to 4.6 ± 1.6 µM for saliva [176], even though the influence of matrix proteins and other metabolites from serum would have to be investigated in more

detail for this to obtain reliable measurements. The results, demonstrate that this represents a promising approach for the development of a competitive kynurenine antibody-binding assay and ultimately a kynurenine rapid test from saliva and possibly other body fluids. A microbead competitive assay was introduced, allowing for the determination of L-kynurenine metabolites directly from saliva, thus avoiding the use of invasive procedures and expensive equipment. Furthermore, these results highlight that the application of such optimized methods in competitive immunoassays can lead to enhanced sensitivity, enabling the specific detection of small molecules in general, even when traditional antibody-based tests are not feasible.

4.2 Part 2: Ready-to-use nanopore platform for label-free small molecule quantification: Ethanolamine as first example

This section presents the results of the development of a ready-to-use protein nanopore platform for small molecule quantification, here using ethanolamine as an example using a magnetic bead-based strand displacement assay. The experimental design and execution of the strand displacement assay and nanopore measurements were performed by the author of this work. The results have already been published in [1], where the author is listed as first co-author. The data analysis was performed by the other first co-author. In this dissertation, however, the results are discussed in more detail and in a broader scientific context.

4.2.1 Identification of characteristic current patterns for aptamer detection

Initially, the nanopores' capability to detect the ethanolamine (EA) aptamer was evaluated. Therefore, varying concentrations of the EA aptamer diluted in flush buffer were analyzed using the MinION©flow cells. The ONT flush buffer was selected based on the manufacturer's recommendation for flow cell priming during sequencing. Alternative buffer systems were tested, but only the ONT flush buffer provided consistent performance, as others proved incompatible with the flow cells and led to decreased pore activity up to the total loss of active pores. As illustrated in Figure 22a, the EA aptamer led to significant current blockages, with the ionic current dropping from approximately 240 pA down to 60, 80, or 100 pA during nanopore translocation. The density plot (Figure 22b) shows a distinct wave-like signal pattern characteristic for the EA aptamer. In contrast, the negative control using the flush buffer without EA aptamer shows only minimal noise and no significant peaks (Figure 22b, right panel). The density plot quantifies the distribution of current levels throughout the experimental runtime, with three prominent peaks corresponding to key nanopore states: **(1)** base current or open pore (200–250 pA), **(2)** event current during aptamer translocation (60–100 pA), and **(3)** closed pore (0 pA). To quantify the event frequency, an event density metric was defined, which represents the proportion of time in which the signal is within the event current range. At 1 µM EA aptamer concentration, the mean event density was determined to be 0.362 ± 0.123 SD (standard deviation).

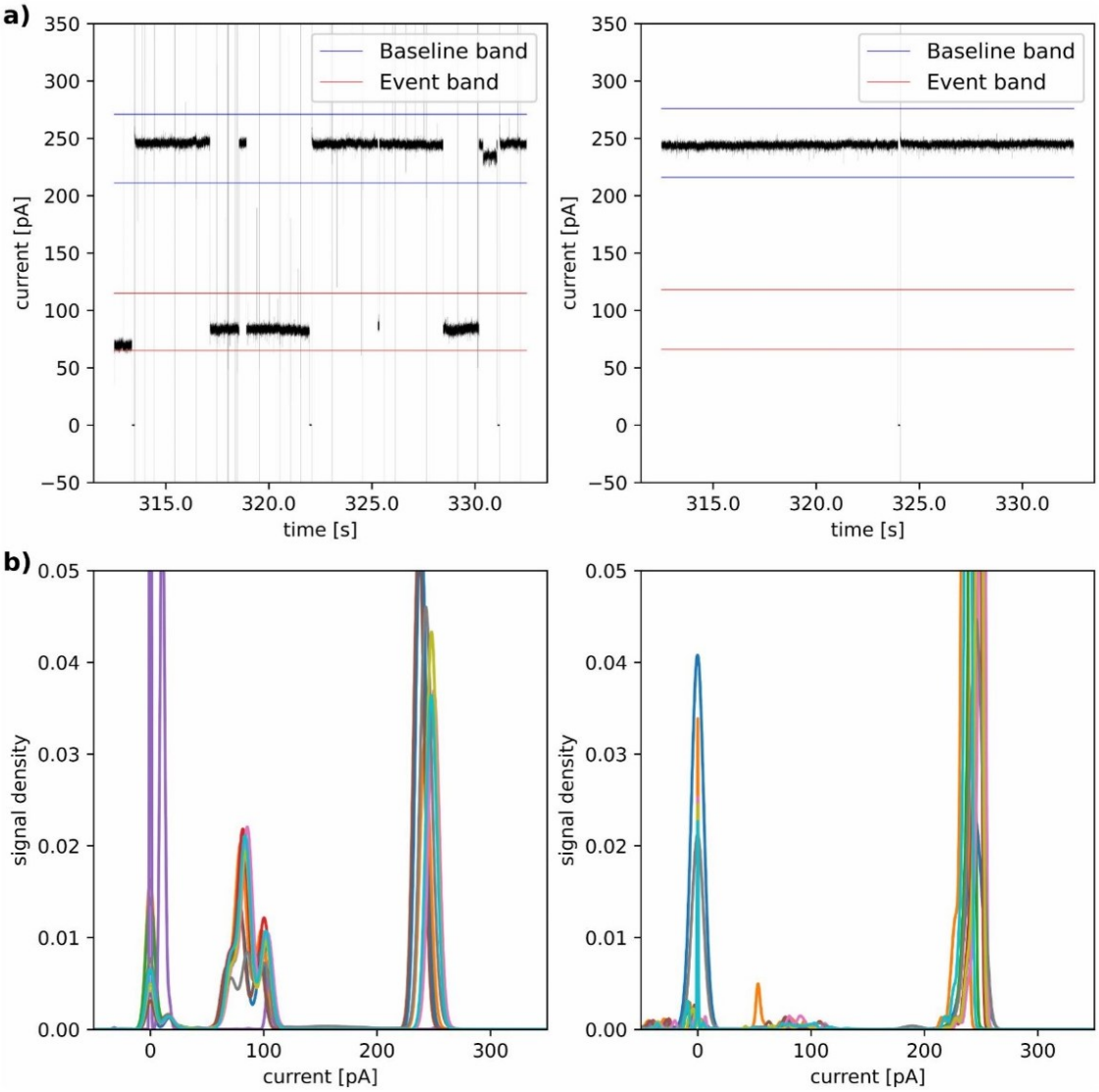

Figure 22: Ethanolamine aptamer signals. (a) Representative current traces recorded with ONT flush buffer (right) and 1 µM EA aptamer (left). **(b)** Density plots of signals from 10 randomly selected channels for ONT flush buffer (right) and 1 µM EA aptamer (left) (n=1). The density plot displays the distribution of current levels (in pA) over the entire measurement period. Reproduced from [1].

To establish a quantitative assay, it is essential that the number of detected translocation events correlates with the aptamer concentration in the sample. Consequently, the signal dependency on aptamer concentration was evaluated. As depicted in Figure 23a, event density increases proportionally with aptamer concentration up to 2.5 µM. Beyond this concentration, no further increase in event density was observed. The assay's detection limit was determined at 100 nM (event density of 0.0787 ± 0.022 SD), since concentrations below this threshold produced event densities with confidence intervals (mean ± 1 SD) overlapping those of the negative control. Thus, the aptamer exhibits a linear detection range between 100 nM and 2.5 µM. At saturation,

the translocation frequency reaches approximately 30 to 40 events per minute, during which the nanopores are blocked by the aptamer for around 70% of the time, corresponding to an event density of 0.717 ± 0.049 SD (Figure 23a). Triplicate measurements per concentration were used to perform linear regression, resulting in a calibration curve with an R^2 value of 0.92 (Figure 23b). This calibration curve provided the foundation for subsequent strand displacement assays.

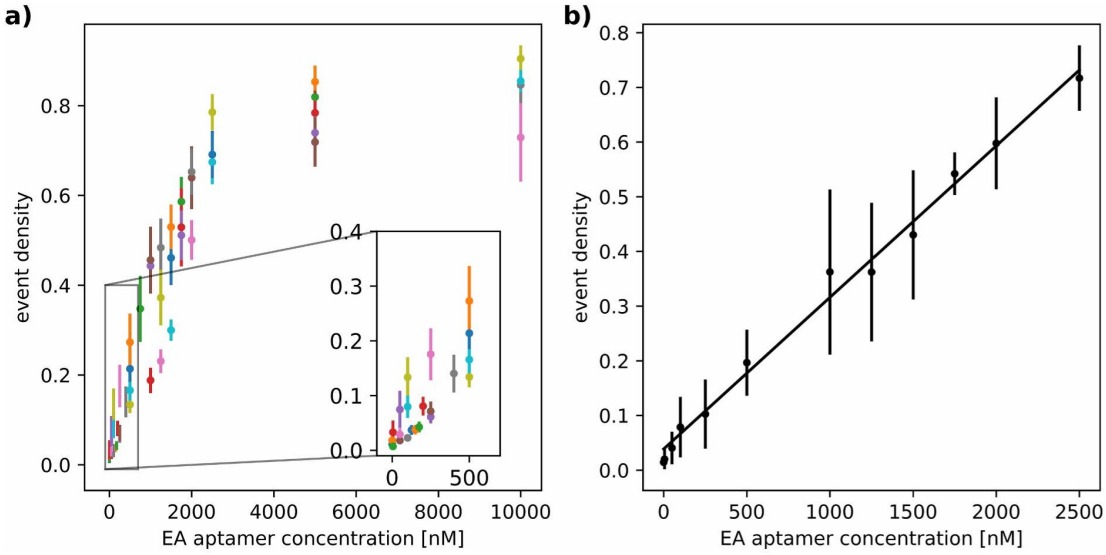

Figure 23: Ethanolamine aptamer calibration. **(a)** Mean event densities measured for varying EA aptamer concentrations ($n \leq 5$). Error bars represent intra-assay standard deviation across active channels within a single run. **(b)** Calibration curve within the linear detection range (100 nM to 2.5 µM), based on three independent runs ($n = 3$), with an R^2 value of 0.92. Error bars indicate inter-assay standard deviation. Reproduced from [1].

As ethanolamine istself is a small, uncharged molecule, it cannot be detected directly by the nanopore device. To enable detection, an aptamer-based indirect assay system was developed. As mentioned earlier, the nanopore flow cells are only compatible with ONT flush buffer. However, this buffer lacks the appropriate salt concentration and pH required for efficient hybridization of the aptamer to its complementary strand [177]. Hybridization tests performed in flush buffer showed minimal to no binding between the EA aptamer and its complementary strand immobilized to the bead surface. Moreover, when hybridization was initially performed in the manufacturer-recommended washing and binding buffer (W&B), almost complete dissociation of the aptamer from its complementary strand was observed after switching to flush buffer. This was evidenced by the displacement of over 1 µM aptamer upon incubation with flush buffer alone, with no further increase upon ethanolamine addition (data not shown). Therefore, a classic strand-displacement assay, based on directly measuring the displaced aptamer, was not feasible under these conditions.

To overcome this limitation, a modified strand-displacement assay was developed (see Figure 24). Instead of quantifying the displaced aptamer, the assay is based on measuring the amount of aptamer that remains bound to the bead-immobilized complementary strand after ethanolamine incubation (non-displaced aptamer). The ethanolamine-induced displacement is then calculated by subtracting the remaining bead-bound aptamer from the control without ethanolamine, which reflects the maximum amount of bound aptamer.

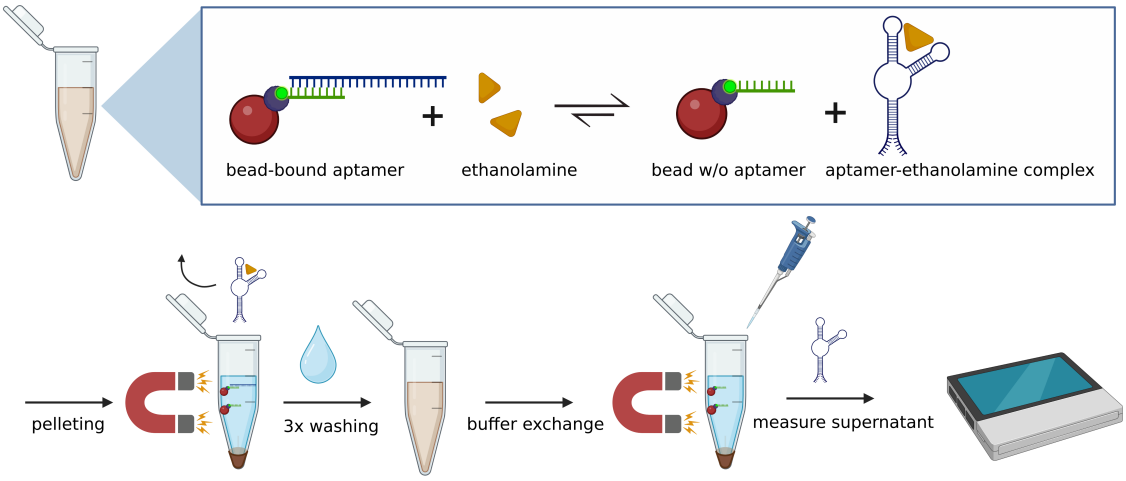

Figure 24: Principle of the strand-displacement assay. The biotinylated complementary strand of the EA aptamer is covalently bound to streptavidin-coated magnetic beads, and the EA aptamer is hybridized to its complement. Upon addition of ethanolamine, the aptamer is displaced from the complementary strand due to target binding. The beads are magnetically separated, and the supernatant containing the displaced aptamer is removed. After washing, the remaining bead-bound aptamer is eluted using ONT flush buffer and quantified using the MinION® device. Illustration created with BioRender. [1]

Both aptamer hybridization and ethanolamine displacement were performed in W&B buffer to ensure optimal binding conditions. Binding efficiency was determined by measuring the absorbance at 260 nm before (0.051) and after (0.037) the reaction. The best hybridization efficiency was obtained at a 2:1 molar ratio of aptamer to complementary strand, resulting in an average of 273 pmol aptamer bound per 500 µl of beads (1 mg/ml). This is in agreement with the manufacturer's specifications, which state that 0.5 mg of beads can bind up to 250 pmol of biotinylated DNA oligonucleotides. Thus, an aptamer binding efficiency of approximately 100% was achieved (see Table 4.1). To exclude non-specific binding of the aptamer to the bead surface, a non-binding control strand was immobilized on the beads. No aptamer hybridization was detected in this control setup, as confirmed by 260 nm absorbance measurements (data not shown).

Table 4.1: EA aptamer binding efficiency based on A260 measurements.

A260 EA aptamer	A260 supernatant	Aptamer binding (pmol)	Binding efficiency (%)
0.045	0.032	289	116
0.048	0.034	292	117
0.049	0.035	286	114
0.048	0.032	333	133
0.058	0.036	379	152
0.050	0.043	140	56
0.057	0.040	298	119
0.059	0.043	271	108
0.047	0.039	170	68

The results of the strand-displacement assay at various ethanolamine concentrations are shown in Figure 25. Increasing ethanolamine concentrations resulted in a significant decrease in the amount of aptamer remaining bound to the beads, indicating effective displacement through formation of the aptamer–ethanolamine complex (Figure 25a). Saturation of aptamer displacement was observed at 20 µM ethanolamine, beyond which no further release of aptamer was detected. At this point, the maximum displaced aptamer concentration reached 1 µM (Figure 25c). At concentrations above 5 µM ethanolamine, a clear reduction in bead-bound aptamer was observed. In contrast, at concentrations below 5 µM, the measured values (0,3543 ± 0,0290 SD) overlapped with the negative control within the confidence interval (mean ± 1 SD), limiting quantification at lower target concentrations. The residual aptamer concentration on the beads was determined using the calibration curve established in Figure 23b by applying the corresponding event density values to the linear regression equation (Figure 25b). The amount of displaced aptamer was calculated by subtracting the measured amount of bead-bound aptamer after ethanolamine incubation from the average amount bound in the absence of ethanolamine (Figure 25c). Based on these data, a dissociation constant (KD) of 14.4 µM was determined.

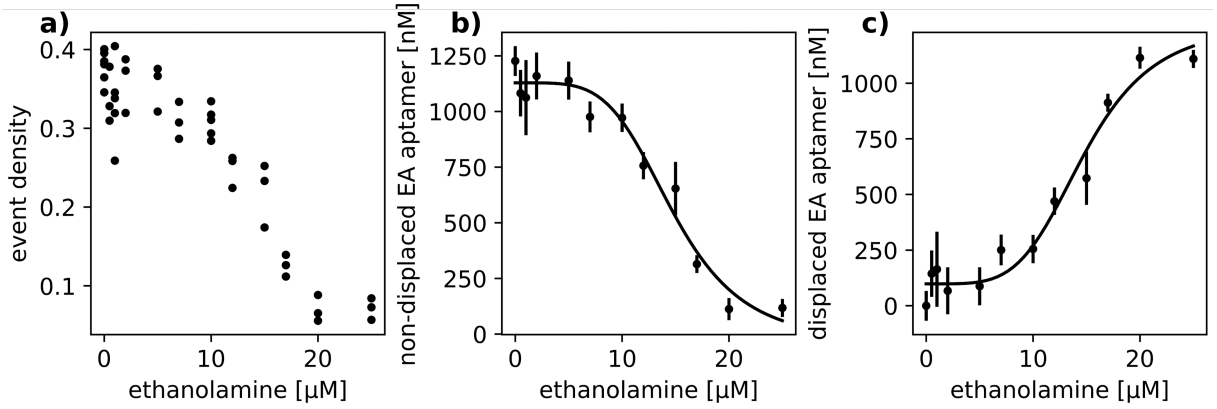

Figure 25: Aptamer displacement by ethanolamine. (a) Mean event densities of bead-bound (non-displaced) aptamers at increasing ethanolamine concentrations. Values were obtained from three independent experiments (inter-assay replicates, $n = 3$) using Nanotrace. Each replicate is shown separately. **(b)** Conversion of event densities into remaining aptamer concentrations (µM) using the calibration curve (see Figure 23b). Mean values ± SD from all replicates are shown. Nonlinear regression was applied to the resulting data. **(c)** Displaced aptamer concentrations (µM) calculated by subtracting the remaining bead-bound aptamer from the initial amount (control without ethanolamine). Data represent mean ± SD ($n = 3$), fitted by nonlinear regression. Reproduced from [1].

To demonstrate the specificity of aptamer displacement induced by ethanolamine, two structurally similar small molecules, ethanol and propylamine, were evaluated as negative controls at a concentration of 20 µM. In contrast to ethanolamine, neither compound caused significant aptamer release from the complementary strand. Additionally, the binding affinity of ethanolamine to its aptamer was confirmed by liquid chromatography–mass spectrometry (LC–MS) analysis. Ethanolamine concentrations were measured before and after incubation with either the EA aptamer or a scrambled, non-binding DNA sequence (see Figure 26). As shown in Figure 26a, only ethanolamine induced notable aptamer displacement from the beads, while ethanol and propylamine caused only a minimal release. This supports the specificity of the aptamer–ethanolamine interaction. The LC–MS results in Figure 26b show the dose–response binding curve of ethanolamine to the immobilized EA aptamer. A maximum of 1.7 µM ± 0.14 ethanolamine was bound at an input concentration of 5 µM, indicating a 3-fold excess. Higher input concentrations did not lead to further increases in binding, suggesting saturation. No detectable ethanolamine binding was observed with the scrambled aptamer sequence, confirming the specificity of the interaction. Based on these data, the dissociation constant (K_D) of 4.7 µM was calculated.

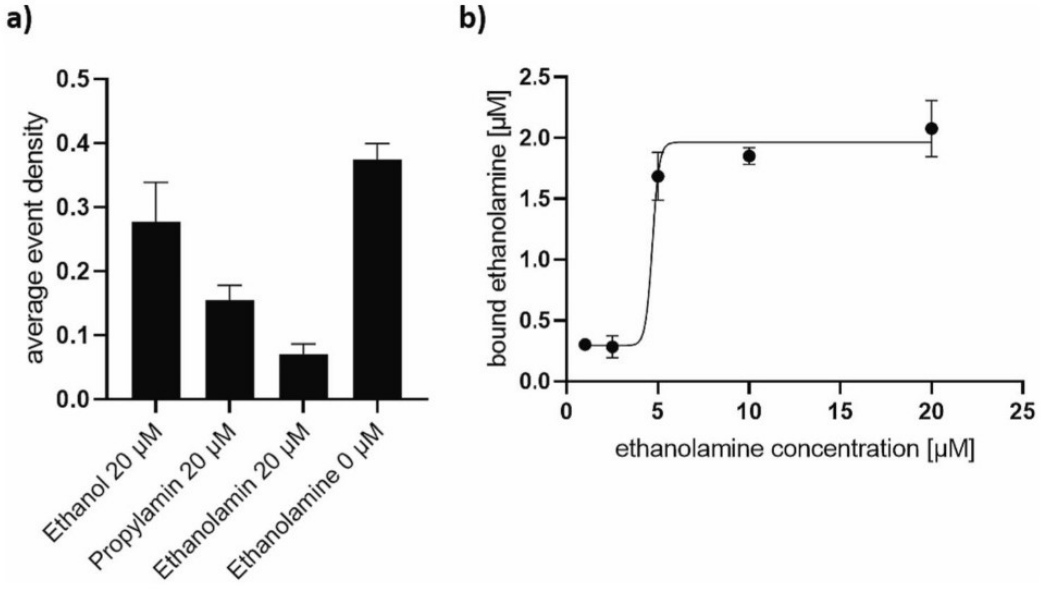

Figure 26: Aptamer affinity measurements. **(a)** Mean event densities of non-displaced EA aptamer after incubation with different small molecules (ethanolamine, ethanol, propylamine) at 20 μM. Error bars represent inter-assay standard deviation across independent runs ($n \leq 5$). **(b)** Binding curve of ethanolamine to its specific aptamer obtained by LC–MS analysis. Ethanolamine concentrations were measured after incubation with either the EA aptamer or a scrambled non-binding sequence. Data points represent mean values ± SD from three replicates. A dissociation constant (K_D) of 4.7 μM was calculated. Reproduced from [1].

4.2.2 Data analysis

For data pre-processing, analysis, and visualization, a user-friendly, Python-based software tool named *Nanotrace* was developed. The software provides squiggle plots of selected nanopore channels and calculates the corresponding event density. Event boundaries can be freely defined by the user, enabling flexible application to various experimental contexts. Additionally, the software supports graphical overlays of signal distributions from up to ten selected channels, allowing for comparative visual analysis.

4.2.3 Summary of results for ethanolamine qunatification using protein nanopores

The detection of small molecules is crucial in fields such as molecular diagnostics, drug development and disease monitoring. However, their small size presents a significant challenge for specific antibody binding, as only a single epitope is available for recognition [4]. Current state-of-the-art techniques, such as HPLC, LC/MS, and GC/MS, are effective but costly and require skilled personnel [10–12, 15]. Nanopores have emerged as promising tools for molecule sensing, frequently used for RNA/DNA sequencing and small molecule analysis [46, 47, 58, 59]. In this study [1], a novel approach that utilizes an established nanopore-based sequencer to detect ethanolamine, as model compound, through its binding aptamer in a strand displacement assay is presented.

First, the suitability of the protein nanopore system for quantitative detection of the EA aptamer was tested. As shown in Figure 22, the EA aptamer caused a significant current drop from 240 pA to 60, 80 or 100 pA during molecular translocation compared to buffer alone. In addition, the density plot showed a typical wavy pattern for the EA aptamer (Figure 22,b), which indicates that these current disruptions are caused by the aptamer translocating through the pore. The EA aptamer consists of 42 nucleotides and forms a quadruplex tertiary structure [161]. This structure is bulkier and therefore likely causes stronger interactions with the pore wall, resulting in longer translocation times compared to linear DNA strands of the same nucleotide length [178]. This might explain the relatively long translocation time of up to 1-2 seconds. According to literature, ssDNA or RNA strands with fewer than 100 nucleotides translocate too quickly (5 to 10 µs per base) to be detected by the device at a sampling rate of 3 kHz. Therefore, most other approaches for detecting small nucleic acids like microRNAs rely on bioinformatic analysis or chemical modifications to improve the signal [179–181]. In contrast, in sequencing applications, motor proteins are ligated to DNA or RNA strands to actively slow down translocation [182]. The wavy pattern in the density plot is due to three different current interruptions at 60, 80 or 100 pA during aptamer translocation. This suggests that the aptamer might adopt different conformations or block the pore differently depending on which part of the molecule enters the pore first [183–186]. The saturation effect observed at concentrations of 2.5 µM and higher can be explained by the limited number of available pores. If most pores are permanently occupied by aptamers, no further increase in translocation events per time unit can be detected. The relatively large variation between individual runs, and therefore the high standard deviations, are most likely due to the inherent variability of MinION® flow cells and cannot be improved by optimizing the method alone (see Figure 23a). Nevertheless, the results clearly show that the EA aptamer can be quantified using MinION® nanopores by analyzing the current disruptions in the respective event band, without the need for labeling. This has not been achieved with this platform before [179, 180]. Based on these findings, a strand displacement assay was developed

(Figure 24), in which the aptamer displaced by ethanolamine was indirectly detected by measuring the remaining bead-bound aptamer using protein nanopores. Using custom-developed software, ethanolamine concentrations in the micromolar range could be quantified. The results of this strand displacement assay show that the method is suitable for indirect detection of ethanolamine in a concentration range between 5 and 20 µM, with a dissociation constant (KD-value) of 14.4 µM (see Figure 25). The relatively high KD-value of the strand displacement assay is caused by the immobilization of the EA aptamer on its complementary strand before ethanolamine is added. This creates a competition between the aptamer's binding to the complementary strand and to ethanolamine, which shifts the equilibrium and increases the KD-value. In comparison, when using LC/MS for the direct detection of free EA aptamer, a lower KD of 4.7 µM was determined (see Figure 26b). Although other detection methods have shown lower limits of detection for ethanolamine,[155, 161, 166] the concentration range covered by this assay is sufficient for many clinical applications. Ethanolamine is important for the synthesis of phosphatidylethanolamine (PE), a major phospholipid in all cell membranes [143]. Reduced levels of ethanolamine or PE are linked to several diseases, including Alzheimer's disease, [146], Parkinson's disease [141], and Huntington's disease [147]. In Alzheimer's disease patients, both serum levels of PE and free ethanolamine were significantly lower across all stages of dementia, and levels correlated with disease severity. Similar observations have been made in patients with Parkinson's and Huntington's disease [145–147]. Other studies reported that ethanolamine levels below 12.1 µM in cerebrospinal fluid were associated with major depressive disorder (MDD), and could serve as a biomarker for a specific subtype of MDD [187]. In the gut, ethanolamine plays a role in bacterial competition, as certain pathogenic bacteria such as EHEC can use ethanolamine as a carbon and nitrogen source. Even small concentrations of 1 µM are enough to trigger virulence gene expression in these pathogens [188]. A separate metabolomic study using mass spectrometry showed that ethanolamine concentrations in the saliva of pancreatic cancer patients were significantly increased compared to healthy individuals [189]. Increased PE concentrations have also been found in pancreatic and breast cancer cells [190]. These findings suggest that micromolar sensitivity is sufficient to monitor changes in ethanolamine levels under pathological conditions and could also help to study its role in different diseases. At the same time, this method avoids the need for expensive and complex equipment.

In summary, the results show that the protein nanopore system from Oxford Nanopore Technologies (ONT) is not only suitable for DNA and RNA sequencing, but can also be used for the detection and quantification of small molecules. This is still a major technical challenge and usually requires expensive instrumentation, but it is highly relevant for disease diagnosis. The method is based on the current-independent and controlled translocation of target-binding aptamers. The work presented here is a proof of principle for detecting a small molecule like ethanolamine by using a strand displacement assay and its specific aptamer. These results

show that ethanolamine can be indirectly detected by measuring the remaining aptamer with the nanopore system, with sensitivity in the micromolar range. These findings also show that the ONT nanopore system can be extended beyond sequencing and used for small molecule sensing. This marks a valuable addition to its application range. The current-independent translocation of aptamers, as demonstrated here, is an important factor for detecting small molecules with sufficient signal quality. This makes the method interesting for future clinical applications, especially since the platform is already commercially available and cost-effective. The approach can also be applied to other small molecules, as long as a suitable aptamer of similar structure and size is available. The long translocation time of 1 to 2 seconds is likely related to the tertiary structure of the EA aptamer. Since many aptamers form similar structures, this method could also work for other targets. Aptamers are highly specific and are often the only available binders for small molecules that lack suitable antibodies. This makes the method flexible and promising for a broader range of analytes. Of course, this assumption still needs to be confirmed in future studies. In addition, the developed software tool Nanotrace allows researchers without bioinformatics background to quickly and easily visualize bulk fast5 files. This is a clear advantage over existing tools that are mostly based on Python and require programming skills [191, 192]. The method presented here therefore serves not only as a proof of principle but also as a practical step towards simplifying diagnostics for small molecules. It can be adapted to other targets with similar aptamers and thus represents a useful extension of existing nanopore-based methods.

4.3 Part 3: Solid-state nanopores for small molecule detection

As this section explores the application of hybrid nanopore insights to solid-state nanopores (ssNPs) for small molecule detection. Two fabrication methods were evaluated for producing sub-10 nm nanopores. The resulting nanopores were compared in quality, current noise, and sensing applicability. Additionally, surface modification techniques were examined to enhance functionality.

4.3.1 Nanopore fabrication

For nanopore fabrication two different approaches were used, the controlled dielectric breakdown (CBD) and the focused ion beam scanning electron microscope (FIB-SEM). For detecting small molecules (< 1 kDa), small diameter nanopores are needed. As seen in the previous section, the hybrid nanopores of the commercial MinION®-sequencer, with a diameter of 1.2 nm, were able to detect ethanolamine, a small biomarker, through its binding to a 42-nt long ssDNA aptamer. Therefore, the goal was to produce functional nanopores with diameters as small as possible and to test the influence of pore sizes on signal intensity.

4.3.1.1 Fabrication method 1: Controlled Dielectric Breakdown (CBD)

Nanopore fabrication in solid membranes was first conducted using CBD. This method relies on applying a voltage across an insulating membrane to generate a high electric field, while monitoring the induced leakage current. CBD promises the fabrication of very small-diameter nanopores down to 2 nm [70]. Thin silicon nitride membranes (12 nm thick) were used to fabricate small-diameter nanopores. As shown in Figure 27, CBD allows for the fabrication of nanopores with diameters as small as 3 nm. For 12 nm SiN membranes, pore formation generally occurs within the first 10 minutes under an applied voltage of approximately -10 V.

Figure 27A displays the applied voltage and the measured current over time, highlighting two breakdown events. In the left graph, a breakdown event at -6 V produces a sharp current drop to -122 nA, signaling successful nanopore formation. The right graph shows a breakdown at -7 V, with a smaller current drop to -35 nA. With a current drop threshold set to 25 nA, both events are considered successful pore fabrication. Figure 27B presents the I/V curves of nanopores before and after fabrication and following conditioning. The slope of the I/V curve increases with pore enlargement, indicating a correlation between the curve gradient and pore size. Following fabrication, pore sizes of 2.7 nm (left graph) and 1.4 nm (right graph) were achieved, subsequently enlarging to 5.7 nm and 3.0 nm, respectively, after conditioning.

However, achieving reproducibility with small-diameter nanopores remains challenging due to the random nature of the breakdown event [193]. Small variations in material properties (e.g., batch-to-batch differences) can significantly impact the resulting pore size. Using the same fabrication protocol, initial pore sizes ranged from 1.5 to 10 nm. This initial pore size is crucial, as the pore typically enlarges further during conditioning. Conditioning is strongly recommended to improve nanopore sensing performance (e.g., signal-to-noise ratio), as the surface inside the nanopore is smoothed and ideally shaped into a cylindrical channel. Consequently, achieving a final pore diameter of 3 nm has proven difficult, with a success rate of only 1 in 20 attempts.

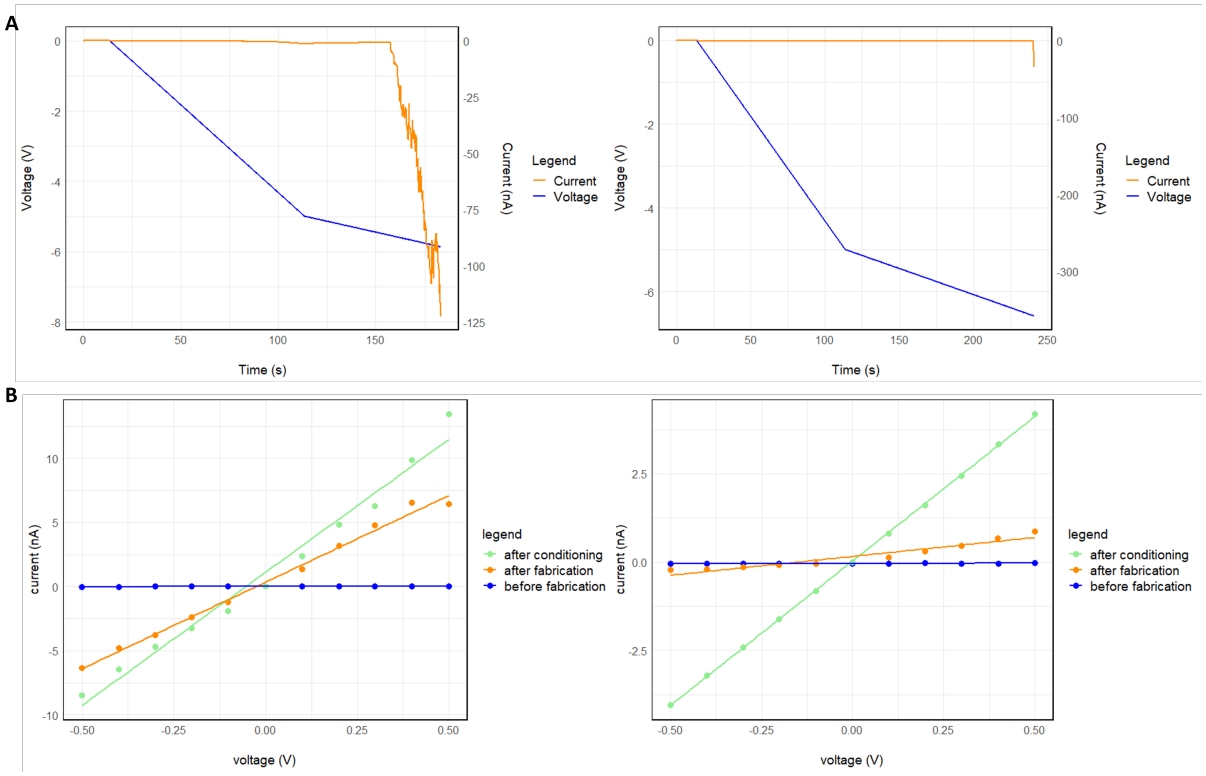

Figure 27: Nanopore fabrication using CBD. (A) Fabrication graph, showing the applied voltage and the current flow over time. **(B)** I/V-graph of the fabricated nanopores before and after fabrication and conditioning (left 5.7 nm and right 3.0 nm).

.

Nanopores with diameters below 6 nm were utilized for current recordings conducted in 1 M KCl and 10 mM HEPES at pH 8 using the eOne amplifier. For effective molecule sensing, nanopores must maintain a stable baseline current with minimal noise to achieve a high signal-to-noise ratio. However, nanopores fabricated via CDB often exhibited high noise levels and unstable baseline currents (Figure 28A), characterized by significant standard deviations, which hindered molecule sensing due to signal interference from noise. As shown in Figure 28B, nanopores were frequently stable at the start of sensing experiments but tended to irreversibly lose functionality over time. For instance, the 5 nm nanopore shown here initially detected signals for 400 nM EA-aptamer but ceased displaying translocation events after 3 minutes, accompanied by changes in the current trace. This degradation in performance could result from pore clogging [91], unstable nanopore wetting [194], or irregular, non-cylindrical nanopore geometries [195], all contributing to unstable and noisy current traces. However, a subset of nanopores in this study exhibited sufficiently low noise and stability, making them suitable for molecule detection. Further optimization of nanopore fabrication and experimental conditions could enhance their reliability and performance for sensing applications.

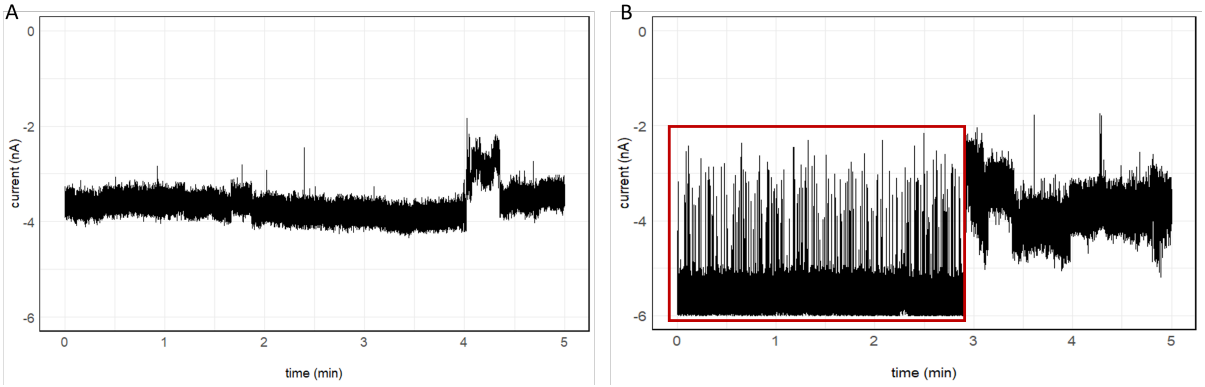

Figure 28: Current noise of 5 nm nanopore. (A) shows the noisy baseline current of a 5 nm diameter nanopore with 1 M KCl pH 8 without any target molecule. **(B)** shows the current trace for a 5 nm nanopore with 400 nM EA-aptamer in 1 M KCl pH 8. In the beginning the current trace was stable and showed molecule translocation peaks (red box), but after 3 minutes the current got instable and noisy, with no further molecule translocation events visible.

.

4.3.1.2 Aptamer detection with ssNPs fabricated using CBD

To replicate and extend the results of protein nanopores (see **??**), the ssNPs were tested for their ability to 1. detect and 2. quantify the EA-aptamer, which is the basic requirement for ethanolamine detection, as an example of a small molecule biomarker Figure 29 shows typical current drops as the EA-aptamer translocates through a 3 nm CDB-fabricated nanopore. In Figure 29A, the baseline current of the 3 nm nanopore in 1 M KCl at pH 8 is shown without EA-aptamer (negative control), displaying a stable baseline current of -3 nA with low standard deviation (+/- 500 pA) and no significant baseline fluctuations. Figure 29B-G show increasing EA-aptamer concentrations, ranging from 5 nM (B) to 400 nM (G). The number of current drops increases linearly with EA-aptamer concentration, as shown in Figure 29H. The minimum detectable aptamer concentration is 50 nM, as lower concentrations did not cause significant changes in current compared to the control (see Figure 29B and C).

These results indicate that small ssNPs with diameters around 3 nm are capable of detecting ssDNA aptamers like the EA-aptamer without further surface modification. The EA-aptamer forms a bulky quadruplex tertiary structure [165], which leads to prolonged translocation times compared to linear ssDNA aptamers. Consequently, linear ssDNA aptamers, such as the histamine-aptamer, did not produce detectable signals using the same 3 nm nanopore (data not shown).

To confirm the hypothesis that only quadruplex structures lead to visible signals, another quadruplex-forming aptamer was tested. Ochratoxin A (OTA) is a small mycotoxin produced by molds, commonly found in various foods, such as cereals, canned meats, vegetables, fruits, and cheese. The binding aptamer for OTA is a 36-nt long ssDNA aptamer, which shares a similar length and structure with the EA-aptamer. As shown in Figure 20, the OTA-aptamer also produced significant current signals in a concentration-dependent manner, with the signal count increasing as the OTA-aptamer concentration rose (Figure 30B-F). These results demonstrate that other quadruplex-forming aptamers can also be detected using 3 nm ssNPs.

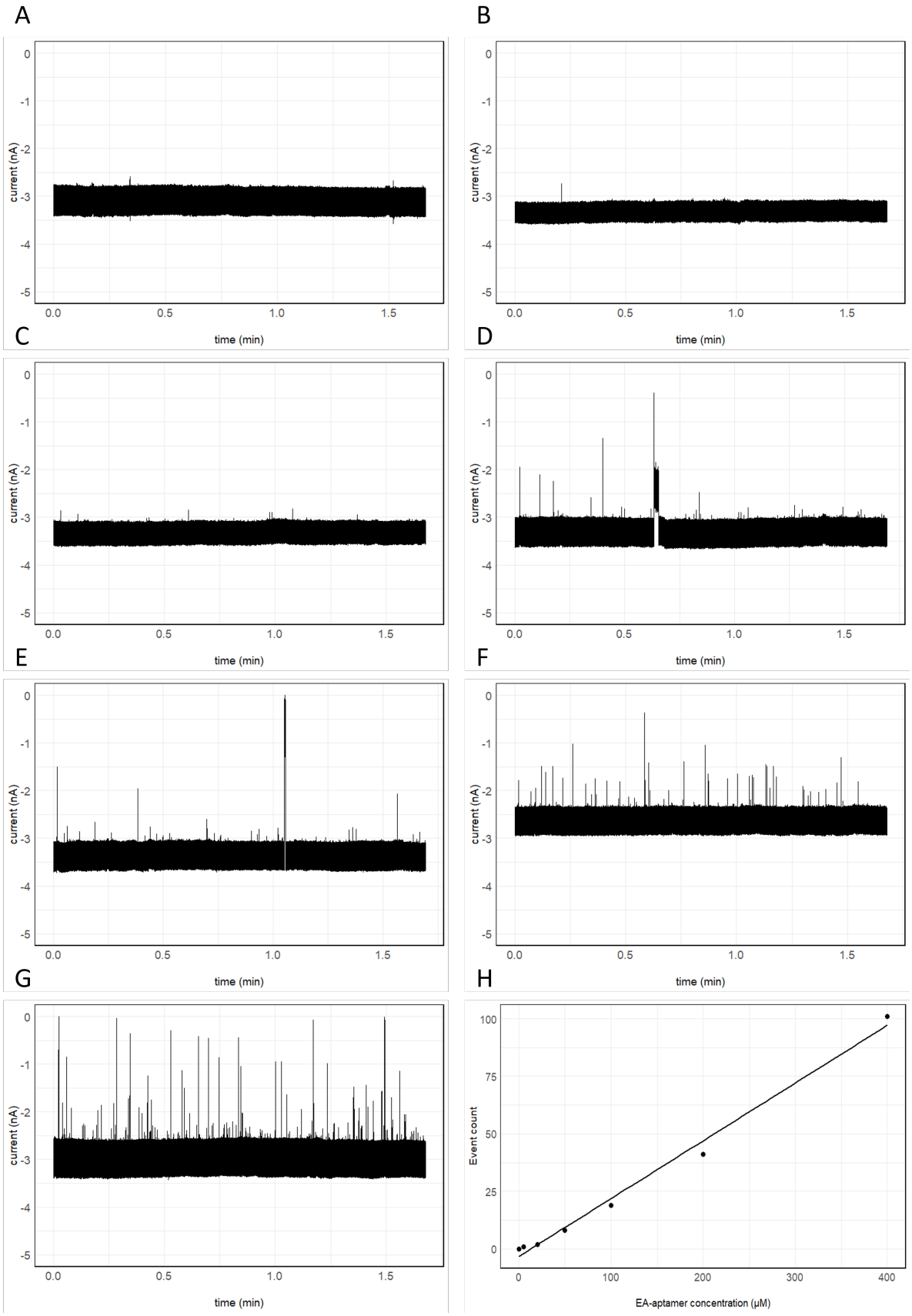

Figure 29: EA-aptamer sensing in 3 nm pore. EA-aptamer in 1 M KCl pH 8 was measured using a 3 nm CBD fabricated nanopore. Current trace recording of **(A)** no EA-aptamer, **(B)** with 5nM EA-aptamer **(C)** with 20 nM EA-aptamer, **(D)** with 50 nM EA-aptamer, **(E)** with 100 nM EA-aptamer, **(F)** with 200 nM EA-aptamer and **(G)** with 400 nM EA-aptamer, were of 100 sec (1.5 min) were shown. **(H)** Event detection for all EA-aptamer concentrations using the EDA software from elements.

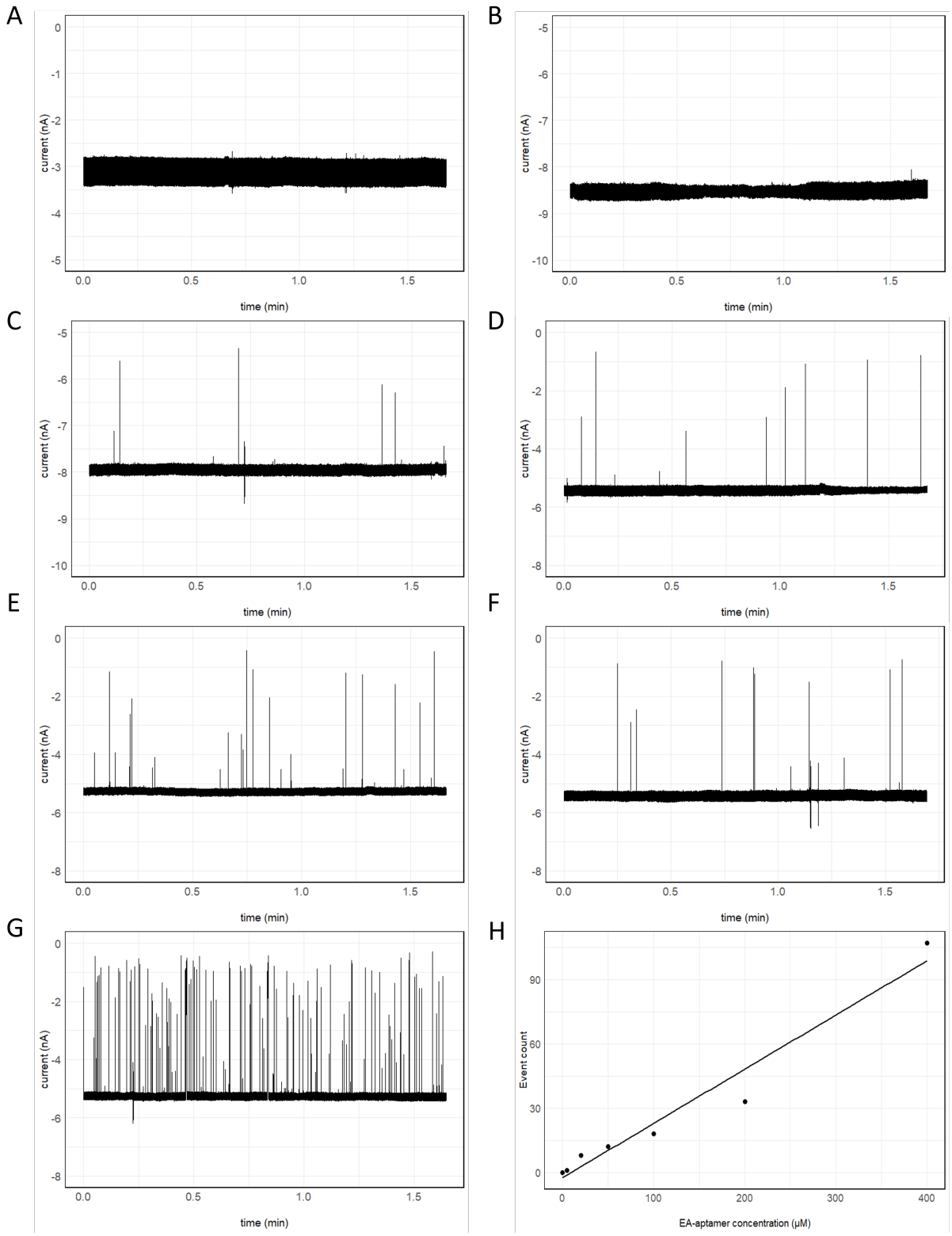

Figure 30: OTA-aptamer sensing in 3 nm pore. OTA-aptamer in 1 M KCl pH 8 was measured using a 3 nm CBD fabricated nanopore. Current trace recording of **(A)** no OTA-aptamer, **(B)** with 5 nM OTA-aptamer, **(C)** with 20 nM OTA-aptamer, **(D)** with 50 nM OTA-aptamer, **(E)** with 100 nM OTA-aptamer, **(F)** with 200 nM OTA-aptamer and **(G)** with 400 nM OTA-aptamer, were of 100 sec (1.5 min) were shown. **(H)** Event detection for all EA-aptamer concentrations using the EDA software from elements.

To investigate whether the different aptamer signals could be distinguished, the signals were analyzed in more detail. The analysis of the current drop (peak amplitude) and translocation time (dwell time) for the EA-aptamer (Figure 31) and OTA-aptamer (Figure 32) are shown below. For the EA-aptamer, dwell times ranged from 0.1 to 3 ms, with the highest event count occurring at 0.2 ms for all aptamer concentrations. At higher concentrations (400 nM), dwell times exceeding 3 ms were observed (Figure 31A). However, these occurrences had low counts and disappeared at lower concentrations, suggesting they resulted from aptamer aggregation or clogging, likely due to increased spatial proximity at higher concentrations. Therefore, these longer dwell times were neglected. The measured amplitude corresponds to the baseline current's mean value. For the EA-aptamer, current drops ranged between 1 and 2 nA across all concentrations. To distinguish different molecules, the signals must differ significantly in terms of dwell time or amplitude. Unfortunately, the OTA-aptamer did not show a significant difference in either parameter compared to the EA-aptamer. The dwell times for the OTA-aptamer were also between 0.1 and 2 ms, with the highest event count at 0.2 ms, and the peak amplitudes ranged from 1 to 2 nA. This suggests that in an unknown sample, distinguishing between OTA- and EA-aptamers would not be possible. This outcome was expected, as both aptamers are similar in size (36 nt for OTA-aptamer and 42 nt for EA-aptamer) and both form quadruplex structures [161, 196], leading to similar blockade events in the nanopore and thus producing similar signals. These results were also confirmed using a 5.7 nm diameter pore. Nanopores with diameters above 6 nm did not show any translocation events for EA- or OTA-aptamer.

In summary, these results show that unmodified ssNPs of appropriate sizes (3-6 nm) can detect small ssDNA aptamer sequences in a concentration-dependent manner, offering the potential for small molecule detection using a strand-displacement assay with magnetic beads. However, nanopore fabrication using CBD proved to be too random, and only a few functional nanopores with the correct pore size and a good signal-to-noise ratio were produced. Another challenge was the stability of the fabricated nanopores. Even if a pore initially showed promise, it often lost functionality after a few measurements—whether or not target molecules were present—due to clogging, damage, or increased noise, leading to unstable baseline currents [81]. As a result, insufficient data was generated to construct a standard curve for both aptamers, hindering the development of an assay for EA or OTA detection in ssNPs. The results from the MinION® nanopores could not be reliably transferred. Moreover, not enough data was generated to evaluate the impact of pore size on signal intensity or shape, making comparisons across experiments with different nanopores extremely challenging.

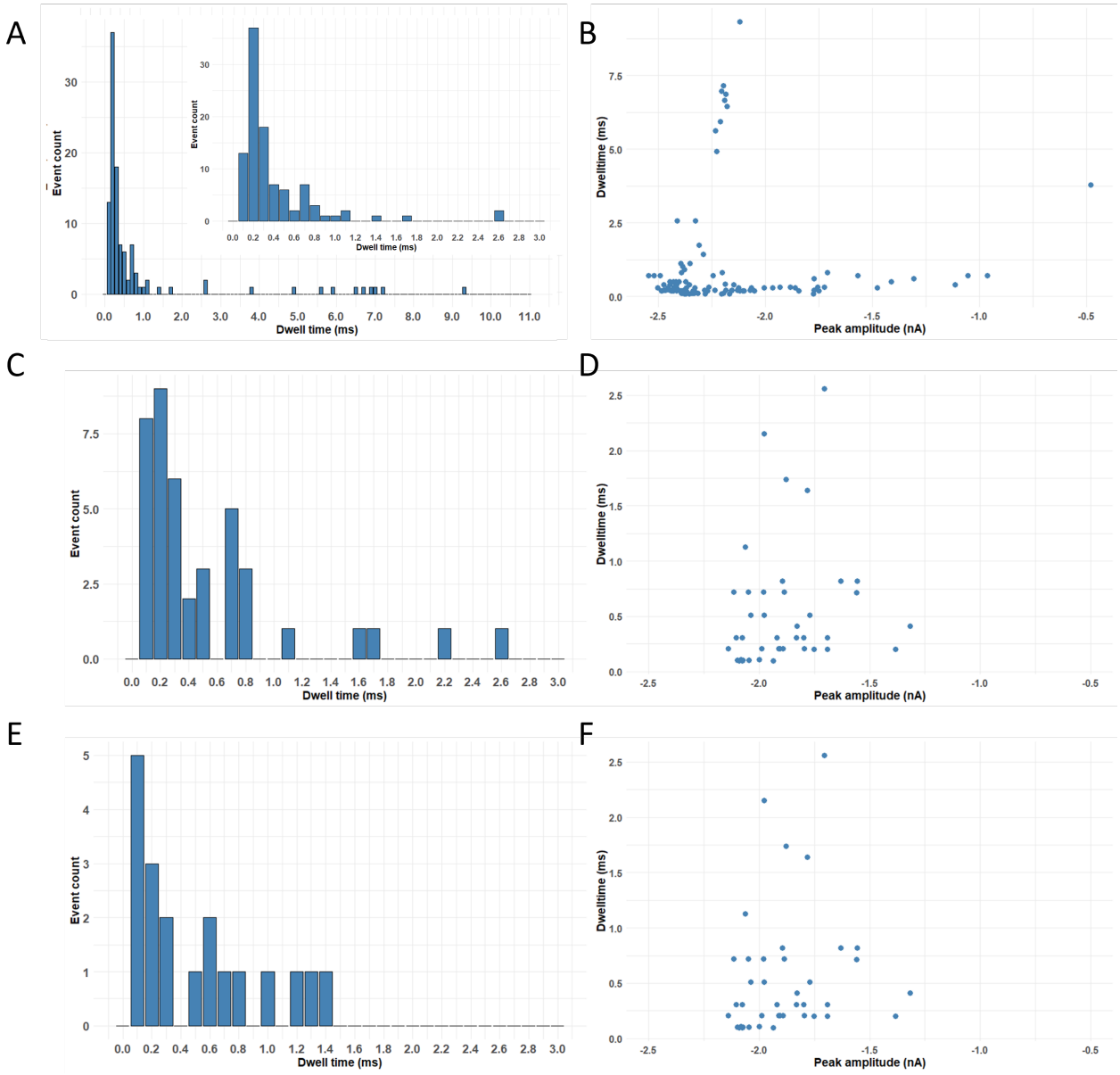

Figure 31: Event detection for EA-aptamer. On the left side the amount of events occuring to different dwell times is shown for **(A)** 400 nM EA-apatmer **(C)** 200 nM EA-aptamer and **(E)** 100 nM EA-aptamer. The right side shows the scatterplot for the peak amplitude in nA against the dwell time in ms **(B, D and F)**. Peak amplitudes are relative to the baseline current.

.

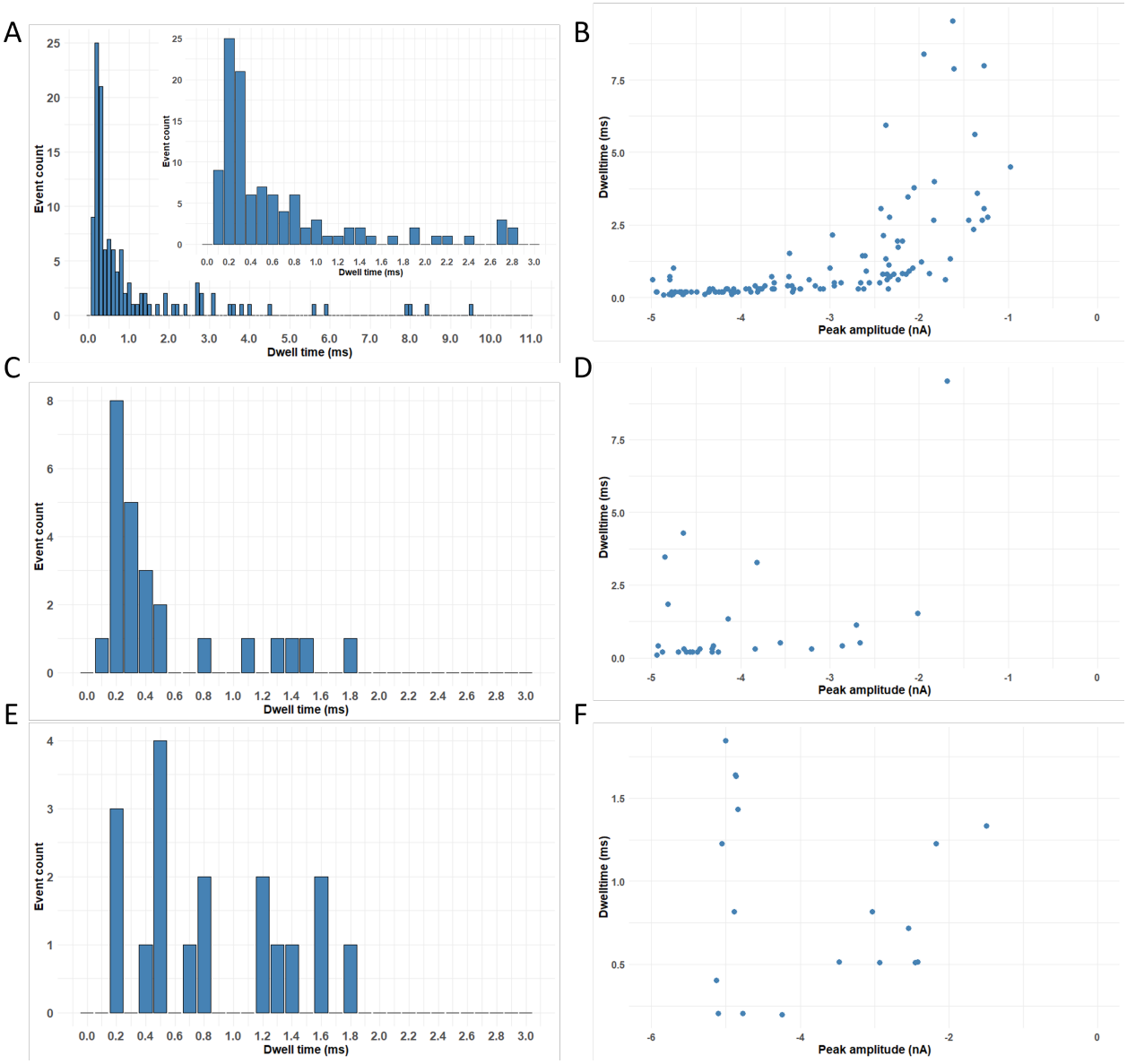

Figure 32: Event detection for OTA-aptamer. On the left side the amount of events occuring to different dwell times is shown for **(A)** 400 nM OTA-apatmer **(C)** 200 nM OTA-aptamer and **(E)** 100 nM OTA-aptamer. The right side shows the scatterplot for the peak amplitude in nA against the dwell time in ms **(B, D and F)**. Peak amplitudes are relative to the baseline current.

.

4.3.1.3 Fabrication method 2: Focused Ion Beam Scanning Electron Microscope

The second approach for nanopore fabrication was using Focused Ion Beam Scanning Electron Microscope (FIB-SEM) milling. This method uses a focused ion beam (typically gallium ions) to mill or sputter atoms from a material surface, creating nanopores by selectively removing material. SEM imaging in the same setup allows for real-time monitoring of pore formation and fine-tuning [197].

First, the optimal parameters for nanopore fabrication in 12 nm thick silicon nitride membranes were tested. Coinciding literature, best results were achieved using 30 kV and 1 pA, as for example using 1 kV led to bigger pore sizes. As shown in Figure 33, a test series of different time intervals using 30 kV and 1 pA was developed. Therefore, the fabrication time was constantly increased. Starting from 10 ms the fabrication time was increased up to 200 ms in 10 ms intervals. Nanopore size was determined using SEM imaging. The results clearly show the influence of fabrication time on pore size, as with increasing fabrication time the pore size also increased. Consequently, 10 ms fabrication time led to the smallest pore size about 20 nm. A further decrease in fabrication time, did not lead to smaller pore sizes, as the pore was not continuous when using I/V-measurement. As a result, the fabrication limit with this gallium ion-beam is 20 nm. This observation is also conscious with literature [198, 199]. But also, the 10 ms fabrication time did not always lead to continuous nanopores, resulting in low reproducibility for small nanopores. Another problem was that during SEM-scanning the nanopore size decreased, this effect was especially striking for small-diameter nanopores. Here sometimes, the nanopore disappeared before a sharp SEM-picture could be captured. This effect refers to the electron beam applied to the nanopore during SEM-imaging [193]. As a result, nanopores of less than 30 nm were difficult to reliably fabricate. Consequently, further FIB-SEM nanopores were fabricated with 30 kV, 1 pA and 90 ms (see Figure 33D). Using these parameters, 50 nm nanopores could be reliably fabricated. As for small molecule detection e.g., of EA-aptamer, small-diameter nanopores were needed, ALD-coating and other surface modification techniques were tested for their ability to reduce the target pore diameter.

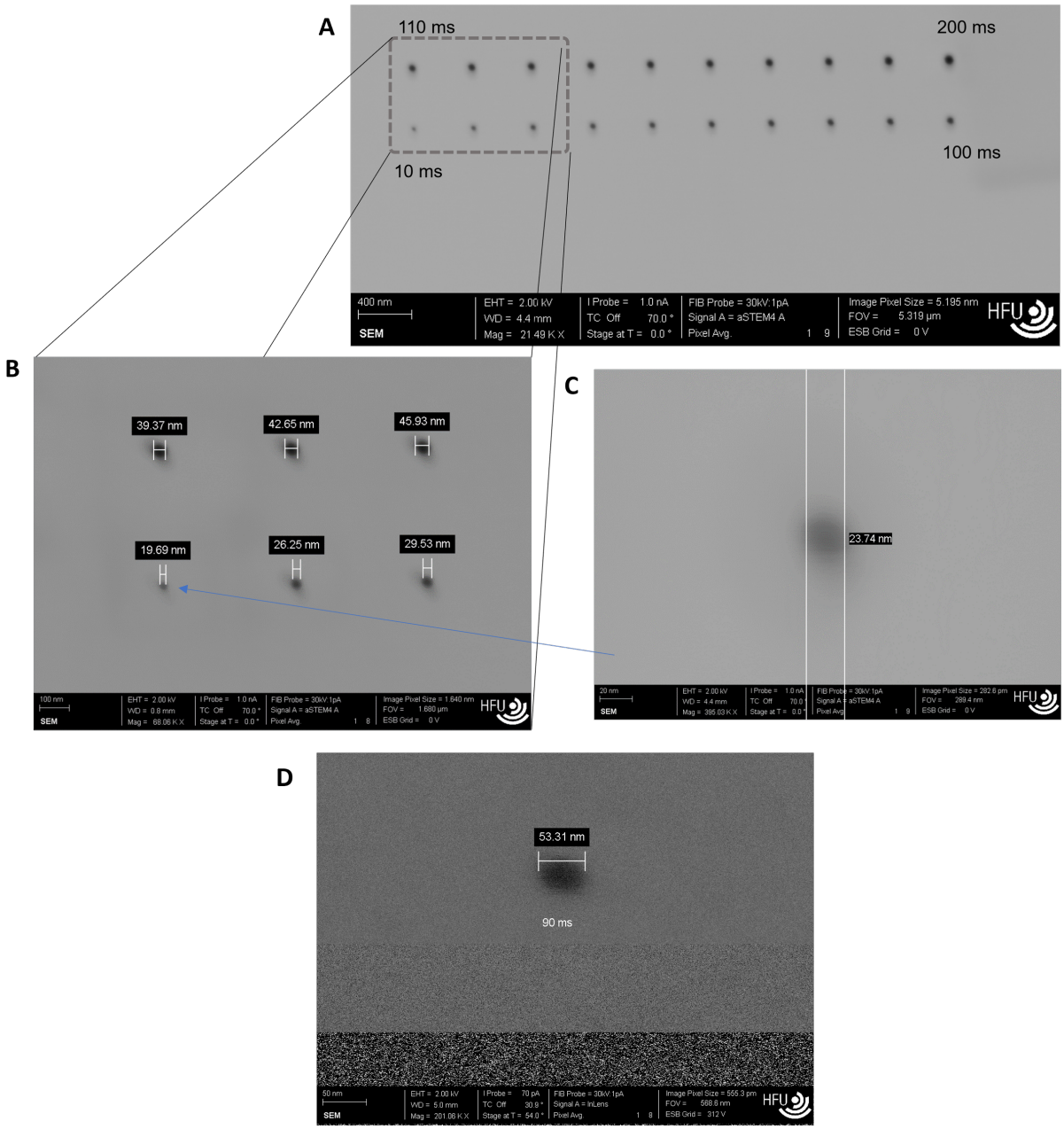

Figure 33: FIB-SEM nanopore fabrication in 12 nm thick silicon nitride chips. (A) shows a SEM-picture of a measurement series of Gallium-FIB fabricated nanopores using 30 kV and 1 pA with different time intervals. Starting from 10 ms (bottom left) to 100 ms (bottom right) and 110 ms (upper left) to 200 ms (upper right). **(B)** shows the zoomed section of the upper picture with different ion-beam times and the estimated diameters using SEM. **(C)** SEM-picture of a nanopore with 23.74 nm fabricated using 30 kV, 1 pA and 10 ms gallium ion-beam. **(D)** SEM-picture of a nanopore with 53.31 nm, fabricated with 30 kV, 1 pA for 90 ms gallium ion-beam.

.

4.3.1.4 Comparison of CBD and FIB-SEM for solid-state nanopore fabrication

One notable advantage of controlled dielectric breakdown (CBD) in solid-state nanopore fabrication is the ability to create nanopores directly in solution, which ensures immediate wettability. This feature is critical for small nanopores (<10 nm) that often require complex wetting procedures with other methods. In contrast, FIB-SEM, necessitates a post-fabrication wetting step due to the drying and cleaning required during fabrication. This additional step can add complexity and time to the fabrication process and may lead to variations in wetting outcomes, which CBD avoids.

When it comes to pore size, both methods have inherent limitations. The CBD method can produce smaller-diameter nanopores directly, making it advantageous for applications requiring nanoscale precision. However, CBD's reliance on a dielectric breakdown event introduces an element of randomness, leading to low reproducibility for sub-5 nm nanopores [193]. Consequently, even though CBD can achieve smaller diameters, controlling this process consistently remains a challenge. FIB-SEM offers a different set of advantages and limitations. Its dependence on ion beam parameters, including current intensity, fabrication time, and ion beam diameter, limits the minimum nanopore size achievable. For example, the specific FIB-SEM device used in this study was constrained to a minimum pore diameter of around 20 nm, due to the technical limitations of the gallium ion beam size [198]. Despite this, FIB-SEM has shown superior control over pore size consistency, resulting in more reproducible outcomes, which are crucial for applications demanding reliability. Baseline current stability, an essential parameter for sensing applications, also differed between the two methods. CBD-fabricated nanopores frequently displayed baseline current instability or noise, which could interfere with precise molecular sensing, likely due to inconsistent pore wall structures. In contrast, FIB-SEM-fabricated nanopores demonstrated a more stable baseline current, likely due to the method's-controlled milling process, which minimizes irregularities at the pore edge.

In summary, while neither CBD nor FIB-SEM is ideal for achieving stable, small-diameter nanopores, each method has distinct strengths. CBD offers the benefit of immediate wettability and can achieve smaller pore sizes, though with limitations in reproducibility and baseline stability. FIB-SEM provides more reliable control over pore size and baseline stability, making it preferable for applications requiring consistent performance. Future optimization may involve fabricating larger, stable nanopores with FIB-SEM, followed by post-fabrication size reduction techniques like atomic layer deposition (ALD), or other covalent surface modification techniques to achieve the precision required for specific applications.

4.3.2 Surface modification of silicon nitride chips

Surface modification of ssNPs with functional groups can effectively reduce non-specific binding and improve the selectivity and sensitivity of small molecule detection. To this end, protocols for covalent attachment of aminated aptamer sequences and IgG antibodies (used as model molecules) were developed and optimized on both blank chips and chips following nanopore fabrication.

As shown in Figure 34A, the FTIR spectrum of unmodified (blank) nanopore chips displays a prominent peak at 860 cm^{-1}, indicative of Si-N bond stretching, a smaller peak at 1100 cm^{-1} corresponding to Si-O-Si bonds, and a broad peak at 3500 cm^{-1} that signals the presence of free OH groups. Following silanization, the spectrum changes significantly: a large peak appears at 2800–2900 cm^{-1}, corresponding to C-H bond stretching, while peaks in the 1400–1700 cm^{-1} range indicate N-H bond bending (see Figure 34B). These spectral changes confirm successful APTES functionalization, which involves a carbon chain ending with an amino group. The uniform spectra across the chip surface suggest consistent APTES coverage. After antibody binding, additional spectral changes were observed, particularly a peak between 1600–1700 cm^{-1} that indicates an amide I band from C=O stretching, characteristic of antibody attachment. Microscopic images corroborated these stages of surface modification. When FITC-labeled IgG antibodies were attached, the chip displayed an even fluorescence signal at 532 nm in the fluorescence reader, supporting uniform antibody distribution (see Figure 34C). Fluorescently labeled aptamer sequences produced similar fluorescence signals (data not shown).

These findings demonstrate that surface functionalization with aptamers or IgG antibodies can be achieved through silanization and glutaraldehyde crosslinking for stable amino-group binding. This approach offers a promising method for attaching target-specific antibodies to the nanopore surface, potentially enhancing signal sensitivity. Furthermore, either EA-aptamer or OTA-aptamer sequences, or their complementary strands, could be attached to the nanopore surface in the same way, representing a potential optimization for ssNP-based assays targeting EA or OTA. However, consistent results were achieved only on blank chips, as chips with nanopores were frequently damaged or irreversibly clogged during the modification process. Additionally, it was not possible to confirm whether surface modification effectively extended inside the nanopore itself. Consequently, no molecule sensing experiments were conducted with functionalized ssNPs in this study.

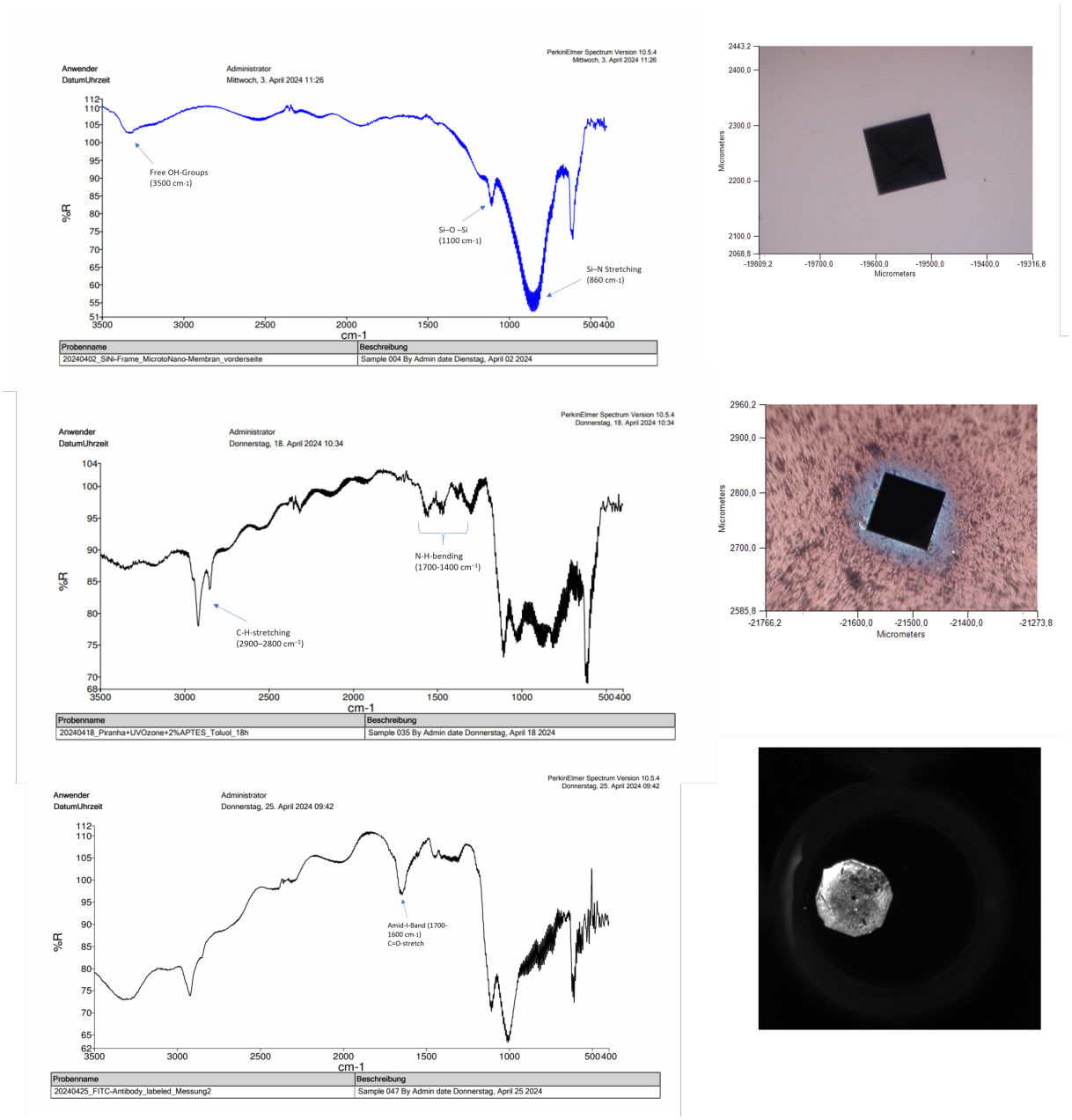

Figure 34: FTIR-spectra of (A) unfunctionalized silicon nitride surface **(B)** after silanization **(C)** after FITC-labeled IgG antibody.

.

Aside from functional group modifications reported in the literature, ALD coating has been shown to precisely reduce nanopore size, enhancing stability [200]. However, post-fabrication ALD coating of 50 nm FIB-SEM-fabricated nanopores did not yield the desired results, as pores tended to clog after treatment. Verifying size reduction was also challenging, as repeated SEM imaging could further shrink the nanopore or lead to complete closure [193]. Additionally, SEM-derived pore sizes often differed from I/V measurements.

Even when successful, pore size reduction came at the cost of increased membrane thickness, which in turn elevated the signal-to-noise ratio, negatively impacting sensing performance. Crucially, ALD coating failed to achieve the sub-10 nm diameters required for small molecule detection. Further optimization and expertise in ALD processing are needed to address these limitations. Due to the unsuitability of ALD-coated nanopores for molecule sensing, data were not included.

4.4 Summary of results for ssNPs

To sum up, ssNPs still face significant challenges for small molecule sensing applications, with reproducible fabrication being one of the most critical issues. High reproducibility is essential to ensure that nanopores exhibit consistent properties; without it, the development of reliable sensing assays or commercial devices is hindered. Fabrication methods like controlled dielectric breakdown (CBD) are prone to randomness, particularly for smaller nanopores, where variations in the dielectric breakdown process make precise control difficult. Although FIB-SEM offers better reproducibility, it is costly and time-intensive, limiting its practicality for large-scale production. Achieving specific pore diameters and shapes with consistency is another challenge, especially for applications like DNA sequencing and single-molecule sensing, where even slight variations can lead to inaccurate results. While CBD can produce a range of pore sizes, precise control is especially difficult for nanopores smaller than 10 nm. FIB milling provides more controlled outcomes but is limited by ion beam diameter, which typically restricts the minimum pore size to larger diameters unless post-fabrication techniques, such as atomic layer deposition (ALD), are applied. Another key issue is achieving adequate wettability. Nanopores need to be fully wetted to conduct ionic current, a requirement for most sensing applications. Small nanopores, especially those under 10 nm, tend to resist wetting, leading to air bubbles or incomplete filling. Non-wetted nanopores block current flow, rendering them ineffective for sensing. While techniques like chemical surface treatments, plasma treatments, and controlled fabrication environments can help, they add complexity and may still yield inconsistent results for ultra-small pores. Beyond fabrication, the stability and durability of ssNPs also present challenges. The nanopore membrane must be thin enough for high sensitivity but strong enough to withstand the stresses of fabrication and operation. Thin membranes (e.g., <20 nm) are more fragile and prone to breake during fabrication or when subjected to high voltages. Conversely, thicker membranes are more durable but reduce sensitivity for small molecules and ions due to longer transit times. Post-fabrication functionalization and ALD-coating pose further challenges. Functionalizing or coating nanopores to tailor properties, such as selectivity, hydrophilicity, and chemical sensitivity, can change pore size or shape, impact stability, and add steps to the fabrication process. Achieving uniform functionalization at the nanoscale is particularly difficult, especially for very small nanopores, but is often essential to optimize their performance for specific applications.

The findings of this study align with the challenges described, as using CBD, nanopores down to 3 nm could be fabricated but only with low reproducibility (1 out of 20). Additionally, these small nanopores exhibited unstable baseline currents and a tendency to expand or clog during sensing experiments, making it impossible to develop a quantitative assay for detecting EA or OTA, as seen in previous work with protein nanopores (see 4.2). Attempts to use surface modifications to increase sensitivity, improve stability, or further reduce pore size did not yield satisfactory results, as the nanopores were frequently damaged or clogged during the process. Furthermore, confirmation of functionalization within the nanopore channels was inconclusive; FTIR- spectroscopy could only verify modifications on the chip surface, not inside the nanopore itself. Although FIB-SEM fabricated nanopores demonstrated improved stability and durability, reproducibly fabricating nanopores below 20 nm with a gallium ion beam proved challenging. Consequently, this method also fell short for small molecule sensing applications. Efforts to reduce pore diameter further through post-fabrication ALD-coating with aluminum oxide, when successful, did result in smaller diameters, but at the cost of a thicker membrane, which reduced sensitivity. Starting with a 50 nm pore size, ALD-coating failed to produce functional nanopores with diameters below 5 nm, suitable for molecular sensing. In summary, while ssNPs remain a promising platform for small molecule sensing, significant challenges, such as reproducible fabrication, stable current profiles, effective functionalization, and scalability, must be addressed to unlock their full potential for these applications.

5 Summary and Outlook

The results of this research underscore the critical importance of developing new sensing technologies for small molecule detection, as they play an essential role in molecular diagnostics and personalized medicine. Despite the progress made in this field, designing assay systems with high specificity and sensitivity that allow for label-free, rapid, and straightforward detection of small molecules still presents challenges. This study explores and evaluates three distinct approaches for small molecule detection, each contributing to advancing the field in a unique way.

First in chapter 4.1, a fluorescence magnetic-bead-based competitive antibody binding assay for L-Kynurenine was developed. This assay demonstrates how antibody-based detection systems can be optimized for greater sensitivity, making small molecule detection feasible when a specific binding antibody is available. The successful synthesis of a fluorescent kynurenine conjugate based on rhodamine B, coupled with its unique antibody binding properties, demonstrated good sensitivity with a KD-value of 5.9 μM for the L-Kynurenine conjugate and IC50 values of 4.0 μM in PBS and 10.2 μM in saliva for the competitive assay with native kynurenine. As expected, the IC50 value in saliva was higher than in PBS due to interfering components such as enzymes and proteins in saliva samples. Nevertheless, these findings present a promising step forward in the development of rapid diagnostic tests for kynurenine as a diagnostic marker for diseases, such as kidney transplant failure, where kynurenine levels in saliva increase to 4.6 +/- 1.6 μM under pathological conditions [128]. These results also demonstrate that immunoassays have yet to reach their full potential and can be applied not only to larger antigens but also to small molecule detection, provided they are optimized with new technologies and advancements in antibody development for small biomarkers. Additionally, conjugation chemistry plays a crucial role in creating fluorescent labeling techniques that do not interfere with antigen-antibody binding.

This dissertation also focused on the development of an assay system based on novel molecular sensors (chapter 4.2), such as nanopore sensors. Nanopores as sensors for small molecules offer a promising alternative to complex and costly standard methods like HPLC or LC-MS, having been extensively studied and established, particularly in DNA analytics. However, there are still few practical publications or applications for small molecule detection. The main challenge lies in the stability and longevity of these nanopores, especially in the lower nanometer range. The protein nanopores of an established nanopore-based sequencer proved effective for detecting small molecules using target-binding aptamers. This involves the controlled, current-independent translocation of target-binding aptamers without requiring complex sample preparation. A ready-to-use nanopore platform for label-free quantification of small

molecules, using ethanolamine as an example, was successfully developed, demonstrating the potential of protein nanopores for small molecule detection.

The developed magnetic-bead-based strand displacement assay illustrates a possible application of protein nanopores for small biomarker detection. These results show that the ONT protein nanopore system, traditionally used for DNA/RNA sequencing, can also detect and quantify small molecules, provided a suitable aptamer is available. Since this process remains difficult and expensive with conventional methods but plays a crucial role in diagnosing numerous diseases, it represents a significant step toward simplifying and reducing the cost of such detections in future diagnostics.

One example is the strand displacement assay for ethanolamine and its binding aptamer. The results revealed that ethanolamine could be indirectly detected by measuring its binding aptamer via the protein nanopores, with sensitivity in the micromolar range. The ethanolamine aptamer showed significant current interruptions, ranging from 240 pA to 60, 80, or 100 pA during molecular translocation, exhibiting a characteristic wave-like pattern. Using the strand-displacement assay, ethanolamine concentrations between 5 and 20 μM, were reliably detected, with a dissociation constant (Kd) of 14.4 μM. This approach shows promise for clinical applications, as the device offers a cost-effective and well-established platform. Moreover, this methodology can be adapted to other small molecules with suitable aptamers of similar structure and size. The long translocation time of 1–2 seconds observed is likely due to the G-quadruplex tertiary structure of the aptamer. As such quadruplex structures are common in other aptamers, this method could be applied to detect other small molecules using their specific aptamers. However, this hypothesis requires further confirmation in future studies.

Additionally, the Nanotrace software developed here enables scientists, even without a bioinformatics background, to easily visualize the generated bulk-fast5 files. This presents a significant advantage over other available software tools, which typically require Python-based programming skills. To sum it up the methodology described serves as a proof of principle that can be adapted to other small molecules with suitable binding aptamers of similar structure, marking an important step toward simplifying small molecule diagnostics.

Furthermore, this disseration explored the use of ssNPs for small molecule detection (chapter 4.3). The investigation into nanopore technologies extended to the fabrication of ssNPs through two distinct methods: CBD and FIB-SEM. While FIB-SEM demonstrated limitations in precision, especially for small-diameter nanopores (below 20 nm), the CBD method showed promising potential for fabricating smaller nanopores (<6 nm). Despite challenges in reproducibility and stability, the research demonstrated that ssNPs fabricated with CBD could successfully and quantitatively detect the two G-quadruplex-forming aptamers of the small molecules ethanolamine and ochratoxin. Both aptamers showed increasing translocation events up to 400 nM with a

LOD of 50 nM. Due to their comparable length and structure, both exhibited similar translocation times between 0.1 and 0.2 ms, making it challenging to distinguish between the two molecules in a single assay. Although sufficient data could not be obtained to develop a reliable strand displacement using ssNPs due to reproducibility issues, these results suggest that ssNPs could serve as a valuable tool for small molecule detection in the future, as the basic requirements of quantitative aptamer detection could be clearly demonstrated. The small diameter nanopores fabricated through CBD represent a promising technology for the next generation of diagnostic sensors, provided that the fabrication process can be refined to improve stability, wetting, and reproducibility.

While the advancements presented in this dissertation are promising, several key challenges remain. The reproducibility and stability of small-diameter nanopores, particularly in the context of ssNPs, require further investigation. Fabricating nanopores with diameters smaller than 6 nm has proven difficult, and additional optimization is needed to achieve reliable detection. Moreover, the prolonged translocation times observed in protein nanopore assays indicate the need for further refinement of aptamer structures and nanopore systems to improve detection speed and efficiency. Optimizing surface functionalization methods is also crucial in this regard. Additionally, developing more robust software tools like Nanotrace is essential to enhance the analysis of nanopore output data and make this technology more accessible to a wider range of researchers, particularly those without a bioinformatics background.

Future research should focus on several key areas: (1) improving the materials and fabrication methods for ssNPs to ensure greater reliability and reproducibility; (2) enhancing the sensitivity and specificity of aptamer-based detection systems, especially for clinical applications; (3) optimizing the nanopore technologies to overcome the limitations in translocation time and detection accuracy; and (4) further developing user-friendly software platforms to analyze nanopore data. By addressing these challenges, small molecule detection technologies can be advanced to a level where they are practical for routine clinical diagnostics, particularly for personalized medicine. In conclusion, this research makes significant contributions to the field of small molecule detection by not only optimizing traditional immunoassays to enhance their sensitivity for small molecule application but introducing novel assay methods and demonstrating the feasibility of using aptamers for small molecule detection in both protein nanopores and ssNPs. These findings lay the groundwork for future diagnostic technologies that are more cost-effective and accessible. While several challenges remain, the insights gained through this study represent a crucial step toward improving molecular diagnostics. Further research into optimizing ssNPs, enhancing aptamer-based detection, and addressing fabrication and stability issues will be critical for advancing these technologies to the point where they can be implemented in clinical practice, offering improved diagnostic capabilities for a range of diseases.

Bibliography

[1] Isabel Quint et al. “Ready-to-use nanopore platform for label-free small molecule quantification: Ethanolamine as first example”. In: *Nanomedicine : nanotechnology, biology, and medicine* 55 (2024), p. 102724. DOI: 10.1016/j.nano.2023.102724.

[2] Max Borgolte et al. “A Fluorescence-Based Competitive Antibody Binding Assay for Kynurenine, a Potential Biomarker of Kidney Transplant Failure”. In: *Diagnostics (Basel, Switzerland)* 12.6 (2022). ISSN: 2075-4418. DOI: 10.3390/diagnostics12061380.

[3] Harshvardhan Modh. *Detection of Small Molecules Using Aptamers*. Master’s thesis, Leibniz Universität Hannover. Institutionelles Repositorium der Leibniz Universität Hannover, 2019. DOI: 10.15488/4828.

[4] Andrew J. Wilson. “Inhibition of protein-protein interactions using designed molecules”. In: *Chemical Society reviews* 38.12 (2009), pp. 3289–3300. DOI: 10.1039/b807197g.

[5] Sneha Govardhanagiri, Shipra Bethi, and Ganji Purnachandra Nagaraju. “Small Molecules and Pancreatic Cancer Trials and Troubles”. In: *Breaking Tolerance to Pancreatic Cancer Unresponsiveness to Chemotherapy*. Elsevier, 2019, pp. 117–131. ISBN: 9780128176610. DOI: 10.1016/B978-0-12-817661-0.00008-1.

[6] Erica J. Carbone et al. “Small molecule delivery through nanofibrous scaffolds for musculoskeletal regenerative engineering”. In: *Nanomedicine: Nanotechnology, Biology and Medicine* 10.8 (2014), pp. 1691–1699. ISSN: 15499634. DOI: 10.1016/j.nano.2014.05.013.

[7] Gyuhyung Jin and Sean P. Palecek. “Inductive factors for generation of pluripotent stem cell-derived cardiomyocytes”. In: *Engineering Strategies for Regenerative Medicine*. Elsevier, 2020, pp. 177–242. ISBN: 9780128162217. DOI: 10.1016/B978-0-12-816221-7.00006-9.

[8] Xu Wang et al. “Competitive Immunoassays for the Detection of Small Molecules Using Single Molecule Arrays”. In: *Journal of the American Chemical Society* 140.51 (2018), pp. 18132–18139. DOI: 10.1021/jacs.8b11185.

[9] Cristina Adrover-Jaume et al. “A paper biosensor for overcoming matrix effects interfering with the detection of sputum pyocyanin with competitive immunoassays”. In: *Mikrochimica acta* 190.11 (2023), p. 441. DOI: 10.1007/s00604-023-06017-1.

[10] Gunnar Brandhorst et al. “Liquid chromatography-tandem mass spectrometry or automated immunoassays: what are the future trends in therapeutic drug monitoring?” In: *Clinical chemistry* 58.5 (2012), pp. 821–825. DOI: 10.1373/clinchem.2011.167189.

[11] Gejing Deng and Gautam Sanyal. “Applications of mass spectrometry in early stages of target based drug discovery”. In: *Journal of pharmaceutical and biomedical analysis* 40.3 (2006), pp. 528–538. ISSN: 0731-7085. DOI: 10.1016/j.jpba.2005.08.038.

[12] Mohammed Jemal and Yuan-Qing Xia. “LC-MS Development strategies for quantitative bioanalysis”. In: *Current drug metabolism* 7.5 (2006), pp. 491–502. ISSN: 1389-2002. DOI: 10.2174/138920006777697927.

[13] W. Franklin Smyth and Peter Brooks. “A critical evaluation of high performance liquid chromatography-electrospray ionisation-mass spectrometry and capillary electrophoresis-electrospray-mass spectrometry for the detection and determination of small molecules of significance in clinical and forensic science”. In: *Electrophoresis* 25.10-11 (2004), pp. 1413–1446. ISSN: 0173-0835. DOI: 10.1002/elps.200305850.

[14] Kirstie Canene-Adams. “Reverse-phase HPLC analysis and purification of small molecules”. In: *Methods in enzymology* 533 (2013), pp. 291–301. DOI: 10.1016/B978-0-12-420067-8.00023-4.

[15] Nicholas W. Kwiecien et al. “High-resolution filtering for improved small molecule identification via GC/MS”. In: *Analytical chemistry* 87.16 (2015), pp. 8328–8335. DOI: 10.1021/acs.analchem.5b01503.

[16] Ray Bakhtiar and Tapan K. Majumdar. “Tracking problems and possible solutions in the quantitative determination of small molecule drugs and metabolites in biological fluids using liquid chromatography–mass spectrometry”. In: *Journal of Pharmacological and Toxicological Methods* 55.3 (2007), pp. 227–243. ISSN: 10568719. DOI: 10.1016/j.vascn.2006.10.002.

[17] Andy Chieng, Zijian Wan, and Shaopeng Wang. “Recent Advances in Real-Time Label-Free Detection of Small Molecules”. In: *Biosensors* 14.2 (2024), p. 80. DOI: 10.3390/bios14020080. URL: https://www.ncbi.nlm.nih.gov/pmc/articles/PMC10886562/.

[18] Obtin Alkhamis et al. “Innovative engineering and sensing strategies for aptamer-based small-molecule detection”. In: *Trends in analytical chemistry : TRAC* 121 (2019). ISSN: 0165-9936. DOI: 10.1016/j.trac.2019.115699.

[19] Shengnan Fu et al. “DNA nanotechnology enhanced single-molecule biosensing and imaging”. In: *Trends in analytical chemistry : TRAC* 140 (2021), p. 116267. ISSN: 0165-9936. DOI: 10.1016/j.trac.2021.116267.

[20] Don Hui Lee, Won-Yong Lee, and Jayoung Kim. “Introducing Nanoscale Electrochemistry in Small-Molecule Detection for Tackling Existing Limitations of Affinity-Based Label-Free Biosensing Applications”. In: *Journal of the American Chemical Society* 145.32 (2023), pp. 17767–17778. ISSN: 0002-7863. DOI: 10.1021/jacs.3c04458.

[21] Muhammad Saleem et al. “Recent Development on Sensing Strategies for Small Molecules Detections”. In: *Journal of fluorescence* 34.4 (2024), pp. 1493–1525. DOI: 10.1007/s10895-023-03387-w.

[22] Long Ma et al. “Sensitive Small Molecule Aptasensing based on Hybridization Chain Reaction and CRISPR/Cas12a Using a Portable 3D-Printed Visualizer”. In: *ACS sensors* 8.3 (2023), pp. 1076–1084. DOI: 10.1021/acssensors.2c02097.

[23] Xiuli Fu, Lingxin Chen, and Jaebum Choo. “Optical Nanoprobes for Ultrasensitive Immunoassay”. In: *Analytical chemistry* 89.1 (2017), pp. 124–137. DOI: 10.1021/acs.analchem.6b02251.

[24] Zheyu Wang et al. “Plasmonically-enhanced competitive assay for ultrasensitive and multiplexed detection of small molecules”. In: *Biosensors and Bioelectronics* 200 (2022), p. 113918. ISSN: 09565663. DOI: 10.1016/j.bios.2021.113918.

[25] Eiki Watanabe, Shiro Miyake, and Yasuhiro Yogo. “Review of Enzyme-Linked Immunosorbent Assays (ELISAs) for Analyses of Neonicotinoid Insecticides in Agro-environments”. In: *Journal of agricultural and food chemistry* 61.51 (2013), pp. 12459–12472. ISSN: 0021-8561. DOI: 10.1021/jf403801h.

[26] Karen L. Cox et al. *Assay Guidance Manual: Immunoassay Methods*. Bethesda (MD), 2004.

[27] Seiichi Sakamoto et al. “Enzyme-linked immunosorbent assay for the quantitative/qualitative analysis of plant secondary metabolites”. In: *Journal of Natural Medicines* 72.1 (2018), pp. 32–42. ISSN: 1340-3443. DOI: 10.1007/s11418-017-1144-z.

[28] M. E. Clementi et al. “Antibodies against small molecules”. In: *Annali dell'Istituto superiore di sanita* 27.1 (1991), pp. 139–143. ISSN: 0021-2571.

[29] Catalin Nistor and Jenny Emnéus. “Chapter 9 Immunoassay: potentials and limitations”. In: *Biosensors and Modern Biospecific Analytical Techniques*. Vol. 44. Comprehensive Analytical Chemistry. Elsevier, 2005, pp. 375–427. ISBN: 9780444507150. DOI: 10.1016/S0166-526X(05)44009-X.

[30] Jared A. Carter et al. “A label-free, multiplex competitive assay for small molecule pollutants”. In: *Biosensors & bioelectronics* 77 (2016), pp. 1–6. DOI: 10.1016/j.bios.2015.08.064.

[31] Patrick M. Sluss and Frances J. Hayes. “Laboratory Techniques for Recognition of Endocrine Disorders”. In: *Williams Textbook of Endocrinology*. Elsevier, 2016, pp. 77–107. ISBN: 9780323297387. DOI: 10.1016/B978-0-323-29738-7.00006-X.

[32] K. V. Singh et al. “Synthesis and characterization of hapten-protein conjugates for antibody production against small molecules”. In: *Bioconjugate chemistry* 15.1 (2004), pp. 168–173. ISSN: 1043-1802. DOI: 10.1021/bc034158v.

[33] Mei-Miao Zhan et al. “From monoclonal antibodies to small molecules: the development of inhibitors targeting the PD-1/PD-L1 pathway”. In: *Drug discovery today* 21.6 (2016), pp. 1027–1036. DOI: 10.1016/j.drudis.2016.04.011.

[34] D. Modena et al. “Production and characterization of murine monoclonal antibodies to polypeptide hormones and their fragments”. In: *Annali dell'Istituto superiore di sanita* 27.1 (1991), pp. 167–174. ISSN: 0021-2571.

[35] Javier Adrian et al. “Generation of broad specificity antibodies for sulfonamide antibiotics and development of an enzyme-linked immunosorbent assay (ELISA) for the analysis of milk samples”. In: *Journal of agricultural and food chemistry* 57.2 (2009), pp. 385–394. ISSN: 0021-8561. DOI: 10.1021/jf8027655.

[36] O. N. Chappey, P. Sandouk, and J. M. Scherrmann. “Monoclonal antibodies in hapten immunoassays”. In: *Pharmaceutical research* 9.11 (1992), pp. 1375–1379. ISSN: 0724-8741. DOI: 10.1023/a:1015890208714.

[37] Michaela Domsicova et al. “New Insights into Aptamers: An Alternative to Antibodies in the Detection of Molecular Biomarkers”. In: *International journal of molecular sciences* 25.13 (2024). DOI: 10.3390/ijms25136833.

[38] Tatsuo Adachi and Yoshikazu Nakamura. “Aptamers: A Review of Their Chemical Properties and Modifications for Therapeutic Application”. In: *Molecules (Basel, Switzerland)* 24.23 (2019). DOI: 10.3390/molecules24234229.

[39] Varatharasa Thiviyanathan and David G. Gorenstein. “Aptamers and the next generation of diagnostic reagents”. In: *Proteomics. Clinical applications* 6.11-12 (2012), pp. 563–573. ISSN: 1862-8346. DOI: 10.1002/prca.201200042.

[40] A. D. Ellington and J. W. Szostak. “In vitro selection of RNA molecules that bind specific ligands”. In: *Nature* 346.6287 (1990), pp. 818–822. ISSN: 1476-4687. DOI: 10.1038/346818a0.

[41] C. Tuerk and L. Gold. “Systematic evolution of ligands by exponential enrichment: RNA ligands to bacteriophage T4 DNA polymerase”. In: *Science (New York, N.Y.)* 249.4968 (1990), pp. 505–510. ISSN: 0036-8075. DOI: 10.1126/science.2200121.

[42] Jing Mi et al. “In vivo selection of tumor-targeting RNA motifs”. In: *Nature chemical biology* 6.1 (2010), pp. 22–24. DOI: 10.1038/nchembio.277.

[43] Michael Kohlberger and Gabriele Gadermaier. “SELEX: Critical factors and optimization strategies for successful aptamer selection”. In: *Biotechnology and applied biochemistry* 69.5 (2022), pp. 1771–1792. DOI: 10.1002/bab.2244.

[44] Tilman Schlotter et al. “Aptamer-Functionalized Interface Nanopores Enable Amino Acid-Specific Peptide Detection”. In: *ACS nano* 18.8 (2024), pp. 6286–6297. DOI: 10.1021/acsnano.3c10679.

[45] Miten Jain et al. “The Oxford Nanopore MinION: delivery of nanopore sequencing to the genomics community”. In: *Genome biology* 17.1 (2016), p. 239. DOI: 10.1186/s13059-016-1103-0.

[46] Yi-Lun Ying et al. “Nanopore-based technologies beyond DNA sequencing”. In: *Nature nanotechnology* 17.11 (2022), pp. 1136–1146. ISSN: 1748-3387. DOI: 10.1038/s41565-022-01193-2.

[47] Runyu Wang et al. “Recent advances of small molecule detection in nanopore sensing”. In: *Talanta* 277 (2024), p. 126323. DOI: 10.1016/j.talanta.2024.126323.

[48] Farzin Haque et al. “Solid-State and Biological Nanopore for Real-Time Sensing of Single Chemical and Sequencing of DNA”. In: *Nano today* 8.1 (2013), pp. 56–74. ISSN: 1748-0132. DOI: 10.1016/j.nantod.2012.12.008.

[49] John E. Butler, ed. *Immunochemistry of solid-phase immunoassay*. Boca Raton: CRC Press, 1991. ISBN: 9780367812775.

[50] J. Li et al. “Ion-beam sculpting at nanometre length scales”. In: *Nature* 412.6843 (2001), pp. 166–169. ISSN: 1476-4687. DOI: 10.1038/35084037.

[51] Bo Zhang et al. “Bench-top method for fabricating glass-sealed nanodisk electrodes, glass nanopore electrodes, and glass nanopore membranes of controlled size”. In: *Analytical chemistry* 79.13 (2007), pp. 4778–4787. DOI: 10.1021/ac070609j.

[52] Xin Wu, Haiyan Zhao, and Jiayun Pei. “Fabrication of nanopore in graphene by electron and ion beam irradiation: Influence of graphene thickness and substrate”. In: *Computational Materials Science* 102 (2015), pp. 258–266. ISSN: 09270256. DOI: 10.1016/j.commatsci.2015.02.042.

[53] L. Song et al. “Structure of staphylococcal alpha-hemolysin, a heptameric transmembrane pore”. In: *Science (New York, N.Y.)* 274.5294 (1996), pp. 1859–1866. ISSN: 0036-8075. DOI: 10.1126/science.274.5294.1859.

[54] Michael Faller, Michael Niederweis, and Georg E. Schulz. “The structure of a mycobacterial outer-membrane channel”. In: *Science* 303.5661 (2004), pp. 1189–1192. ISSN: 1095-9203. DOI: 10.1126/science.1094114.

[55] Richard M. A. Manara, E. Jayne Wallace, and Syma Khalid. “DNA sequencing with MspA: Molecular Dynamics simulations reveal free-energy differences between sequencing and non-sequencing mutants”. In: *Scientific reports* 5 (2015), p. 12783. DOI: 10.1038/srep12783.

[56] O. Braha et al. “Simultaneous stochastic sensing of divalent metal ions”. In: *Nature biotechnology* 18.9 (2000), pp. 1005–1007. ISSN: 1087-0156. DOI: 10.1038/79275.

[57] Hai-Chen Wu and Hagan Bayley. “Single-molecule detection of nitrogen mustards by covalent reaction within a protein nanopore”. In: *Journal of the American Chemical Society* 130.21 (2008), pp. 6813–6819. ISSN: 0002-7863. DOI: 10.1021/ja8004607.

[58] S. Howorka, S. Cheley, and H. Bayley. “Sequence-specific detection of individual DNA strands using engineered nanopores”. In: *Nature biotechnology* 19.7 (2001), pp. 636–639. ISSN: 1087-0156. DOI: 10.1038/90236.

[59] Deanpen Japrung et al. “Urea Facilitates the Translocation of Single-Stranded DNA and RNA Through the α-Hemolysin Nanopore”. In: *Biophysical Journal* 98.9 (2010), pp. 1856–1863. ISSN: 0006-3495. DOI: 10.1016/j.bpj.2009.12.4333.

[60] Zheng–Li Hu et al. “Biological Nanopore Approach for Single–Molecule Protein Sequencing”. In: *Angewandte Chemie* 133.27 (2021), pp. 14862–14873. ISSN: 0044-8249. DOI: 10.1002/ange.202013462.

[61] Kefan Wang et al. “Unambiguous discrimination of all 20 proteinogenic amino acids and their modifications by nanopore”. In: *Nature methods* 21.1 (2024), pp. 92–101. DOI: 10.1038/s41592-023-02021-8.

[62] Yuqin Wang et al. “Identification of nucleoside monophosphates and their epigenetic modifications using an engineered nanopore”. In: *Nature nanotechnology* 17.9 (2022), pp. 976–983. ISSN: 1748-3387. DOI: 10.1038/s41565-022-01169-2.

[63] Huma Bhatti et al. “Recent advances in biological nanopores for nanopore sequencing, sensing and comparison of functional variations in MspA mutants”. In: *RSC advances* 11.46 (2021), pp. 28996–29014. DOI: 10.1039/D1RA02364K.

[64] Stephen Cheley, Li-Qun Gu, and Hagan Bayley. “Stochastic Sensing of Nanomolar Inositol 1,4,5-Trisphosphate with an Engineered Pore”. In: *Chemistry & Biology* 9.7 (2002), pp. 829–838. ISSN: 1074-5521. DOI: 10.1016/S1074-5521(02)00172-2.

[65] A. J. Storm et al. “Fabrication of solid-state nanopores with single-nanometre precision”. In: *Nature materials* 2.8 (2003), pp. 537–540. ISSN: 1476-1122. DOI: 10.1038/nmat941.

[66] Z. Siwy et al. “Rectification and voltage gating of ion currents in a nanofabricated pore”. In: *Europhysics Letters (EPL)* 60.3 (2002), pp. 349–355. ISSN: 0295-5075. DOI: 10.1209/epl/i2002-00271-3.

[67] Henry S. White and Andreas Bund. “Ion current rectification at nanopores in glass membranes”. In: *Langmuir : the ACS journal of surfaces and colloids* 24.5 (2008), pp. 2212–2218. ISSN: 0743-7463. DOI: 10.1021/la702955k.

[68] Jingwei Bai et al. “Fabrication of sub-20 nm nanopore arrays in membranes with embedded metal electrodes at wafer scales”. In: *Nanoscale* 6.15 (2014), pp. 8900–8906. DOI: 10.1039/c3nr06723h.

[69] Michael M. Marshall, Jijin Yang, and Adam R. Hall. “Direct and transmission milling of suspended silicon nitride membranes with a focused helium ion beam”. In: *Scanning* 34.2 (2012), pp. 101–106. DOI: 10.1002/sca.21003.

[70] Harold Kwok, Kyle Briggs, and Vincent Tabard-Cossa. “Nanopore fabrication by controlled dielectric breakdown”. In: *PloS one* 9.3 (2014), e92880. DOI: 10.1371/journal.pone.0092880.

[71] Zehui Xia et al. “Silicon Nitride Nanopores Formed by Simple Chemical Etching: DNA Translocations and TEM Imaging”. In: *ACS nano* 16.11 (2022), pp. 18648–18657. DOI: 10.1021/acsnano.2c07240.

[72] J. H. Yuan et al. “A Simple Method for Preparation of Through-Hole Porous Anodic Alumina Membrane”. In: *Chemistry of Materials* 16.10 (2004), pp. 1841–1844. ISSN: 0897-4756. DOI: 10.1021/cm049971u.

[73] Song Liu et al. “Boron nitride nanopores: highly sensitive DNA single-molecule detectors”. In: *Advanced Materials* 25.33 (2013), pp. 4549–4554. ISSN: 0935-9648. DOI: 10.1002/adma.201301336.

[74] V. Dimitrov et al. “Nanopores in solid-state membranes engineered for single molecule detection”. In: *Nanotechnology* 21.6 (2010), p. 065502. DOI: 10.1088/0957-4484/21/6/065502.

[75] Sourav Kundu and S. N. Karmakar. “Graphene nanopore devices for DNA sequencing: A tight-binding model study”. In: *Physica B: Condensed Matter* 623 (2021), p. 413334. ISSN: 09214526. DOI: 10.1016/j.physb.2021.413334.

[76] Yuxin Liu, Xiaochen Dong, and Peng Chen. “Biological and chemical sensors based on graphene materials”. In: *Chemical Society reviews* 41.6 (2012), pp. 2283–2307. DOI: 10.1039/C1CS15270J.

[77] M. J. Kim et al. “Rapid Fabrication of Uniformly Sized Nanopores and Nanopore Arrays for Parallel DNA Analysis”. In: *Advanced Materials* 18.23 (2006), pp. 3149–3153. ISSN: 0935-9648. DOI: 10.1002/adma.200601191.

[78] Bala Murali Venkatesan et al. “Highly Sensitive, Mechanically Stable Nanopore Sensors for DNA Analysis”. In: *Advanced Materials* 21.27 (2009), p. 2771. ISSN: 0935-9648. DOI: 10.1002/adma.200803786.

[79] Xin Meng et al. “Atomic Layer Deposition of Silicon Nitride Thin Films: A Review of Recent Progress, Challenges, and Outlooks”. In: *Materials (Basel, Switzerland)* 9.12 (2016). ISSN: 1996-1944. DOI: 10.3390/ma9121007.

[80] Yung-Chien Chou et al. “Lifetime and Stability of Silicon Nitride Nanopores and Nanopore Arrays for Ionic Measurements”. In: *ACS nano* 14.6 (2020), pp. 6715–6728. DOI: 10.1021/acsnano.9b09964.

[81] Olivia M. Eggenberger, Cuifeng Ying, and Michael Mayer. “Surface coatings for solid-state nanopores”. In: *Nanoscale* 11.42 (2019), pp. 19636–19657. DOI: 10.1039/C9NR05367K.

[82] Cees Dekker. “Solid-state nanopores”. In: *Nature nanotechnology* 2.4 (2007), pp. 209–215. ISSN: 1748-3387. DOI: 10.1038/nnano.2007.27.

[83] Liang Xue et al. “Solid-state nanopore sensors”. In: *Nature Reviews Materials* 5.12 (2020), pp. 931–951. DOI: 10.1038/s41578-020-0229-6.

[84] Bo Song et al. “Atomic-scale electron-beam sculpting of near-defect-free graphene nanostructures”. In: *Nano letters* 11.6 (2011), pp. 2247–2250. DOI: 10.1021/nl200369r.

[85] Simon Finn Mayer, Chan Cao, and Matteo Dal Peraro. “Biological nanopores for single-molecule sensing”. In: *iScience* 25.4 (2022), p. 104145. DOI: 10.1016/j.isci.2022.104145.

[86] Vishal Maingi et al. “Stability and dynamics of membrane-spanning DNA nanopores”. In: *Nature communications* 8 (2017), p. 14784. DOI: 10.1038/ncomms14784.

[87] S. Garaj et al. “Graphene as a subnanometre trans-electrode membrane”. In: *Nature* 467.7312 (2010), pp. 190–193. ISSN: 1476-4687. DOI: 10.1038/nature09379.

[88] Daniel Fologea et al. “Slowing DNA translocation in a solid-state nanopore”. In: *Nano letters* 5.9 (2005), pp. 1734–1737. DOI: 10.1021/nl051063o.

[89] Payel Sen, Hiofan Hoi, and Manisha Gupta. “Low Noise Hybrid Nanopore with Engineered OmpG and Bilayer MoS 2”. In: *ACS Applied Bio Materials* 4.7 (2021), pp. 5416–5424. ISSN: 2576-6422. DOI: 10.1021/acsabm.1c00095.

[90] Alessio Fragasso, Sonja Schmid, and Cees Dekker. “Comparing Current Noise in Biological and Solid-State Nanopores”. In: *ACS nano* 14.2 (2020), pp. 1338–1349. DOI: 10.1021/acsnano.9b09353.

[91] Zhipeng Tang et al. “Surface modification of solid-state nanopores for sticky-free translocation of single-stranded DNA”. In: *Small (Weinheim an der Bergstrasse, Germany)* 10.21 (2014), pp. 4332–4339. DOI: 10.1002/smll.201401091.

[92] Zexi Liang et al. “Interaction prolonged DNA translocation through solid-state nanopores”. In: *Nanoscale* 7.24 (2015), pp. 10752–10759. DOI: 10.1039/C5NR01954K.

[93] Cheng-Yu Lee et al. “Combining aptamer-modified gold nanoparticles with barcode DNA sequence amplification for indirect analysis of ethanolamine”. In: *Sensors and Actuators B: Chemical* 254 (2018), pp. 189–196. ISSN: 09254005. DOI: 10.1016/j.snb.2017.07.073.

[94] Adam R. Hall et al. “Hybrid pore formation by directed insertion of α-haemolysin into solid-state nanopores”. In: *Nature nanotechnology* 5.12 (2010), pp. 874–877. ISSN: 1748-3387. DOI: 10.1038/nnano.2010.237.

[95] Boxuan Shen et al. “Advanced DNA Nanopore Technologies”. In: *ACS Applied Bio Materials* 3.9 (2020), pp. 5606–5619. ISSN: 2576-6422. DOI: 10.1021/acsabm.0c00879.

[96] Fupeng Qin et al. “Construction and applications of hybrid nanochannels with helical foldamers and solid-state nanopores”. In: *Chemical Engineering Journal* 489 (2024), p. 151006. ISSN: 13858947. DOI: 10.1016/j.cej.2024.151006.

[97] Mehrnaz Mojtabavi et al. “High-Voltage Biomolecular Sensing Using a Bacteriophage Portal Protein Covalently Immobilized within a Solid-State Nanopore”. In: *Journal of the American Chemical Society* 144.49 (2022), pp. 22540–22548. ISSN: 0002-7863. DOI: 10.1021/jacs.2c08514.

[98] Pin Chen et al. “Portable nanopore-sequencing technology: Trends in development and applications”. In: *Frontiers in microbiology* 14 (2023), p. 1043967. ISSN: 1664-302X. DOI: 10.3389/fmicb.2023.1043967.

[99] Lucile Reynaud et al. “Sensing with Nanopores and Aptamers: A Way Forward”. In: *Sensors (Basel, Switzerland)* 20.16 (2020). DOI: 10.3390/s20164495.

[100] Karen Thomson et al. “Preliminary nanopore cheminformatics analysis of aptamer-target binding strength”. In: *BMC bioinformatics* 8 Suppl 7.Suppl 7 (2007), S11. DOI: 10.1186/1471-2105-8-S7-S11.

[101] Ji Wook Shim, Qiulin Tan, and Li-Qun Gu. “Single-molecule detection of folding and unfolding of the G-quadruplex aptamer in a nanopore nanocavity”. In: *Nucleic acids research* 37.3 (2009), pp. 972–982. DOI: 10.1093/nar/gkn968.

[102] Ting Li et al. “A universal strategy for aptamer-based nanopore sensing through host-guest interactions inside α-hemolysin”. In: *Angewandte Chemie (International ed. in English)* 54.26 (2015), pp. 7568–7571. DOI: 10.1002/anie.201502047.

[103] Xu Wang et al. “Nanoparticle-based immunosensors and immunoassays for aflatoxins”. In: *Analytica chimica acta* 912 (2016), pp. 10–23. DOI: 10.1016/j.aca.2016.01.048.

[104] Ryuji Kawano et al. “Rapid detection of a cocaine-binding aptamer using biological nanopores on a chip”. In: *Journal of the American Chemical Society* 133.22 (2011), pp. 8474–8477. ISSN: 0002-7863. DOI: 10.1021/ja2026085.

[105] Christina Kratschmer and Matthew Levy. “Effect of Chemical Modifications on Aptamer Stability in Serum”. In: *Nucleic acid therapeutics* 27.6 (2017), pp. 335–344. DOI: 10.1089/nat.2017.0680.

[106] Sayyed Mohamad Azimi et al. “A magnetic bead-based DNA extraction and purification microfluidic device”. In: *Microfluidics and Nanofluidics* 11.2 (2011), pp. 157–165. ISSN: 1613-4982. DOI: 10.1007/s10404-011-0782-9.

[107] Yu-Chen Lee et al. “One-step isolation of plasma membrane proteins using magnetic beads with immobilized concanavalin A”. In: *Protein expression and purification* 62.2 (2008), pp. 223–229. DOI: 10.1016/j.pep.2008.08.003.

[108] Luciano F. Huergo et al. “Magnetic Bead-Based Immunoassay Allows Rapid, Inexpensive, and Quantitative Detection of Human SARS-CoV-2 Antibodies”. In: *ACS sensors* 6.3 (2021), pp. 703–708. DOI: 10.1021/acssensors.0c02544.

[109] Eddie C. Y. Wang, Leszek K. Borysiewicz, and Anthony P. Weetman. “Cell Sorting Using Immunomagnetic Beads”. In: *Immunochemical Protocols*. Ed. by Margaret M. Manson. Vol. 10. New Jersey: Humana Press, 1992, pp. 347–358. ISBN: 0-89603-204-3. DOI: 10.1385/0-89603-204-3:347.

[110] T. Ji et al. “Preparation, Characterization, and Application of Au-Shell/Polystyrene Beads and Au-Shell/Magnetic Beads”. In: *Advanced Materials* 13.16 (2001), p. 1253. ISSN: 0935-9648. DOI: 10.1002/1521-4095(200108)13:16{\textless}1253::AID-ADMA1253{\textgreater}3.0.CO;2-T.

[111] K. Rudi et al. “Rapid, universal method to isolate PCR-ready DNA using magnetic beads”. In: *BioTechniques* 22.3 (1997), pp. 506–511. ISSN: 0736-6205. DOI: 10.2144/97223rr01.

[112] Fengchun Zhao et al. “Development of a rapid magnetic bead-based immunoassay for sensitive detection of zearalenone”. In: *Food Control* 79 (2017), pp. 227–233. ISSN: 09567135. DOI: 10.1016/j.foodcont.2017.03.051.

[113] Harshvardhan Modh, Thomas Scheper, and Johanna-Gabriela Walter. “Aptamer-Modified Magnetic Beads in Biosensing”. In: *Sensors (Basel, Switzerland)* 18.4 (2018). DOI: 10.3390/s18041041.

[114] Seray Adams et al. “Involvement of the kynurenine pathway in human glioma pathophysiology”. In: *PloS one* 9.11 (2014), e112945. DOI: 10.1371/journal.pone.0112945.

[115] Igor Cervenka, Leandro Z. Agudelo, and Jorge L. Ruas. “Kynurenines: Tryptophan’s metabolites in exercise, inflammation, and mental health”. In: *Science* 357.6349 (2017). ISSN: 1095-9203. DOI: 10.1126/science.aaf9794.

[116] Robert Dantzer. “Role of the Kynurenine Metabolism Pathway in Inflammation-Induced Depression: Preclinical Approaches”. In: *Current topics in behavioral neurosciences* 31 (2017), pp. 117–138. ISSN: 1866-3370. DOI: 10.1007/7854{\textunderscore}2016{\textunderscore}6.

[117] Abdulla A-B Badawy. “Kynurenine Pathway of Tryptophan Metabolism: Regulatory and Functional Aspects”. In: *International journal of tryptophan research : IJTR* 10 (2017), p. 1178646917691938. ISSN: 1178-6469. DOI: 10.1177/1178646917691938..

[118] Helen J. Ball et al. “Indoleamine 2,3-dioxygenase-2; a new enzyme in the kynurenine pathway”. In: *The international journal of biochemistry & cell biology* 41.3 (2009), pp. 467–471. DOI: 10.1016/j.biocel.2008.01.005..

[119] Abdulla A-B Badawy. “Tryptophan metabolism in alcoholism”. In: *Nutrition research reviews* 15.1 (2002), pp. 123–152. DOI: 10.1079/NRR200133.

[120] Trevor W. Stone, Nicholas Stoy, and L. Gail Darlington. “An expanding range of targets for kynurenine metabolites of tryptophan”. In: *Trends in pharmacological sciences* 34.2 (2013), pp. 136–143. DOI: 10.1016/j.tips.2012.09.006..

[121] Senad Divanovic et al. “Opposing biological functions of tryptophan catabolizing enzymes during intracellular infection”. In: *The Journal of infectious diseases* 205.1 (2012), pp. 152–161. DOI: 10.1093/infdis/jir621..

[122] Yuzo Suzuki et al. “Serum indoleamine 2,3-dioxygenase activity predicts prognosis of pulmonary tuberculosis”. In: *Clinical and vaccine immunology : CVI* 19.3 (2012), pp. 436–442. DOI: 10.1128/CVI.05402-11..

[123] T. A. Babcock and J. M. Carlin. “Transcriptional activation of indoleamine dioxygenase by interleukin 1 and tumor necrosis factor alpha in interferon-treated epithelial cells”. In: *Cytokine* 12.6 (2000), pp. 588–594. ISSN: 1043-4666. DOI: 10.1006/cyto.1999.0661.

[124] Milton W. Taylor and Gensheng Feng. “Relationship between interferon–γ, indoleamine 2,3–dioxygenase, and tryptophan catabolism”. In: *The FASEB Journal* 5.11 (1991), pp. 2516–2522. ISSN: 0892-6638. DOI: 10.1096/FASEBJ.5.11.1907934.

[125] Andrew L. Mellor and David H. Munn. “IDO expression by dendritic cells: tolerance and tryptophan catabolism”. In: *Nature reviews. Immunology* 4.10 (2004), pp. 762–774. ISSN: 1474-1733. DOI: 10.1038/nri1457.

[126] Jörg C. Schefold et al. “Increased indoleamine 2,3-dioxygenase (IDO) activity and elevated serum levels of tryptophan catabolites in patients with chronic kidney disease: a possible link between chronic inflammation and uraemic symptoms”. In: *Nephrology, dialysis, transplantation : official publication of the European Dialysis and Transplant Association - European Renal Association* 24.6 (2009), pp. 1901–1908. DOI: 10.1093/ndt/gfn739.

[127] Yoric Gagnebin et al. “Exploring blood alterations in chronic kidney disease and haemodialysis using metabolomics”. In: *Scientific reports* 10.1 (2020), p. 19502. DOI: 10.1038/s41598-020-76524-1..

[128] Jürgen Kaden et al. “Dynamics and Diagnostic Relevance of Kynurenine Serum Level after Kidney Transplantation”. In: *Annals of transplantation* 20 (2015), pp. 327–337. DOI: 10.12659/AOT.893721..

[129] Piotr Buczko, Anna Tankiewicz-Kwedlo, Agnieszka Buraczewska, Dariusz Pawlak, Michal Mysliwiec. *Accumulation of kynurenine pathway metabolites in saliva and plasma of uremic patients*. 2007. URL: http://if-pan.krakow.pl/pjp/pdf/2007/s1_199.pdf.

[130] Hansongyi Lee et al. “Amino Acid Metabolites Associated with Chronic Kidney Disease: An Eight-Year Follow-Up Korean Epidemiology Study”. In: *Biomedicines* 8.7 (2020). ISSN: 2227-9059. DOI: 10.3390/biomedicines8070222.

[131] Vetalise C. Konje et al. “Tryptophan levels associate with incident cardiovascular disease in chronic kidney disease”. In: *Clinical kidney journal* 14.4 (2021), pp. 1097–1105. ISSN: 2048-8505. DOI: 10.1093/ckj/sfaa031..

[132] G. Brandacher et al. “Non-invasive monitoring of kidney allograft rejection through IDO metabolism evaluation”. In: *Kidney international* 71.1 (2007), pp. 60–67. ISSN: 0085-2538. DOI: 10.1038/sj.ki.5002023..

[133] José Joaquín Merino et al. “Elevated Systemic L-Kynurenine/L-Tryptophan Ratio and Increased IL-1 Beta and Chemokine (CX3CL1, MCP-1) Proinflammatory Mediators in Patients with Long-Term Titanium Dental Implants”. In: *Journal of clinical medicine* 8.9 (2019). ISSN: 2077-0383. DOI: 10.3390/jcm8091368.

[134] N. Clendenen et al. “Acute Metabolomic Changes after Implantation of a Left Ventricular Assist Device”. In: *The Journal of Heart and Lung Transplantation* 38.4 (2019), S245. ISSN: 10532498. DOI: 10.1016/j.healun.2019.01.605.

[135] Jolanta Flieger et al. “Determination of Tryptophan and Its Major Metabolites in Fluid from the Anterior Chamber of the Eye in Diabetic Patients with Cataract by Liquid Chromotography Mass Spectrometry (LC-MS/MS)”. In: *Molecules (Basel, Switzerland)* 23.11 (2018). DOI: 10.3390/molecules23113012.

[136] Francesca M. Notarangelo et al. “Gas chromatography/tandem mass spectrometry detection of extracellular kynurenine and related metabolites in normal and lesioned rat brain”. In: *Analytical biochemistry* 421.2 (2012), pp. 573–581. DOI: 10.1016/j.ab.2011.12.032.

[137] Ditta Ungor et al. “Red-emitting gold nanoclusters for rapid fluorescence sensing of tryptophan metabolites”. In: *Sensors and Actuators B: Chemical* 288 (2019), pp. 728–733. ISSN: 09254005. DOI: 10.1016/j.snb.2019.03.026.

[138] Jessica L. Klockow and Timothy E. Glass. “Development of a fluorescent chemosensor for the detection of kynurenine”. In: *Organic letters* 15.2 (2013), pp. 235–237. DOI: 10.1021/ol303025m.

[139] Nicole Seegers et al. “High-throughput fluorescence-based screening assays for tryptophan-catabolizing enzymes”. In: *Journal of biomolecular screening* 19.9 (2014), pp. 1266–1274. DOI: 10.1177/1087057114536616.

[140] E. Miedema and K. E. Richardson. “Ethanolamine metabolism in plant tissues”. In: *Plant physiology* 41.6 (1966), pp. 1026–1030. ISSN: 0032-0889. DOI: 10.1104/pp.41.6.1026.

[141] Dhaval Patel and Stephan N. Witt. “Ethanolamine and Phosphatidylethanolamine: Partners in Health and Disease”. In: *Oxidative medicine and cellular longevity* 2017 (2017), p. 4829180. DOI: 10.1155/2017/4829180.

[142] Yerim Kwon et al. “Arabidopsis serine decarboxylase mutants implicate the roles of ethanolamine in plant growth and development”. In: *International journal of molecular sciences* 13.3 (2012), pp. 3176–3188. DOI: 10.3390/ijms13033176.

[143] Elizabeth Calzada, Ouma Onguka, and Steven M. Claypool. “Phosphatidylethanolamine Metabolism in Health and Disease”. In: *International review of cell and molecular biology* 321 (2015), pp. 29–88. ISSN: 1937-6448. DOI: 10.1016/bs.ircmb.2015.10.001.

[144] David S. Wishart et al. “HMDB: the Human Metabolome Database”. In: *Nucleic acids research* 35.Database issue (2007), pp. D521–6. DOI: 10.1093/nar/gkl923.

[145] Dayan B. Goodenowe et al. “Peripheral ethanolamine plasmalogen deficiency: a logical causative factor in Alzheimer’s disease and dementia”. In: *Journal of lipid research* 48.11 (2007), pp. 2485–2498. ISSN: 0022-2275. DOI: 10.1194/jlr.P700023-JLR200.

[146] Shiro Mawatari et al. “Decreases of ethanolamine plasmalogen and phosphatidylcholine in erythrocyte are a common phenomenon in Alzheimer’s, Parkinson’s, and coronary artery diseases”. In: *Brain research bulletin* 189 (2022), pp. 5–10. DOI: 10.1016/j.brainresbull.2022.08.009.

[147] D. W. Ellison, M. F. Beal, and J. B. Martin. “Phosphoethanolamine and ethanolamine are decreased in Alzheimer’s disease and Huntington’s disease”. In: *Brain research* 417.2 (1987), pp. 389–392. ISSN: 0006-8993. DOI: 10.1016/0006-8993(87)90471-9.

[148] Josephine S. Modica-Napolitano and Perry F. Renshaw. “Ethanolamine and phosphoethanolamine inhibit mitochondrial function in vitro: implications for mitochondrial dysfunction hypothesis in depression and bipolar disorder”. In: *Biological psychiatry* 55.3 (2004), pp. 273–277. ISSN: 0006-3223. DOI: 10.1016/S0006-3223(03)00784-4.

[149] C. S. Lieber, S. J. Robins, and M. A. Leo. “Hepatic Phosphatidylethanolamine Methyltransferase Activity Is Decreased by Ethanol and Increased by Phosphatidylcholine”. In: *Alcoholism: Clinical and Experimental Research* 18.3

(1994), pp. 592–595. ISSN: 0145-6008. DOI: 10.1111/j.1530-0277.1994.tb00915.x.

[150] Kholoud A Elmihi et al. “The emerging role of ethanolamine phosphate phospholyase in regulating hepatic phosphatidylethanolamine and plasma lipoprotein metabolism in mice”. In: *FASEB journal : official publication of the Federation of American Societies for Experimental Biology* 38.18 (2024), e70063. DOI: 10.1096/fj.202401321R.

[151] Tong Liu et al. “A conjunctive lipidomic approach reveals plasma ethanolamine plasmalogens and fatty acids as early diagnostic biomarkers for colorectal cancer patients”. In: *Expert review of proteomics* 17.3 (2020), pp. 233–242. DOI: 10.1080/14789450.2020.1757443.

[152] T. Kano-Sueoka et al. “Analysis of cytosolic phosphoethanolamine and ethanolamine and their correlation with prognostic factors in breast cancer”. In: *Japanese journal of cancer research : Gann* 82.7 (1991), pp. 829–834. ISSN: 0910-5050. DOI: 10.1111/j.1349-7006.1991.tb02709.x.

[153] Pengxun Han et al. “Niclosamide ethanolamine improves diabetes and diabetic kidney disease in mice”. In: *American journal of translational research* 10.4 (2018), pp. 1071–1084. ISSN: 1943-8141.

[154] Peter Fechner et al. “Size does matter! Label-free detection of small molecule-protein interaction”. In: *Analytical and bioanalytical chemistry* 406.17 (2014), pp. 4033–4051. DOI: 10.1007/s00216-014-7834-4.

[155] Gang Liang et al. “Aptamer-based biosensor for label-free detection of ethanolamine by electrochemical impedance spectroscopy”. In: *Analytica chimica acta* 936 (2016), pp. 222–228. DOI: 10.1016/j.aca.2016.06.056.

[156] Ole Mrklas, Angus Chu, and Stuart Lunn. “Determination of ethanolamine, ethylene glycol and triethylene glycol by ion chromatography for laboratory and field biodegradation studies”. In: *Journal of environmental monitoring : JEM* 5.2 (2003), pp. 336–340. ISSN: 1464-0325. DOI: 10.1039/b210572a.

[157] Bhavna Sikarwar et al. “Enzyme Based Electrochemical Biosensor for Ethanolamine”. In: *Electroanalysis* 28.4 (2016), pp. 881–889. ISSN: 1040-0397. DOI: 10.1002/elan.201501046.

[158] Sadia Ameen, M. Shaheer Akhtar, and Hyung-Shik Shin. “Low temperature grown ZnO nanotubes as smart sensing electrode for the effective detection of ethanolamine chemical”. In: *Materials Letters* 106 (2013), pp. 254–258. ISSN: 0167577X. DOI: 10.1016/J.MATLET.2013.05.031.

[159] Kidan Lee et al. “Recent Progress in Solid-State Nanopores”. In: *Advanced Materials* 30.42 (2018), e1704680. ISSN: 0935-9648. DOI: 10.1002/adma.201704680.

[160] Maureen McKeague and Maria C. Derosa. “Challenges and opportunities for small molecule aptamer development”. In: *Journal of nucleic acids* 2012 (2012), p. 748913. DOI: 10.1155/2012/748913.

[161] Alexandra Heilkenbrinker et al. “Identification of the target binding site of ethanolamine-binding aptamers and its exploitation for ethanolamine detection”. In: *Analytical chemistry* 87.1 (2015), pp. 677–685. DOI: 10.1021/ac5034819.

[162] Doerthe Mann et al. “In vitro selection of DNA aptamers binding ethanolamine”. In: *Biochemical and biophysical research communications* 338.4 (2005), pp. 1928–1934. ISSN: 0006-291X. DOI: 10.1016/j.bbrc.2005.10.172.

[163] Betty Chu et al. “Crystal Structure of a Tetrameric DNA Fold-Back Quadruplex”. In: *Journal of the American Chemical Society* 140.47 (2018), pp. 16291–16298. ISSN: 0002-7863. DOI: 10.1021/jacs.8b10153.

[164] Tao Li, Shaojun Dong, and Erkang Wang. “G-quadruplex aptamers with peroxidase-like DNAzyme functions: which is the best and how does it work?” In: *Chemistry, an Asian journal* 4.6 (2009), pp. 918–922. DOI: 10.1002/asia.200900019.

[165] Xiaohong Cheng et al. “Specific DNA G-quadruplexes bind to ethanolamines”. In: *Biopolymers* 91.10 (2009), pp. 874–883. ISSN: 0006-3525. DOI: 10.1002/bip.21272.

[166] Mostafa Mahmoud, Stefan Laufer, and Hans-Peter Deigner. “Visual aptamer-based capillary assay for ethanolamine using magnetic particles and strand displacement”. In: *Microchimica Acta* 186.11 (2019), p. 690. ISSN: 0026-3672. DOI: 10.1007/s00604-019-3795-9.

[167] Mostafa Mahmoud, Stefan Laufer, and Hans-Peter Deigner. “An aptamer based thermofluorimetric assay for ethanolamine”. In: *Biochimie* 158 (2019), pp. 233–237. DOI: 10.1016/j.biochi.2019.01.014.

[168] Redouan Mahou and Christine Wandrey. “Versatile Route to Synthesize Heterobifunctional Poly(ethylene glycol) of Variable Functionality for Subsequent Pegylation”. In: *Polymers* 4.1 (2012). Published: 16 February 2012, pp. 561–589. DOI: 10.3390/polym4010561. URL: https://doi.org/10.3390/polym4010561.

[169] Kyong-Oh Shin and Yong-Moon Lee. “Simultaneous analysis of mono-, di-, and tri-ethanolamine in cosmetic products using liquid chromatography coupled tandem mass spectrometry”. In: *Archives of Pharmacal Research* 38.12 (2015), pp. 2156–2163. DOI: 10.1007/s12272-015-0677-5.

[170] Charles R. Harris et al. “Array programming with NumPy”. In: *Nature* 585 (2020), pp. 357–362. DOI: 10.1038/s41586-020-2649-2.

[171] Skipper Seabold and Josef Perktold. “Statsmodels: Econometric and Statistical Modeling with Python”. In: *Proceedings of the 9th Python in Science Conference*. Austin, TX, June 2010, pp. 57–61. DOI: 10.25080/Majora-92bf1922-011. URL: https://doi.org/10.25080/Majora-92bf1922-011.

[172] h5py contributors. *h5py Documentation (stable)*. Accessed: 2025-07-07. n.d. URL: https://docs.h5py.org/en/stable/.

[173] Matthew Waugh et al. “Solid-state nanopore fabrication by automated controlled breakdown”. In: *Nature protocols* 15.1 (2020), pp. 122–143. DOI: 10.1038/s41596-019-0255-2.

[174] J. Niskanen et al. “Thermal Response of a PVCL-HA Conjugate”. In: *Journal of Polymer Science Part A: Polymer Chemistry* 54 (2016), pp. 425–436. DOI: 10.1002/pola.27794. URL: https://doi.org/10.1002/pola.27794.

[175] K. Helttunen et al. “Interaction of Aminomethylated Resorcinarenes with Rhodamine B”. In: *New Journal of Chemistry* 33 (2009), p. 1148. DOI: 10.1039/b820409h. URL: https://doi.org/10.1039/b820409h.

[176] J. Kaden et al. “Untersuchungen zur Dynamik der Indolamin 2,3-Dioxygenase bei Patienten mit unterschiedlichen Verläufen nach Nierentransplantation”. In: *Transplant. Organ Dtsch. Transplant.* 19 (2007). [Google Scholar], pp. 110–116.

[177] Aman Sachan et al. “Specificity and ligand affinities of the cocaine aptamer: impact of structural features and physiological NaCl”. In: *Analytical Chemistry* 88.15 (2016), pp. 7715–7723.

[178] Jiali Li et al. “Characterization of protein unfolding with solid-state nanopores”. In: *Current Pharmaceutical Biotechnology* 14.10 (2013), pp. 965–972. DOI: 10.2174/09298665113209990077.

[179] Albert S. W. Kang et al. “Ready-to-use nanopore platform for the detection of any DNA/RNA oligo at attomole range using an Osmium tagged complementary probe”. In: *Scientific Reports* 10 (2020), p. 19790. DOI: 10.1038/s41598-020-76892-9.

[180] Madiha Sultan and Anastassia Kanavarioti. “Nanopore device-based fingerprinting of RNA oligos and microRNAs enhanced with an Osmium tag”. In: *Scientific Reports* 9 (2019), p. 14180. DOI: 10.1038/s41598-019-50425-7.

[181] Nanami Takeuchi, Moe Hiratani, and Ryuji Kawano. “Pattern Recognition of microRNA Expression in Body Fluids Using Nanopore Decoding at Subfemtomolar Concentrations”. In: *ACS Sensors* (June 2022). DOI: 10.1021/acssensors.2c00891.

[182] Camilla L.C. Ip et al. “MinION Analysis and Reference Consortium: Phase 1 data release and analysis”. In: *F1000Research* 4 (2015). Version 1; peer review: 2 approved, p. 1075. DOI: 10.12688/f1000research.7201.1.

[183] Bo Lu et al. “Origins and Consequences of Velocity Fluctuations during DNA Passage through a Nanopore”. In: *Biophysical Journal* 105.3 (2013), pp. L41–L44. DOI: 10.1016/j.bpj.2013.06.030.

[184] Kyle Briggs, Harold Kwok, and Vincent Tabard-Cossa. “Automated Fabrication of 2-nm Solid-State Nanopores for Nucleic Acid Analysis”. In: *Small* 10.10 (2014), pp. 2077–2085. DOI: 10.1002/smll.201303602.

[185] Aleksij Aksimentiev et al. “Microscopic Kinetics of DNA Translocation through Synthetic Nanopores”. In: *Biophysical Journal* 87.4 (2004), pp. 2086–2097. DOI: 10.1529/biophysj.104.045675.

[186] Rajesh Kumar Sharma et al. “Complex DNA knots detected with a nanopore sensor”. In: *Nature Communications* 10.1 (2019). Open Access, p. 4473. ISSN: 2041-1723. DOI: 10.1038/s41467-019-12358-4.

[187] Shintaro Ogawa et al. “Reduced cerebrospinal fluid ethanolamine concentration in major depressive disorder”. In: *Scientific Reports* 4 (2014), p. 5796. DOI: 10.1038/srep07796. URL: https://doi.org/10.1038/srep07796.

[188] Melissa M. Kendall et al. “Ethanolamine Controls Expression of Genes Encoding Components Involved in Interkingdom Signaling and Virulence in Enterohemorrhagic Escherichia coli O157:H7”. In: *mBio* 3.2 (2012), e00050–12. DOI: 10.1128/mbio.00050-12. URL: https://doi.org/10.1128/mbio.00050-12.

[189] M. Sugimoto, D. T. Wong, A. Hirayama, et al. “Capillary electrophoresis mass spectrometry-based saliva metabolomics identified oral, breast and pancreatic cancer-specific profiles”. In: *Metabolomics* 6 (2010). Received: 08 April 2009; Accepted: 18 August 2009; Published: 10 September 2009, pp. 78–95. DOI: 10.1007/s11306-009-0178-y. URL: https://doi.org/10.1007/s11306-009-0178-y.

[190] Tariq Shah et al. “Molecular causes of elevated phosphoethanolamine in breast and pancreatic cancer cells”. In: *NMR in Biomedicine* (2018). First published: 21 June 2018. DOI: 10.1002/nbm.3936. URL: https://doi.org/10.1002/nbm.3936.

[191] Alexander Payne et al. “BulkVis: a graphical viewer for Oxford nanopore bulk FAST5 files”. In: *Bioinformatics* 35.13 (2019). Published 2019, pp. 2193–2198. DOI: 10.1093/bioinformatics/btz110. URL: https://doi.org/10.1093/bioinformatics/btz110.

[192] James M. Ferguson and Martin A. Smith. “SquiggleKit: a toolkit for manipulating nanopore signal data”. In: *Bioinformatics* 35.24 (2019). Published 23 July 2019, Open Access, pp. 5372–5373. DOI: 10.1093/bioinformatics/btz586. URL: https://doi.org/10.1093/bioinformatics/btz586.

[193] Xin Lei et al. “Controllable Shrinking Fabrication of Solid-State Nanopores”. In: *Micromachines* 13.6 (2022). ISSN: 2072-666X. DOI: 10.3390/mi13060923.

[194] Eric Beamish et al. “Fine-tuning the size and minimizing the noise of solid-state nanopores”. In: *Journal of visualized experiments : JoVE* 80 (2013), e51081. DOI: 10.3791/51081.

[195] Jasper P. Fried et al. “In situ solid-state nanopore fabrication”. In: *Chemical Society reviews* 50.8 (2021), pp. 4974–4992. DOI: 10.1039/D0CS00924E.

[196] Guohua Xu et al. “Structural Insights into the Mechanism of High-Affinity Binding of Ochratoxin A by a DNA Aptamer”. In: *Journal of the American Chemical Society* 144.17 (2022), pp. 7731–7740. ISSN: 0002-7863. DOI: 10.1021/jacs.2c00478.

[197] Qi Chen and Zewen Liu. “Fabrication and Applications of Solid-State Nanopores”. In: *Sensors (Basel, Switzerland)* 19.8 (2019). DOI: 10.3390/s19081886.

[198] Shuanglin Yue and Changzhi Gu. “Nanopores fabricated by focused ion beam milling technology”. In: *2007 7th IEEE Conference on Nanotechnology (IEEE NANO)*. IEEE, 2007, pp. 628–631. ISBN: 978-1-4244-0607-4. DOI: 10.1109/NANO.2007.4601269.

[199] N. Patterson et al. “Controlled fabrication of nanopores using a direct focused ion beam approach with back face particle detection”. In: *Nanotechnology* 19.23 (2008), p. 235304. DOI: 10.1088/0957-4484/19/23/235304.

[200] Xiaorui Zhu, Ceming Wang, and Lin Wang. “Properties and stability of atomic layer deposition modified track-etched single conical nanopore”. In: *Radiation Physics and Chemistry* 218 (2024), p. 111633. ISSN: 0969806X. DOI: 10.1016/j.radphyschem.2024.111633.

List of Figures